COMPUTATIONAL AND LABORATORY INVESTIGATIONS OF A MODEL OF BLOOD DROPLET FLIGHT FOR FORENSIC APPLICATIONS

by

Raquel Murray

A thesis submitted in conformity with the requirements
for the degree of Masters of Science
Faculty of Graduate Studies (Modelling and Computational Science)
University of Ontario Institute of Technology

Supervisor(s): Dr. Dhavide Aruliah and Dr. Faisal Z. Qureshi

Abstract

Computational and Laboratory Investigations of a Model of Blood Droplet Flight for Forensic Applications

Raquel Murray

Masters of Science

Faculty of Graduate Studies

University of Ontario Institute of Technology

2012

We present a three-dimensional, forward model of blood droplets in flight. The proposed model is based on a set of ordinary differential equations (ODEs) incorporating viscous drag and gravitational forces. We validate the model against laboratory experiments in which a mock crime scene is constructed. The experiments consist of a ballistics gel containing transfer blood or porcine blood shot by a riot ball from a paintball gun constituting a simulated bloodletting event. The experiments are captured using high-speed stereo camera pair from which three-dimensional trajectories can be extracted using tracking software. The long-term goal is to develop an accurate framework for forensic Bloodstain Pattern Analysis (BPA).

Dedication

I dedicate this thesis to my parents, Wayne and Pauline Murray.

Acknowledgements

I acknowledge Dr. Dhavide Aruliah and Dr. Faisal Z. Qureshi for their supervision, Dr. Franco Gaspari for overseeing the experiments in this research, Dr. Peter Berg for his helpful discussions, and Luis Zarrabeitia for his code and collaboration in this research.

Contents

1 Introduction **1**

1.1 Motivation and Background . . . 2

1.1.1 Dynamics of Blood Droplets . . . 3

1.2 Existing Methods for Bloodstain Pattern Analysis . . . 5

2 Laboratory Simulations of Bloodletting Events **12**

2.1 Outline of Procedure for Laboratory Experiments . . . 13

2.2 Preparing the Mock Crime Scene . . . 14

2.3 Calibrating the Recording Equipment . . . 18

2.3.1 Capturing a Moving Checkerboard for Calibration . . . 21

2.3.2 Capturing a Moving Laser Dot for Calibration . . . 23

2.3.3 Capturing a Falling Riot Ball for Orientation . . . 25

2.4 Running the Experiment . . . 26

2.5 Documenting and Verifying the Experiment . . . 26

3 Modelling Trajectories of Blood Droplets **31**

3.1 Models of Aerodynamic Drag . . . 33

3.1.1 Using Navier-Stokes Equations to describe non-Newtonian Fluids and the Reynolds Number . . . 33

3.1.2 Reynolds number: Re . . . 34

3.1.3 Stokes' Flow . . . 36

3.1.4 Drag Coefficient: κ 37

3.2 Dynamic ODE Model of Droplet Flight 39

3.3 Fitting the Dynamic ODE Model to the Laboratory Experiment Data . . 43

3.3.1 Reconstruction of Experimental Blood Droplet Trajectories 43

3.3.2 Using a Practical Optimisation Solver 46

3.3.3 Initialisation of Decision Parameters for Optimisation 47

3.3.4 Initialisation of the parameter θ 48

3.3.5 Criteria for Rejection of Reconstructed Trajectories 49

4 Experimental Results 52

4.1 Visual Verification of the Model on Single Trajectories 53

4.2 Visual Verification of the Fitting for Full Experiments 57

4.3 Validation of the Model by Comparing Speeds for Individual Trajectories 64

4.4 Validation of the Model by Comparing Speeds for Full Experiments . . . 68

4.5 Analysing the Reynolds numbers and Resulting Drag Coefficients 71

4.6 Analysing the Optimisation Norms and Average Estimated Misfits 74

4.7 Discussion 76

5 Conclusions and Future Research 82

5.1 Conclusions 82

5.2 Future Research 83

5.2.1 Initial Conditions of the Inverse Problem 83

5.2.2 Surfaces 86

5.2.3 Collisions 88

5.2.4 Models of Oscillations in Moving Droplet Shape 88

Bibliography 90

List of Tables

2.1 Materials for reconstructing experiment 15

3.1 List of notation 32
3.2 List of constants and known values 32

List of Figures

1.1 Region of intersection. 2

1.2 The spines on circular blood droplets. 4

1.3 The String Method. 6

1.4 Screen captures of trajectory reconstruction produced by *BACKTRACK™* [11]. 8

1.5 *HEMOSPAT™* stain identification (see [16]) 9

1.6 *HEMOSPAT™* screen captures. 10

2.1 Position of paintball gun in mock crime scene. 17

2.2 Positions of the high-speed cameras for experiment. 19

2.3 Positions of the high-speed cameras for experiment with markup. 20

2.4 Position of single high-speed camera in a previous experiment. 21

2.5 Manual tracking of a blood droplet using high-speed software. 22

2.6 Still shot of checkerboard calibration. 23

2.7 Placement of stationary checkerboards in mock crime scene. 24

2.8 Still shot of bad calibration validation using the laser. 25

2.9 Still shot of good calibration validation using the laser. 26

2.10 Still shot of riot ball calibration. 27

2.11 Visualisation of experimental path reconstructions. 28

2.12 Final photos of the mock crime scene using transfer blood. 29

3.1 Coordinate system. 33
3.2 Reynolds number plotted over speeds and radii. 35
3.3 A plot of the calculation of the drag coefficient using a range of Reynolds numbers in Equation 3.8. 38
3.4 Drag coefficient plotted over different speeds and radii. 39
3.5 Free body diagram of forces acting on a blood droplet. 40
3.6 Automated tracking of a full experiment using the Droplet Tracker [30]. . 44
3.7 Depiction of the coordinate system change when converting three-dimensional to two-dimensional or planar data. 46
3.8 ODE model trapped in wrong range of exit angle θ. 49
3.9 ODE model in correct range of exit angle θ. 50

4.1 ODE-based trajectory fit with DT trajectory for a porcine blood droplet. 54
4.2 ODE-based trajectory fit with DT trajectory for a transfer blood droplet. 55
4.3 ODE-based trajectory fit with DT path reconstruction for transfer blood. 56
4.4 xy plane view of DT trajectories of porcine blood droplets with their ODE-based trajectories. 58
4.5 zx plane view of DT trajectories of porcine blood droplets with their ODE-based trajectories. 59
4.6 zy plane view of DT trajectories of porcine blood droplets with their ODE-based trajectories. 60
4.7 xy plane view of DT trajectories of transfer blood droplets with their ODE-based trajectories. 61
4.8 zx plane view of DT trajectories of transfer blood droplets with their ODE-based trajectories. 62
4.9 zy plane view of DT trajectories of transfer blood droplets with their ODE-based trajectories. 63
4.10 Speed validation of one path in a porcine blood experiment. 65

4.11 Speed validation of one path in a transfer blood experiment. 66

4.12 Speed validation of one path in another transfer blood experiment. 67

4.13 Speed validation of all velocities calculated for a porcine blood experiment. 69

4.14 Speed validation of all velocities calculated for a transfer blood experiment. 70

4.15 Histogram of the Reynolds numbers calculated for a porcine blood experiment 72

4.16 Histogram of the Drag Coefficients calculated for a porcine blood experiment 73

4.17 Histogram of the Reynolds numbers calculated for a transfer blood experiment 74

4.18 Histogram of the drag coefficients calculated for a transfer blood experiment 75

4.19 A plot of the calculation of the drag coefficient using a range of Reynolds numbers from $10 \leq \mathrm{Re} \leq 5000$ in Equation 3.8 (in blue) and a line plotted at $\kappa = 0.424$ (in black). 76

4.20 The optimisation norms for each trajectory analysed by the model in a porcine blood experiment. 77

4.21 The average estimated misfit (from DT) for each trajectory analysed by the model in a porcine blood experiment. 78

4.22 The optimisation norms for each trajectory analysed by the model in a transfer blood experiment. 79

4.23 The average estimated misfit (from DT) for each trajectory analysed by the model in a transfer blood experiment. 80

5.1 Measurements of an elliptical bloodstain. 84

5.2 The impact angle (α), stringing angle (β) and glancing angle (γ) of a bloodstain. 85

5.3 A digital photograph of the resulting bloodstain pattern formed on a cardboard surface from the porcine blood experiment. 87

Chapter 1

Introduction

We investigate motion of blood droplets as they travel through air and present a physics-based, three-dimensional, forward simulation for modelling blood droplet trajectories. We develop the model by addressing the necessity of physical forces —gravity and drag— that are acting upon the droplet. The model is validated by setting up a physical experiment simulating a bullet hitting human flesh. In our experiments we know the position of the target and the position and type of the weapon used to fire the bullet. The model contains the following parameters: the drag coefficient, radii of the droplets, and the initial speeds of the droplets. The proposed model enables us to analyse the motion of the blood droplets through the air. Specifically, we study how well the proposed model explains the motion of physical blood droplets as these move through the air. We record our experiments using a high frame rate stereo camera pair and use a blood droplet tracker to estimate the three-dimensional trajectories of the blood droplets. These trajectories are subsequently used to validate the proposed model. We demonstrate that our model correctly identify the motion parameters associated with the trajectories of physical blood droplets. These include initial velocities and drag coefficients. The values for these parameters are found by fitting the proposed model to the trajectories of physical blood droplets by minimising the Euclidean norm.

1.1 Motivation and Background

Bloodstain Pattern Analysis (BPA) is a branch of forensic physics focused on analysing bloodstains found in a crime scene with the view to recreate the events leading to these bloodstains. The objective is to identify the cause (or source) of the bloodstain, often referred to as the bloodletting event. This includes knowing where a victim was positioned at the bloodletting event and what weapon or object caused the bloodletting event. The aim of BPA is to trace the stains from individual droplets back to their source. Under the assumption that the blood droplets from a single blood letting event are responsible for a particular bloodstain, the paths of these blood droplets should intersect when traced back from the bloodstain and the region of intersection of these paths is assumed to give a good indication of the position of the bloodletting event as depicted in Figure 1.1.

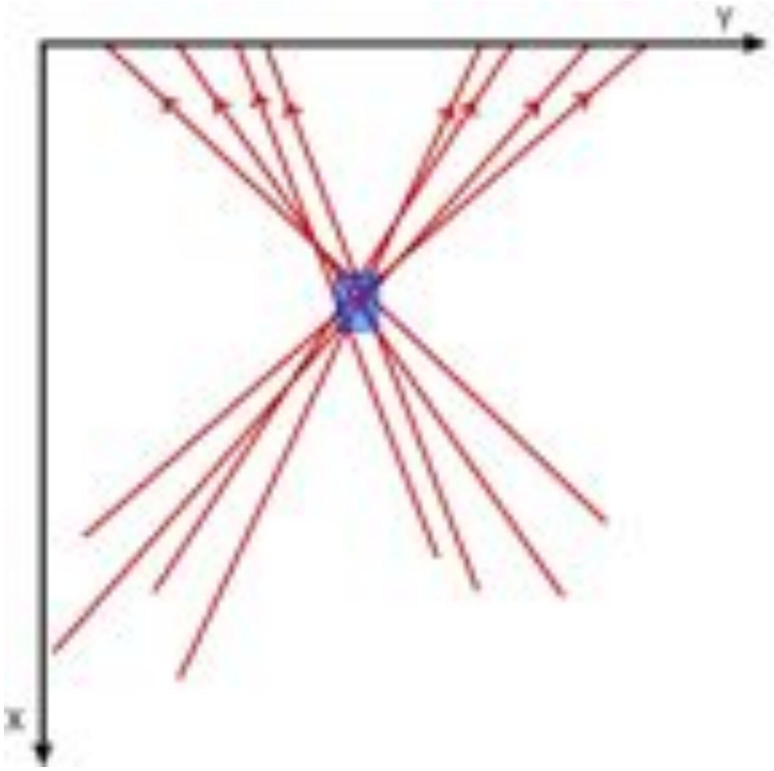

Figure 1.1: An overhead view of the intersection of blood droplet paths. The region in the blue square is considered region of intersection. The arrows indicate the direction of motion of the droplet. The bloodstain is created on the y plane. See [16]

Once a blood droplet exits the body, it travels along a unique trajectory toward the surface it is going to impact. This trajectory resembles a parabolic path and while the droplet is travelling along this path, radial contractions or oscillations of the droplet occur [25]. The proposed model does not account for radial distortions of the blood droplets as they fly through the air. In Section 5.2.4 we discuss some future research that can be done in this topic.

1.1.1 Dynamics of Blood Droplets

Blood droplet dynamics of human blood have been studied at length by Pizzola *et. al.* [22, 23]. [22] presents two experiments designed to observe the bloodstains formed when blood droplets fall vertically down on a surface. In the first experiment a blood droplet is released from a known height and falls on a stationary, inclined surface. Here the volume of the blood droplet is also known. The experiment is photographed to observe how the droplet impacts the surface and how the stain settles on the surface. The second experiment observes circular stains and their corresponding spines caused by a blood droplet falling from an ice pick, a scarf and a steel laboratory rod. Further research was done by Hulse-Smith *et. al.* in [9, 10] on extracting a droplet's diameter and impact velocity from the spines on a bloodstain. Figure 1.2 shows high-speed photographs of porcine blood droplets, of different diameters, falling onto paper and the resulting spines. In [23], another experiment was done involving a blood droplet falling onto a moving belt which could be set on an incline. The purpose of this was to view the differences in the stains when a droplet impacts a stationary surface on an incline and when a droplet impacts a moving surface on a flat plane. Many experiments, have been conducted to study blood droplet dynamics and some experiments use porcine blood [10, 14] as a substitute for human blood. It has been shown that porcine blood and human blood share very similar characteristics with regards to density, surface tension and viscosity. Porcine blood, therefore, is an acceptable substitute for human blood [26]. We study

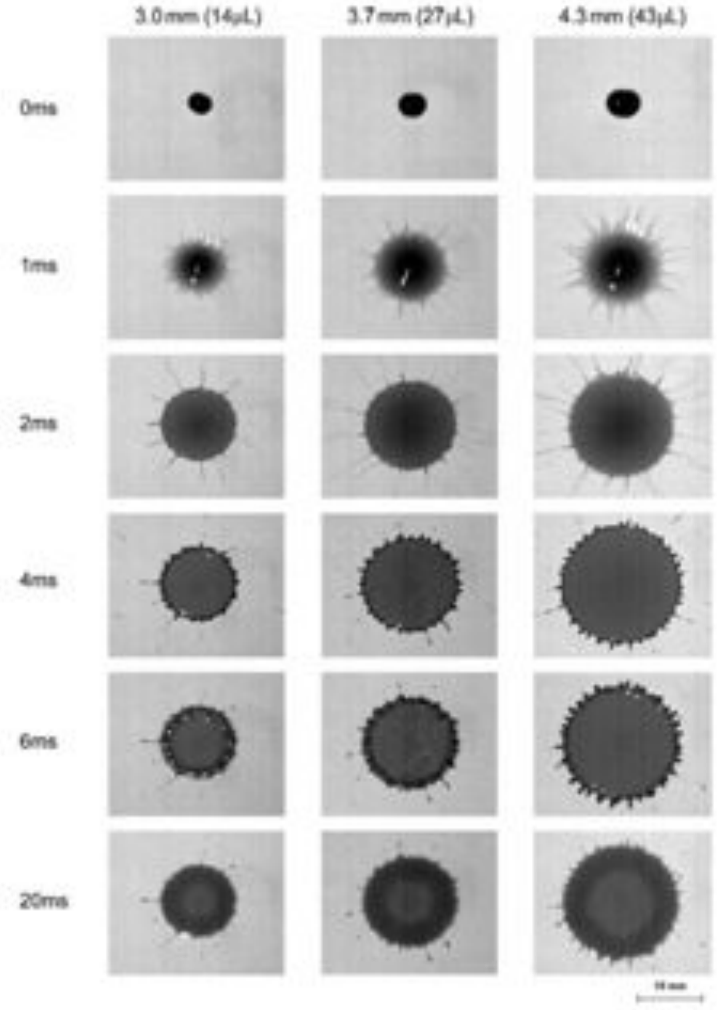

Figure 1.2: A series of high-speed photographs comparing the impact dynamics of three different porcine blood droplet diameters falling onto paper [10].

different blood droplet dynamics than those explored in [10, 22, 23]. For the purposes of our model, we focus on the dynamics of blood droplet flight and the parameters that are involved in creating the unique forward trajectories each droplet has when it emerges from the ballistics gel.

1.2 Existing Methods for Bloodstain Pattern Analysis

The current methods for finding the location of the bloodletting event responsible for a bloodstain assume that blood droplets travel in a straight line. The most common method is the *String Method* [11]. In this method, an investigator aligns a string with the major axis of an elliptical stain of an upward moving droplet and pulls the string back according to the impact angle (see Equation 5.1) calculated using the dimensions of the stain. When using the *String Method*, the investigator will not use bloodstains of droplets that are moving downward once the droplet hits the surface. When a string is pulled back according to the impact angle of a droplet that is moving downward, the string will extend upward in a straight line falsely indicating that the source of that droplet is in the ceiling. Thus investigators will predominately ignore downward moving droplets when using the *String Method* or use them with caution. We call such methods, *straight line geometric reconstruction* of bloodstains.

Figure 1.3 shows that droplets appear to be moving sideways and these can give misleading results as their strings are pulled away from the source of bloodletting. These droplets are not moving sideways but could be experiencing a radial distortion as the droplet impacts the surface. Raymond *et. al.* describes these droplet vibrations as follows [25]:

> A spherical droplet striking a surface at an angle produces an elliptical stain. The same stain can be produced by an elliptical drop striking the surface perpendicularly... It has been shown experimentally that the natural mode of vibration of a spherical droplet is ellipsoidal... Initial experimentation has shown that for at least 15 cm of drop travel, there are indications of droplet break-up, some spinning—particularly where the drop has a dumbbell-like shape—and considerable deformation of the shape in some instances.

Oscillatory radial distortions of blood droplets are discussed further in Section 5.2.4. Work has been done to improve straight line geometric reconstruction methods by accounting for gravitational force. In particular, Knock and Davidson have investigated the source of angled bloodstains and they use the gravitational force in a two-dimensional model [14], but neglect air resistance and the oscillation of the blood droplet.

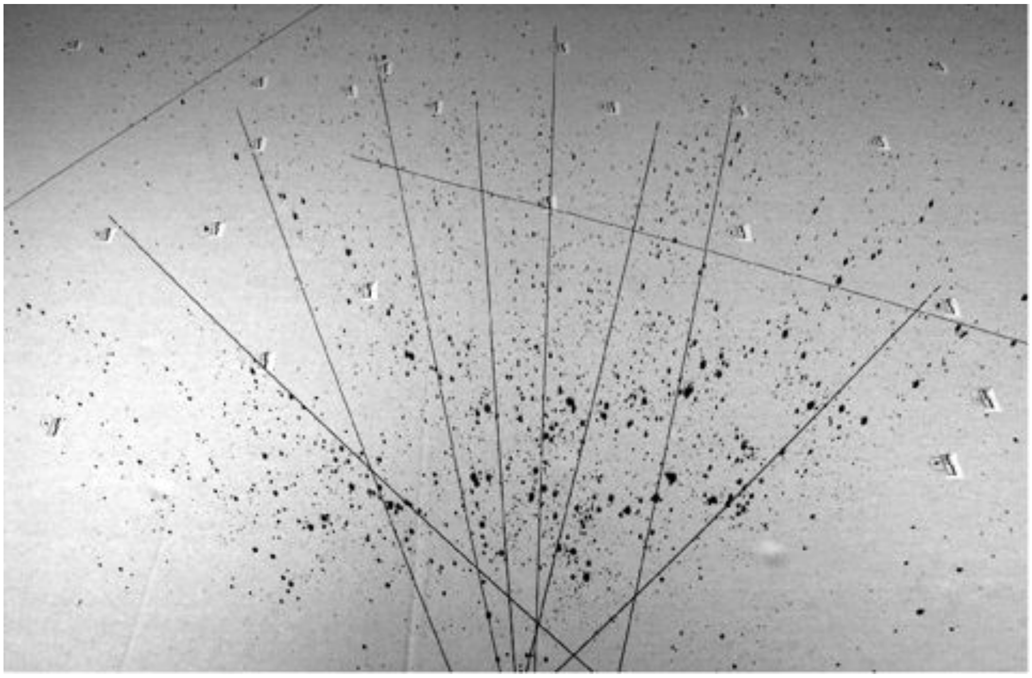

Figure 1.3: The String Method [11]. The strings are aligned with the major axis of a selected droplet and are pulled backward out of the page according to the angle of impact. The origin of bloodletting is out of view of the camera. Some strings are being pulled away from the origin of bloodletting because those droplets are not moving strictly upward.

BACKTRACK™, developed by Carter [11], is a Bloodstain Pattern Analysis (BPA) software package that implements the straight line geometric reconstructions of blood droplet trajectories. This program estimates the coordinates of the source of the bloodletting event in a horizontal plane with sufficient accuracy [11]. However the height estimates of the source of the stain are used with caution because of the uncertainty in downward moving droplets. Figure 1.4 shows downward moving droplets coming from a bloodletting source in the ceiling. Without the three virtual strings (shown in the side view screen capture in Figure 1.4) from upward moving droplets, the area of convergence would be incorrect.

Recently, Maloney developed a three-dimensional BPA software package called *HEMOSPAT™* [17, 18]. This package has a feature that gives investigators who are not at the scene the ability to measure the dimensions of an actual stain from a digital photograph as shown in Figure 1.5a. The user can also invert the colours of the photograph if necessary (Figure 1.5b). Similar to *BACKTRACK™*, this software package is also based on straight line geometric reconstructions (Figure 1.6).

A major disadvantage of both packages is their confinement to straight line geometric reconstructions, *i.e.*, the lack of the drag force and gravitational force in their models. Straight line geometric trajectory reconstructions may be acceptable for bloodstains that are a very short distance from the bloodletting event [5], but in the situations where the bloodstains are far from the source of bloodletting or the stain is incomplete (from moving a piece of the crime scene for instance), a model accounting for drag and gravity is needed. It is unclear what distance constitutes a bloodstain being far or close to the source of bloodletting but Buck *et. al.* states that if the impact angle (measured from the horizontal plane) "exceeds 10 °, ballistic analysis is recommended". Buck *et. al.* also states [5]:

> In the case of bloodstains, which are located [sic] longer distance from the blood drop origin, the straight line was sited [sic] up to 2m higher than the ballistically determined trajectory of the blood drop in the area of origin of the bloodstains. These results demonstrate that a ballistic determination of the trajectories is necessary.

In the same article [5], a three-dimensional, bloodstain documentation procedure is presented. Unlike the String Method, the investigator does not need to connect strings to the bloodstain. Instead a laser scans the crime scene for bloodstains and records their

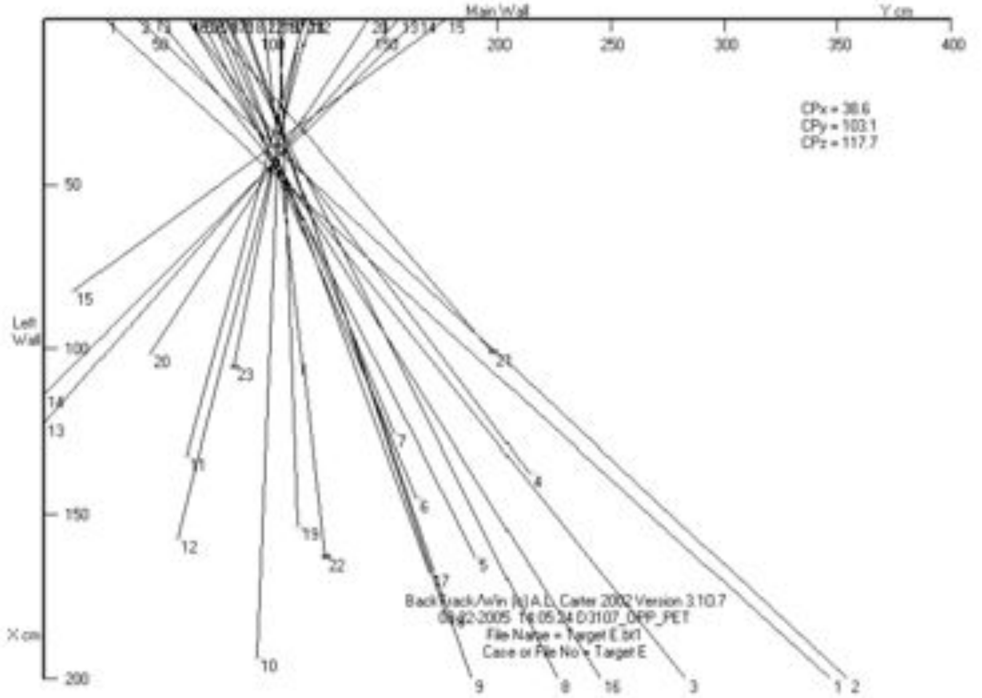

(a) An overhead view where the blood droplets are moving from bottom to top.

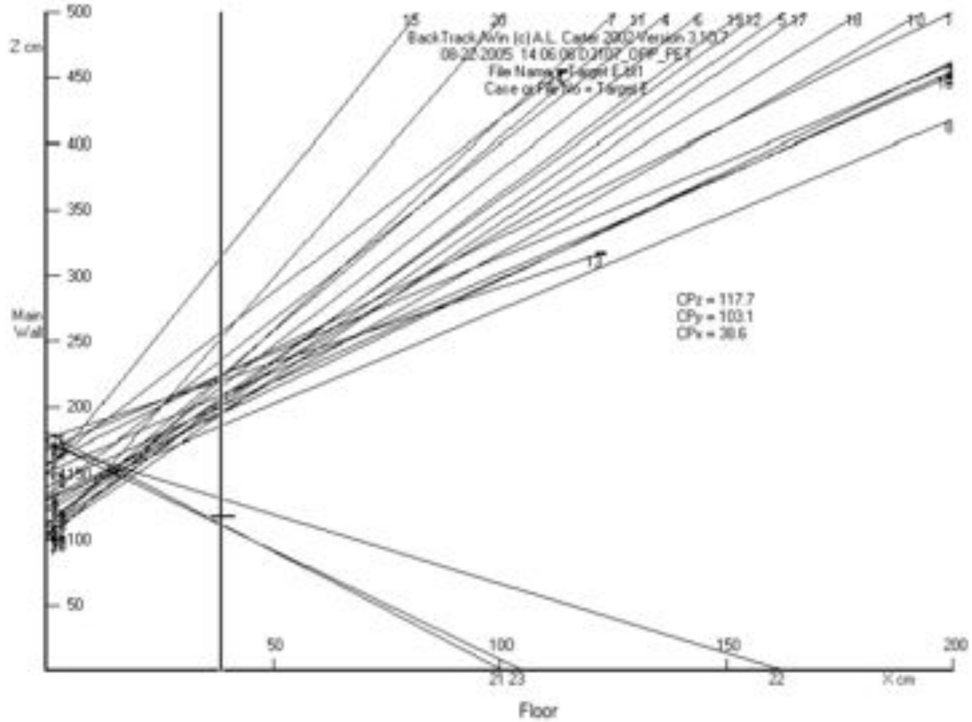

(b) A view from the side where the blood droplets are moving from right to left.

Figure 1.4: Screen captures of trajectory reconstruction produced by *BACKTRACK™* [11].

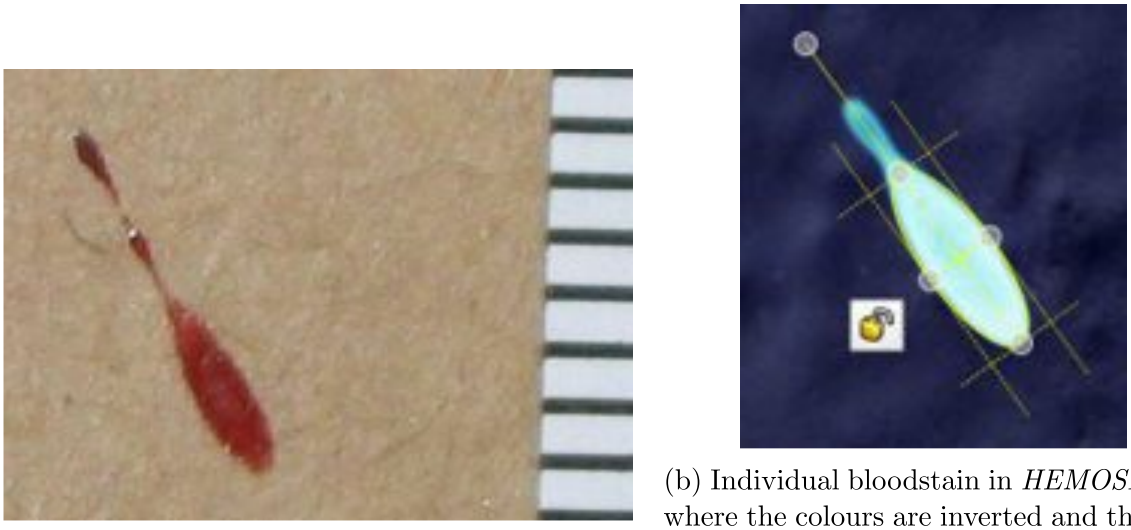

(a) Photograph of bloodstain of an individual blood droplet from a crime scene.

(b) Individual bloodstain in *HEMOSPAT™* where the colours are inverted and the major and minor axes have been identified by the user.

Figure 1.5: *HEMOSPAT™* stain identification (see [16])

sizes and positions. Buck *et. al.* presents a model, also based on straight line trajectory reconstructions, which is used for bloodstains close to the source of bloodletting and an external software provides a ballistic computation for droplets farther from the origin. Also, while the user can provide a desired drag coefficient, the value of drag used by default is noted to be the drag of a rigid sphere of diameters 1 millimetre to 3 millimetres. In summation, the three software packages we found for bloodstain pattern analysis, all use straight line geometric reconstructions. However the model offered in [5] uses external software to reconstruct the trajectories of droplets that are far from the source of bloodletting and would likely have a curved trajectories alongside straight line geometric reconstructions for blood droplets that are close to the source of bloodletting. *HEMOSPAT™* and *BACKTRACK™* both rely on straight line reconstructions of upward moving blood droplets and the region of intersection to find the source of blood letting. See [8] for a comparison between the software packages *HEMOSPAT™* and *BACKTRACK™*.

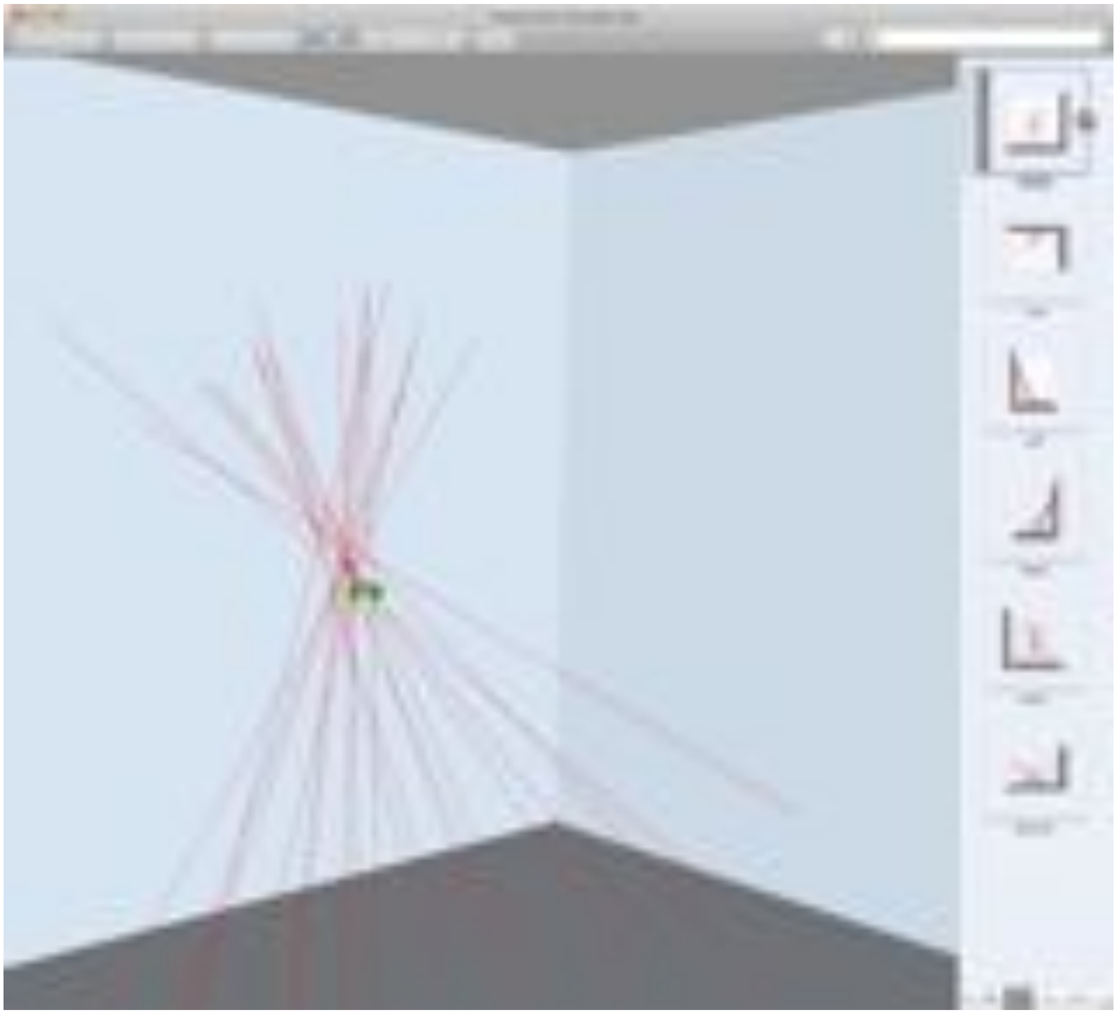

Figure 1.6: Screen capture of the interface for *HEMOSPAT™* [16]. This is a three-dimensional view of the droplet paths. The droplets are moving into the page toward the left wall.

We present a model that does not use straight line geometric reconstruction. Our model incorporates the force of gravity and the effects of drag on a blood droplet. In Chapter 2 we discuss the procedure of producing the bloodstains via a simulated bloodletting event where the position of the target and the weapon used are known. In Chapter 3 we discuss briefly how to track the droplets in the stereo video data and how the paths of the blood droplets are reconstructed. These experimental path reconstructions are used in an objective function which is the Euclidean distance between the experiment path reconstruction and a trajectory produced by our model. We use an optimisation solver to minimise this objective function. Chapter 4 shows the results from fitting our model to the experimental path reconstructs and also shows the distributions of drag coefficients and Reynolds numbers found by our model. Lastly, Chapter 5 has conclusions about our work and a discussion of future research.

Chapter 2

Laboratory Simulations of Bloodletting Events

We construct laboratory experiments of realistic bloodletting events using blood filled gel targets. The position of the target is known and it is shot by a paintball gun loaded with a riot ball. The high-speed stereo cameras record the shooting of the ballistics gel and record the blood droplets flying through the air as they exit the ballistic gel. The collected video is used by the software from [30] to produce trajectory reconstructions of the blood droplets coming out of the ballistics gel. The properties associated with the paths of individual droplets are analysed by the model described in Chapter 3. Each experiment takes about 30 minutes to perform from start to finish and each experiment generates approximately 6 gigabytes of video and photographic data.

2.1 Outline of Procedure for Laboratory Experiments

The laboratory procedure used to generate videos of simulated bloodletting events is as follows. The details of specific calibration processes are outlined in Section 2.3 and each item of the laboratory procedure is briefly described in a paragraph below the list.

1. Prepare the mock crime scene and recording equipment.
2. Calibrate the recording equipment.
3. Run the laboratory experiment.
4. Document and verify the experiment.

Preparing the mock crime scene (see Section 2.2) begins with fixing surface materials on walls using clamps. These surfaces include carpet or cardboard or the default white laminated plywood. High frame rate stereo camera pair is turned on and the *Mega Speed*™ high-speed software is started, and the cameras are tested to ensure that all wire connections from the cameras to the laptop are functioning.

There are three types of calibration videos captured in this experiment, the moving checkerboard calibration video, the moving laser dot calibration video, and the riot ball calibration video. Before the shooting of the ballistics gel all three calibration videos are captured. The first calibration video recorded is the moving checkerboard calibration (see Section 2.3.1). The second calibration video that is captured is the moving laser dot calibration (see Section 2.3.2). Next, both calibration videos are analysed by the calibration software to fix the coordinate system used by software from [30]. Once the coordinate system is fixed the camera capture speed and mock crime scene lighting is adjusted for the riot ball calibration. This calibration video captures a riot ball falling into the mock crime scene (see Section 2.3.3). This video is used for determining the downward direction needed for the software from [30].

After camera calibration is completed, the laboratory experiment can proceed (see Section 2.4). The ballistics gel target is mounted onto the lab jack. We ensure that the riot ball travels directly through the gel and hits the blood package suspended inside the ballistics gel target. Next we press the video synchronisation trigger, shoot the target with the paintball gun and capture the experimental video.

After the shooting of the ballistics gel, the resulting bloodstains are photographed. Then the calibration using the moving laser dot is repeated to ensure that the cameras have not moved during the experiment, say due to recoil from the gun, invalidating the calibration. All the videos are archived and labelled with dated filenames. If during the experiment anything unexpected occurs (i.e. the riot ball ricochets off the lab jack or the riot ball did not pass through the gel completely or droplets from the experiment all moved in one general direction) it is noted in a text file that goes along with the videos (see Section 2.5).

The list of materials needed to set up the mock crime scene and create the ballistic gel targets are listed in Table 2.1. Some items in this table are reused for each experiment but some items (specifically the targets) were remade for each experiment.

2.2 Preparing the Mock Crime Scene

The laboratory experiments are set up on a steel table $0.9\,\mathrm{m} \times 3.0\,\mathrm{m}$ where three $1.2\,\mathrm{m} \times 1.2\,\mathrm{m}$ laminated plywood boards with a white vinyl finish are propped up against the table opposite each camera to simulate the corner of a room (see Figure 2.1). Notice that two plywood boards are propped up, next to each other, on the same side of the table, and the last plywood board is perpendicular to the other two. Camera A faces the two adjacent plywood boards and Camera B faces the last plywood board perpendicular to the direction of the riot ball being fired. Different surfaces can be clamped onto the walls to observe the resulting bloodstain pattern. In our experiments we use the white laminated plywood surface extensively. For two experiments (one with transfer blood

Table 2.1: Materials for reconstructing experiment

Category	**Item**	**Quantity**
Camera	*Mega Speed* ™ high-speed camera	2
	Camera trigger	1
	25mm camera lens	2
	Camera tripods	2
	Gigabit network switch	1
	60cm × 45cm sheet of plexiglass	2
Lights	500 watt halogen work lights	14
	Tripod light stands	5
Target	600mL beakers	6
	Popsicle sticks	2
	Gelatin	40-50g
	Thin string	approx. 30cm
	Latex wrap	1
	Hot plate	2
	Stirring rod	1
	Syringe	1
	Triple beam balance	1
	Transfer blood	15-20mL
Weapon	Paintball gun	1
	Hollow plastic 1.71 cm diameter riot balls	1
Crime Scene	Clamps	16 (minimum)
	Lab jack	1
	1.2m × 1.2m sheet of plywood with white vinyl finish	3
	Cardboard, carpets, other surfaces	2 (one for each wall)

and the other with pig blood), we used cardboard as the surface. The blood runs a lot more on the laminated plywood than on the cardboard, as expected. Experiments using carpet (brown and green) surfaces are unsuccessful because the blood droplets soak into the carpet immediately after the bloodletting event and thus cannot be photographed. On an actual crime scene, investigators will not be taking the photographs of bloodstains immediately after the crime takes place but on surfaces like walls that have been painted or carpet or wallpaper, the bloodstains may retain their shape and not run along the walls. This will be discussed further in Chapter 5. When we took the photographs of the resulting bloodstains we were looking to photograph the stains before they were distorted from the running of the blood so that this photographic data could be used in future research.

The target is a thin latex packet containing either porcine blood or transfer blood encased in gelatine and raised off the table with a lab jack (seen in Figure 2.1 as item B). The ballistics gel is a simulation of human flesh and the blood suspended inside the gel is a simulation of the blood inside a human body. The latex blood package is suspended in the beaker before the gelatine begins to harden and then placed in the refrigerator for 24 hours. The amount of each material is listed below:

- 15-20mL of blood
- 40g of gelatine powder
- 500-600mL of water

Directly behind the target sits the paintball gun loaded with a single riot ball for each experiment. The riot ball has a radius of about 0.5 centimetres. The muzzle velocity of the paintball gun is approximately 100 metres per second. The blood droplets emerge from the ballistics gel at less than 10 metres per second. The crime scene setup is shown in Figure 2.1 where the paintball gun is shown as item A.

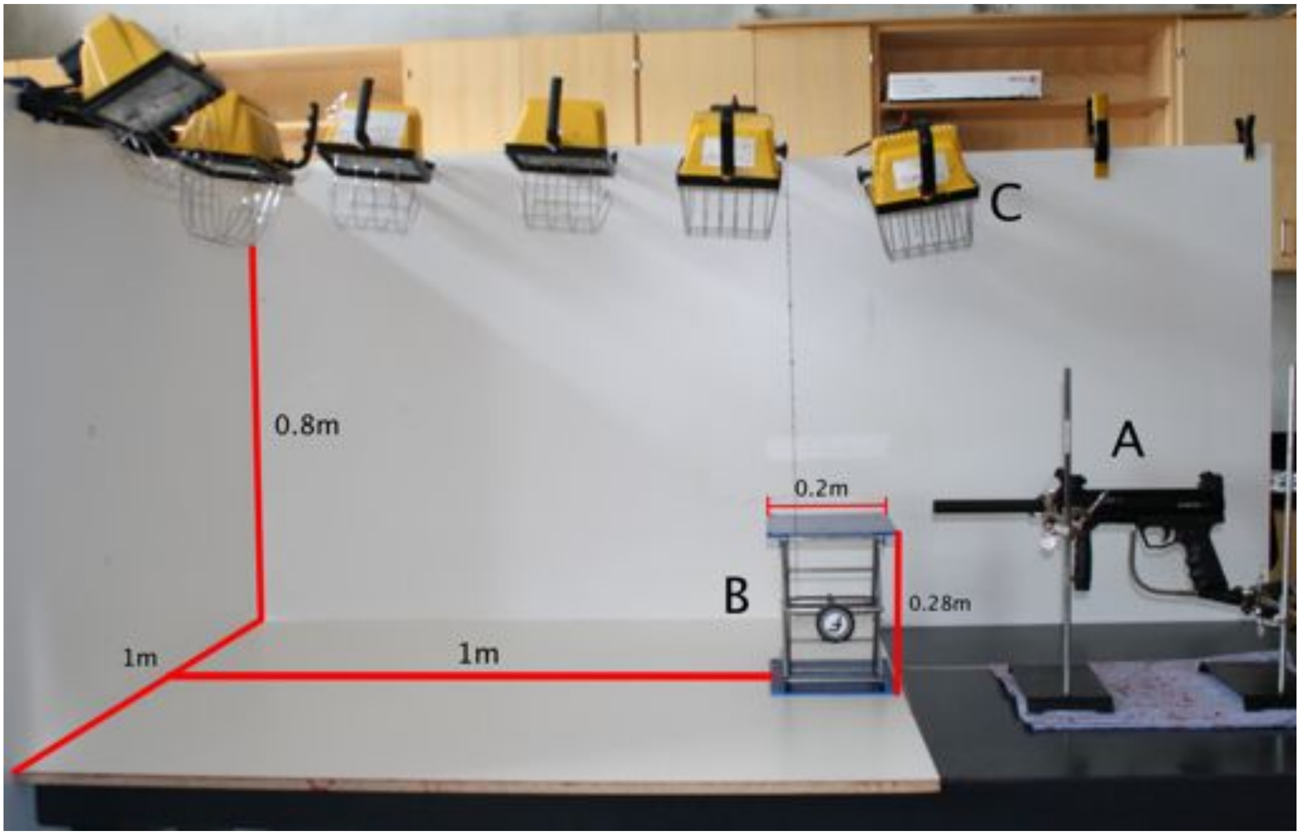

Figure 2.1: Placement of lab jack and paintball gun within the crime scene. A) paintball gun used as a weapon. B) Lab jack on which the ballistics gel is placed in front of the paintball gun. C) Halogen 500W work light.

The placement of the two high-speed cameras is shown in Figure 2.3. Both high-speed cameras are capable of recording videos at 1300 frames per second. One high-speed camera, protected by plexiglass, is mounted on a separate table behind the paintball gun and off to the side (Camera B in Figure 2.3). It is raised above the paintball gun and angled vertically to gain a good perspective of the left and right motion of the blood droplets. The paintball gun, when fired, produces recoil that shakes the table it is placed upon. The high-speed camera, therefore, cannot be placed on the table directly behind the paintball gun because the recoil of the gun can shake the high-speed camera thereby invalidating the experiment. To avoid this, the high-speed camera is placed on its own table to the left of the paintball gun. The other high-speed camera—also protected by a sheet of plexiglass—points in a direction perpendicular to the path of the riot ball (Camera A in Figure 2.3).

The cameras are connected together via a synchronisation trigger. Both cameras are set to *single trigger continuous capture mode* in the *Mega Speed™* high-speed software which means that both cameras will begin capturing when the trigger is pressed, and will continue capturing until the camera buffer is full. The actual shooting of the ballistics gel will take no longer than a second. The cameras will normally capture the few seconds before and after the trigger is pulled filling the camera buffer. Once the videos are captured and saved, the beginning and end of the video clip will be trimmed since the actual experiment occurs in the middle two seconds (maximum) of the video. Lighting is provided by fourteen 500W work lights (seen in Figure 2.1 as item C) allowing the cameras to produce usable videos even at frame rates above 1000 frames per second.

Within the high-speed camera software there is a setting called *camera gain* which controls the quality of the videos captured. Higher gain values give lower quality videos so in order to capture higher frame rate videos we could either use higher gain or more illumination. We opt not to sacrifice the quality of the videos and thus use a higher intensity of light. We use AC light sources and observe the light flickering in the videos because the capture speed is sufficiently high. This flickering is accounted for by the droplet tracking software from [30] (see Chapter 3).

2.3 Calibrating the Recording Equipment

In a previous version of this experiment, only one high-speed camera records the coordinates of the blood droplet trajectories in the vertical plane. This setup can be seen in Figure 2.4. This experiment shows that the blood droplets do indeed travel in curved trajectories.

For this single camera experiment, the tracking of individual blood droplets is done by

Figure 2.2: The full laboratory setup without markup.

hand (shown in Figure 2.5). The current version of this experiment uses two cameras which allows for the three-dimensional reconstruction of the paths of the blood droplets as they come out of the ballistics gel. Both cameras are connected to a trigger, as mentioned above, which is connected to a laptop for video synchronisation.

The tracking of droplets is difficult when using a stereo pair of high-speed cameras because finding a unique droplet in both videos is difficult. The synchronisation trigger is essential for tracking droplets because it would be nearly impossible to manually find a unique blood droplet in both videos without the synchronisation of the cameras. However, even with the trigger synchronising the two video signals, ensuring the droplet being tracked is the same in both videos would be virtually impossible to do with the *Mega Speed*™ software. It is infeasible to use manual tracking to reconstruct the paths of blood

Figure 2.3: The position of Camera A and Camera B with respect to the mock crime scene. Camera A is oriented perpendicular to the direction of shot riot ball. The view of Camera B is not exactly parallel with the direction of the shot riot ball but is oriented overhead the placement of the ballistics gel.

droplets in the videos provided by stereo cameras, hence we use a three-dimensional blood droplet tracker provided by Zarrabeitia *et. al.* [30]. We discuss the use of this program in Chapter 3.

The tracking program developed Zarrabeitia *et. al.* [30] requires stereo camera calibration to estimate the three-dimensional trajectories of blood droplets. Most calibration is done before shooting the ballistics gel. However, there is also some calibration verification done after the shooting is completed, to ensure the cameras have retained their original position. The calibration program was provided by Zarrabeitia [30]. The calibration procedure is as follows:

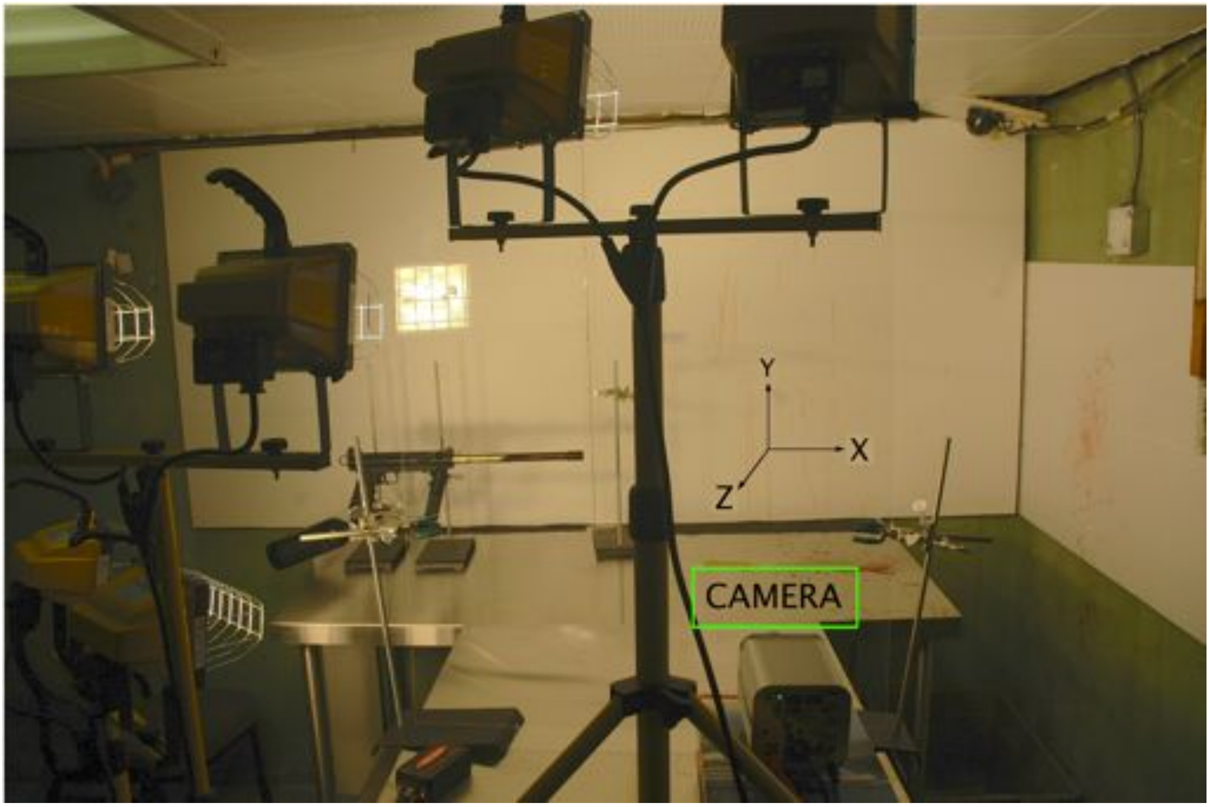

Figure 2.4: A single camera experiment. The high-speed camera is oriented perpendicular to the path of the projectile to capture the motion of the droplets in a vertical plane.

1. Capture the moving checkerboard calibration video
2. Capture the moving laser dot calibration video
3. Verify the accuracy of the above calibration videos using software from [30]
4. Capture the riot ball calibration video

2.3.1 Capturing a Moving Checkerboard for Calibration

Two checkerboard patterns with squares of size 3.35 cm × 3.35 cm are printed out and mounted on the walls of the mock crime scene to aid in the tracking of blood droplets (see Figure 2.7). Each checkerboard is positioned to be in the field of view of one of the two cameras. When the mounted checkerboards are laminated (for cleaning and reuse after

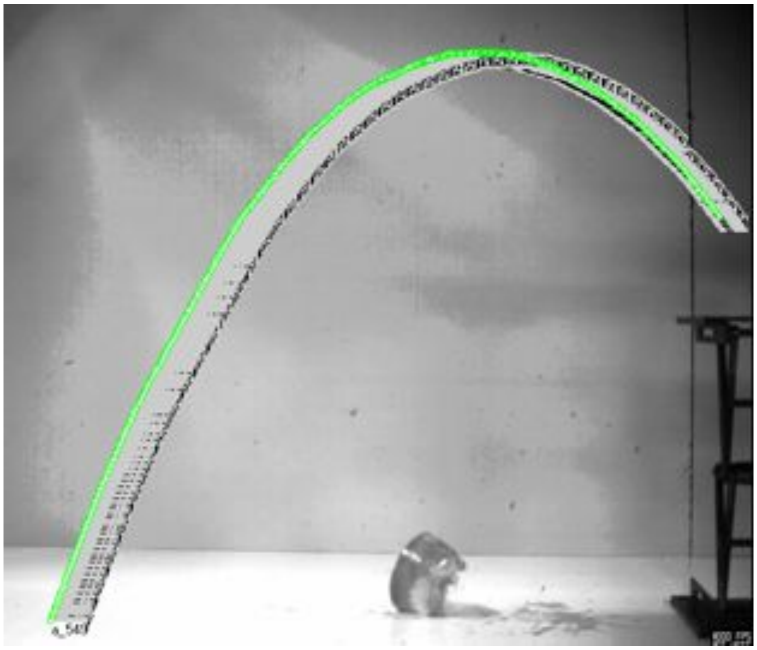

Figure 2.5: Manual tracking of a single droplet with *Mega Speed™* software [19]. Here, a single droplet is observed in 10 frames from a single camera and the position was marked by the user. The *Mega Speed™* software takes those ten points and applies polynomial interpolation to reconstruct the path.

each experiment) the reflection from the work lights prove to be counter productive for the droplet tracking software. Instead of laminated checkerboards a simple paper print out of the checkerboard is used for each experiment.

For the moving checkerboard calibration video the wall checkerboards are covered or removed. The reason for this is to ensure the calibration program is not confused between the moving checkerboard (see Figure 2.6) it should be analysing and the stationary checkerboards mounted on the walls of the mock crime scene. The camera is set to capture at 100 frames per second and the exposure time is set to 5 seconds. The flat checkerboard is moved around in the view of both cameras and both videos are analysed by a calibration program provided by Zarrabeitia *et. al.* [30]. Once it does this the calibration program will record the position of the cameras relative to each other. The coordinate system is chosen with Camera A (shown in Figure 2.3) at the origin and

Camera B will have a position relative to that origin. The size of this calibration video, from one camera, is about 220 megabytes.

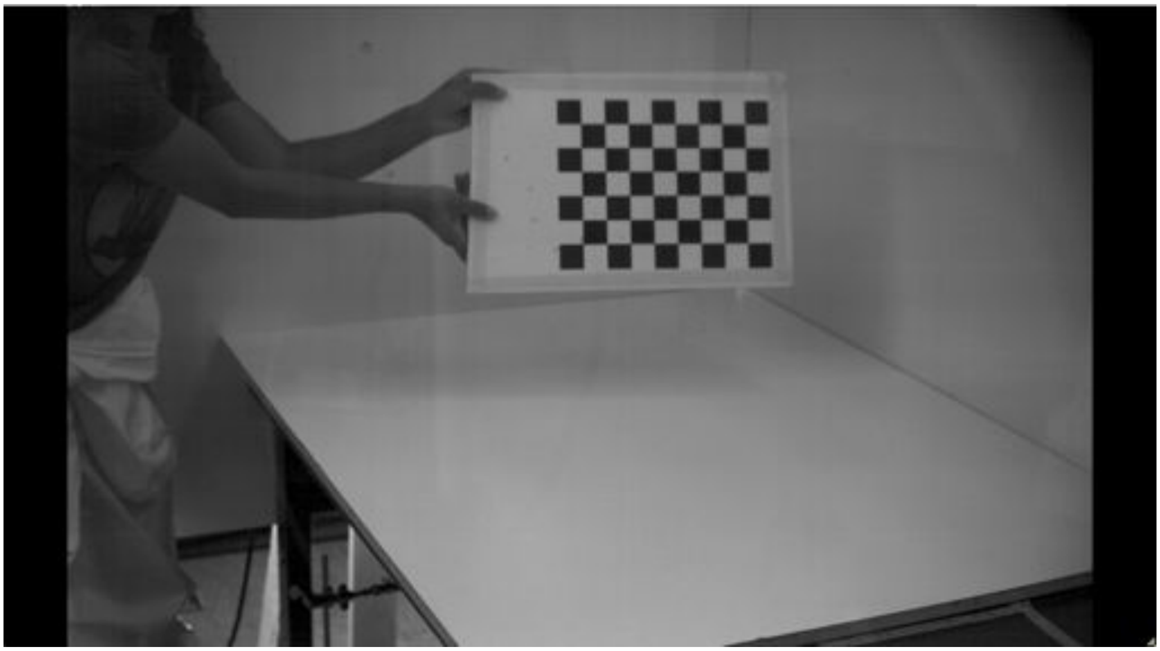

Figure 2.6: Still shot from a moving checkerboard calibration video. The checkerboard is moved around in the view of both cameras and the calibration program identifies the individual squares on the checkerboard. The image has been lightened to enhance contrast.

2.3.2 Capturing a Moving Laser Dot for Calibration

This calibration video is captured with just enough light to see the wall checkerboards. The camera settings are 100 frames per second and the exposure time is set to 5 seconds. The size of this video, from one camera, is approximately 730 megabytes. The laser dot must be the brightest object in each frame and it must be moved very slowly to avoid motion blurring. The objective here is to shine the laser at least once on all three planes of the experiment, trying to reach the edges and areas where the laser dot may be visible by only one camera.

The calibration program (from [30]) will circle the laser dot (in Figures 2.8 and 2.9

Figure 2.7: Still frame (as captured by both cameras) to illustrate the placement of the mounted checkerboards. Each camera captures only one checkerboard. In both views of the mock crime scene, the riot ball can be seen emerging from the ballistics gel. The figure on the left is a still shot from Camera B and the figure on the right is still shot from Camera A.

it is a thin blue circle) and a line (in Figures 2.8 and 2.9 it is a blue line) is plotted corresponding to the position of the laser dot in the other camera. The error is the distance between the line and the laser dot's position. Ideally the blue line should pass directly through the blue circle (as seen in Figure 2.9). The experiment will only proceed if the three-dimensional reconstruction of the laser dot's position matches the laser dot's actual position in the view of the camera. This laser dot verification is done before and after firing the paintball gun to ensure the cameras have not moved during the experiment. Figure 2.8 is an example of a failed experiment. The calibration verification did not pass because one or both cameras had shifted during the experiment. This can be caused by either recoil from the paintball gun or wires connected to the cameras being moved accidentally. Figure 2.9 is an example of a successful experiment. The calibration verification passed indicating that cameras did not move during the experiments.

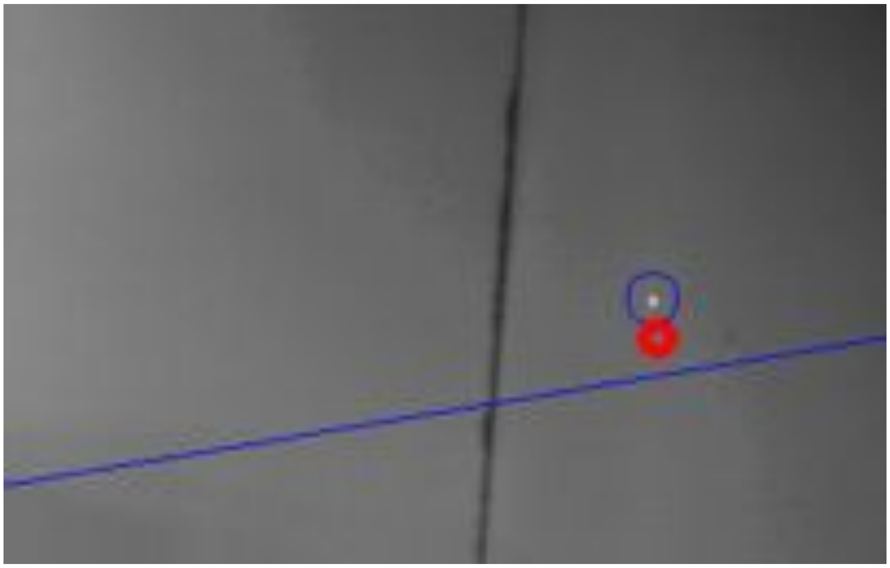

Figure 2.8: A screen shot of calibration verification. The blue circle shows the position of the laser dot and the blue line represents the line corresponding to the position of the laser dot in the other camera. The red circle shows the re-projection of the 3D reconstruction of the laser dot. In this case the calibration is inaccurate because the camera has somehow moved during the experimental procedure.

2.3.3 Capturing a Falling Riot Ball for Orientation

Figure 2.10 shows a still frame of the riot ball falling into the mock crime scene. This calibration is done right before firing the paintball gun. The camera is set to capture at 1300 frames per second and the exposure time is set to 100 microseconds. The size of this video, from one camera, is approximately 180 megabytes; the size is smaller because the length of this video is much shorter than the checkerboard calibration video or the verification of calibration video.

The function of the riot ball calibration video is to fix the direction of gravity. Once all the necessary calibration videos are saved and are processed by the calibration program the actual firing of the paintball gun can proceed.

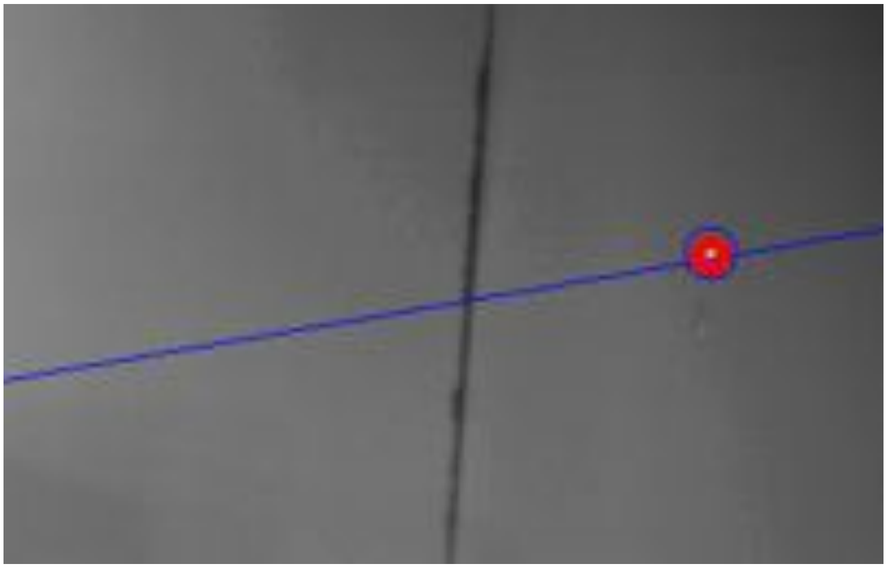

Figure 2.9: A screen shot of calibration verification. The blue circle shows the position of the laser dot and the blue line represents the line corresponding to the position of the laser dot in the other camera. The red circle shows the re-projection of the 3D reconstruction of the laser dot. In this case the calibration is successful because the camera has remained stationary during the experimental procedure.

2.4 Running the Experiment

The synchronisation trigger is pressed and the riot ball is fired at the ballistics gel target. The video of the shooting of the ballistics gel will normally be about 1 gigabyte in size, from one camera, and the camera settings will be identical to the directional calibration camera settings: 1300 frames per second; full illumination. The data provided from the droplet tracking software can be used to visualise the trajectories of blood droplets. Figure 2.11 shows the first one hundred droplets tracked in the porcine blood experiment.

2.5 Documenting and Verifying the Experiment

After each experiment a number of photographs are taken of the scene to record the final positions of the blood droplets on the walls and table for later use. Documenting an actual crime scene consists of four steps: note taking, videography, photography, and

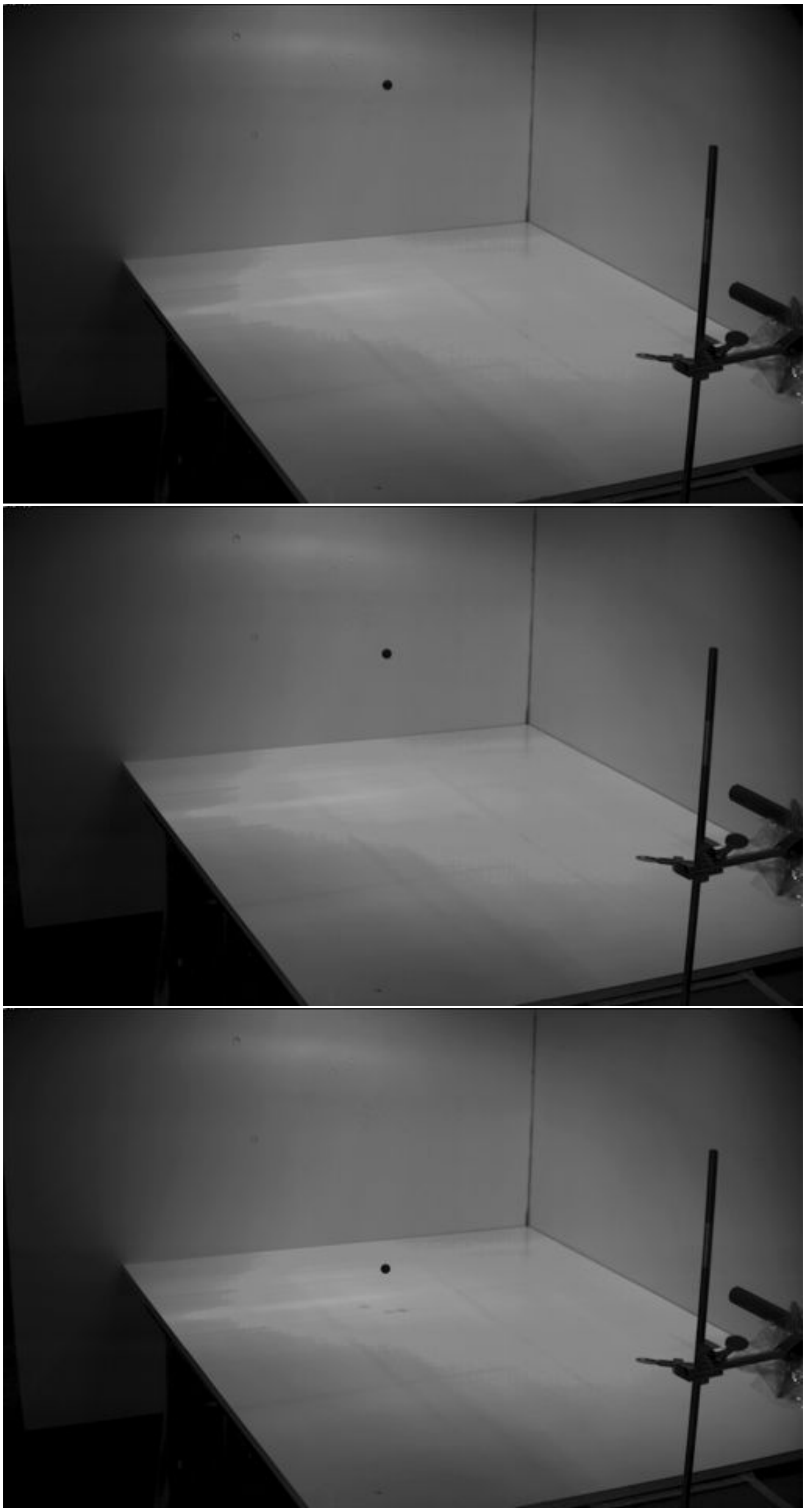

Figure 2.10: Riot ball (shown as the black circle) is dropped from above the mock crime scene and falls straight downward. The still shots also show the concentration of light focused into the corner of the mock crime scene

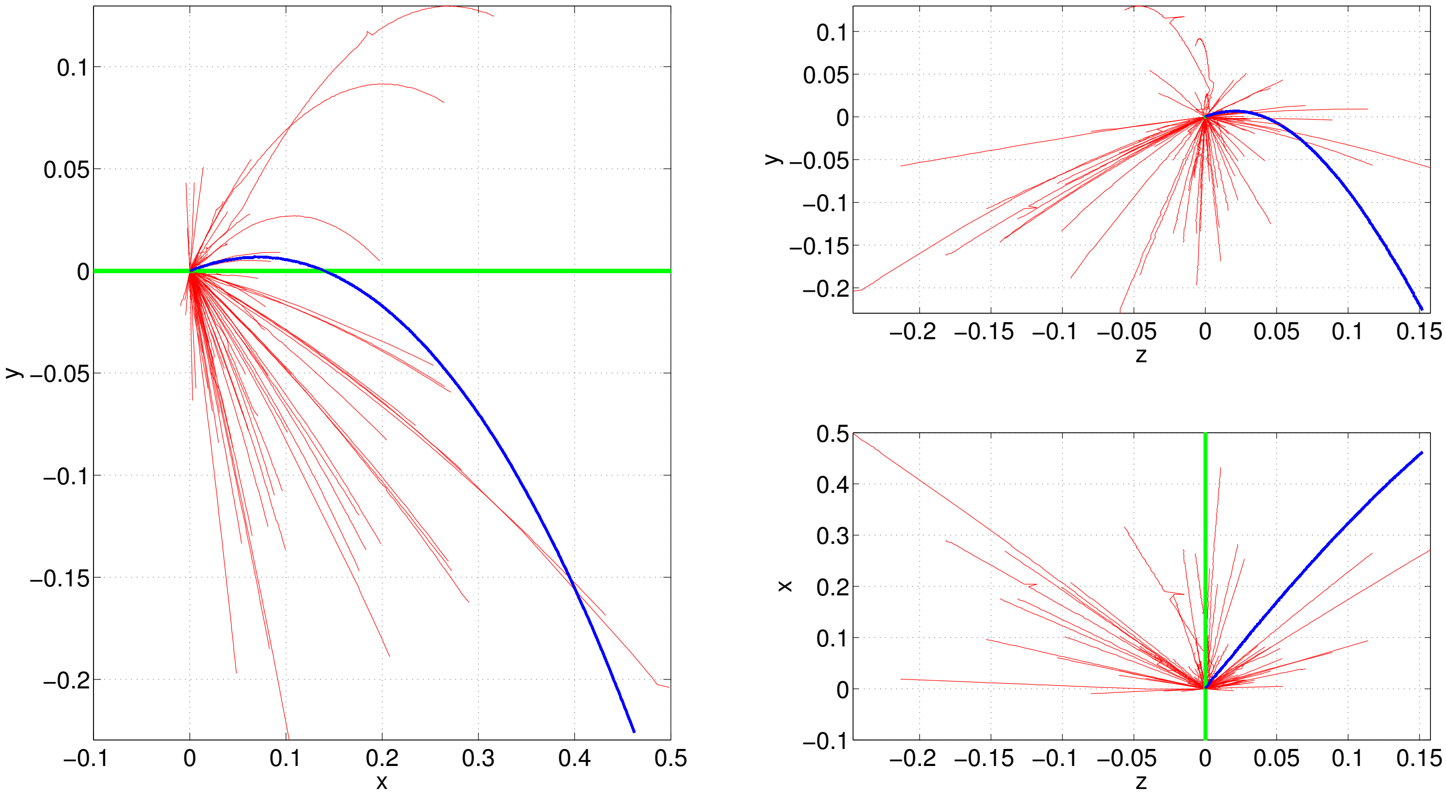

Figure 2.11: Visualisation of the trajectories from software provided by [30]. The left figure is a view of the xy-plane or side view, the top right figure is the zy-plane or a view from behind the gun, and the bottom right figure is a view of the xz-plane or an overhead view. The thick green line is the path of the riot ball.

sketching [13]. Since we have a controlled laboratory experiment where the position of the weapon is known, the only documentation we collected was photography of the resulting bloodstain. While photographs of a crime scene should be taken with a camera equipped with 35mm lens and other auxiliary lenses available, all the pictures of the crime scene are taken with a Sony Cyber-shot DSC-W210 digital camera. The primary use of the photos captured after each experiment is to make a visual validation of the droplet tracking in that specific experiment. It will also serve a purpose in later research, notably the inverse problem (see Chapter 5).

(a) A digital photograph from the perspective of Camera A.

(b) A digital photograph from the perspective of Camera B.

(c) A digital photograph of the ballistics gel including the checkerboard in the field of view of Camera A.

(d) A digital photograph of the ballistics gel including the checkerboard in the field of view of Camera B.

Figure 2.12: Final photos of the mock crime scene using transfer blood.

Before cleaning up the bloodstain pattern from the mock crime scene walls or removing the surfaces a laser is once again shined in a random pattern on the surfaces of the mock crime scene and a video is recorded. The digital photographs are taken before the laser dot video is captured because the blood has a tendency to run on the laminated plywood walls. This video is analysed using the calibration software [30]. If the verification fails (as shown in Figure 2.8) the experiment is discarded and the entire procedure must start over. If the verification passes, the videos are processed by the software from [30] once they are suitably dated and labeled.

Chapter 3

Modelling Trajectories of Blood Droplets

As mentioned in Chapter 1, our objective is to study blood droplet flight dynamics after a bloodletting event. In this chapter we outline the model used to simulate the flight of blood droplets after a bloodletting event (see Chapter 2). The model is used to calculate the exact parameters (in particular, the drag coefficient, the radius, the initial direction and the initial speed) associated with individual droplets. The parameters are determined via the solution of an optimisation problem. The objective function in the optimisation problem is the Euclidean norm of the difference between two vectors: one consisting of points in a reconstructed trajectory and the other consisting of corresponding points produced by the integration of the ordinary differential equation that models the blood droplets motion through the air.

For convenience we provide two tables summarising our notational conventions. Table 3.1 lists parameters associated with individual blood droplets together with some variables that would be measured by an investigator in a crime scene, which is discussed in Chapter 5. Table 3.2 lists known empirical values that we use in our model. Also, see Figure 3.1, for the coordinate system we are using in this model. While this coordinate system is unorthodox, it is the simplest right handed system to use with the high-speed cameras in the laboratory experiment.

Table 3.1: List of notation

Symbol	**Description**	**Units**
κ	drag coefficient	dimensionless
r	radius of a droplet	m
Re	Reynolds number	dimensionless
u_0	speed	ms^{-1}
A	cross sectional area	m^2
θ	polar angle (on the xy plane)	radians
ϕ	azimuthal angle (on the xz plane)	radians
α	impact angle on the surface (see Chapter 5)	radians
γ	glancing angle (see Chapter 5)	radians
β	string angle (see Chapter 5)	radians

Table 3.2: List of constants and known values

Symbol	**Value**	**Description**	**Units**
g	9.80665	acceleration due to gravity	ms^{-2}
ρ_{air}	1.1839	density of air at 25°C	kgm^{-3}
ρ_{pig}	1062	density of porcine blood [26]	kgm^{-3}
ρ_{sim}	1153	density of transfer blood (calculated in lab)	kgm^{-3}
μ_{air}	1.8616×10^{-5}	dynamic viscosity of air at 25°C	Nsm^{-2}
μ_{pig}	4.8×10^{-3}	dynamic viscosity of porcine blood [26]	Nsm^{-2}
σ_{pig}	5.6×10^{-3}	surface tension of pig blood [26]	Nm^{-1}

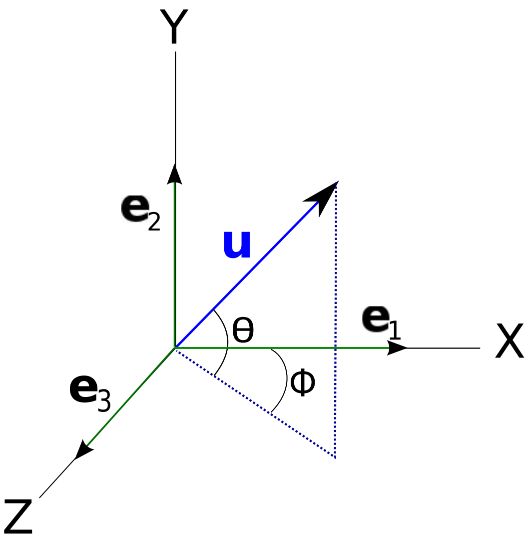

Figure 3.1: Coordinate system used in our model with velocity vector **u**, azimuthal angle ϕ and polar angle θ. The origin of the coordinate system is the centre of the ballistics gel in the laboratory experiment.

3.1 Models of Aerodynamic Drag

3.1.1 Using Navier-Stokes Equations to describe non-Newtonian Fluids and the Reynolds Number

The standard form of the Navier-Stokes Equation which describes the motion of a fluid is:

$$\rho\left(\frac{\partial \mathbf{u}}{\partial t} + \mathbf{u}\cdot\nabla\mathbf{u}\right) = -\nabla p + \nabla\cdot\boldsymbol{\tau} + \mathbf{q}, \tag{3.1}$$

where ρ is the density of the fluid, $\mathbf{u}$ is the velocity of the flow, p is the pressure, τ is the stress tensor, and $\mathbf{q}$ represents any external forces acting upon the fluid. The divergence of the stress tensor, $\nabla\cdot\boldsymbol{\tau}$, from Equation 3.1 is known as the viscous term while $\rho\mathbf{u}\cdot\nabla\mathbf{u}$ from the left hand side of Equation 3.1 is known as the inertial term. The Reynolds number, Re, (see Section 3.1.2) is derived from the ratio of the inertial terms to the viscous terms.

The laboratory experiments, described in Chapter 2, use two different types of blood: simulated (or transfer) blood which is a fluid with Newtonian properties and porcine blood which exhibits non-Newtonian fluid properties, similar to human blood. The stress tensor, τ, for a Newtonian fluid, is linearly proportional to the rate of strain tensor $\mathbf{D}$ thus,

$$\tau = \mu \mathbf{D}, \tag{3.2}$$

where μ is the dynamic viscosity of the fluid. For non-Newtonian fluids, the relationship in Equation 3.2 is not linear. In fact, the dynamic viscosity is a function of pressure, temperature and the rate of strain.

3.1.2 Reynolds number: Re

The Reynolds number, Re, is a ratio of inertial forces to viscous forces in a fluid. The inertial forces characterise how much a fluid resists a change in motion. The viscous forces are associated to the rate of change of a fluid's viscosity over time. Therefore, the Reynolds number is used to characterise a fluid's flow behaviour. For instance, low Reynolds numbers (where the viscous force is dominant) would characterise laminar or smooth fluid flow. Higher Reynolds numbers (where the inertial force is dominant) would characterise turbulent fluid flow. Acheson describes the Reynolds number in [1] as

$$\mathrm{Re} = \frac{\rho U L}{\mu}, \tag{3.3}$$

where L, U, ρ, and μ are characteristic scales of length, speed, fluid density, and dynamic viscosity, respectively.

For our purposes, we treat the droplet as a rigid sphere with the air flowing around it. As in [15], the Reynolds number that characterises this flow is

$$\mathrm{Re} = \frac{2\rho_{\mathrm{air}}\|\mathbf{u}\|r}{\mu_{\mathrm{air}}}. \tag{3.4}$$

In Equation 3.4, the characteristic length is $2r$ (twice the radius of the droplet), the characteristic speed is $\|\mathbf{u}\|$ (the speed of the droplet moving through the air), and ρ_{air} and μ_{air} are, respectively, the density and the dynamic viscosity of air. Despite the small radius of the droplet and the low initial speed of the droplets the density of air proves to be large enough and the dynamic viscosity of air small enough to force the Reynolds number to be greater than 1. Figure 3.2 presents a graph of the Reynolds number as a function of speed for droplets of distinct radii.

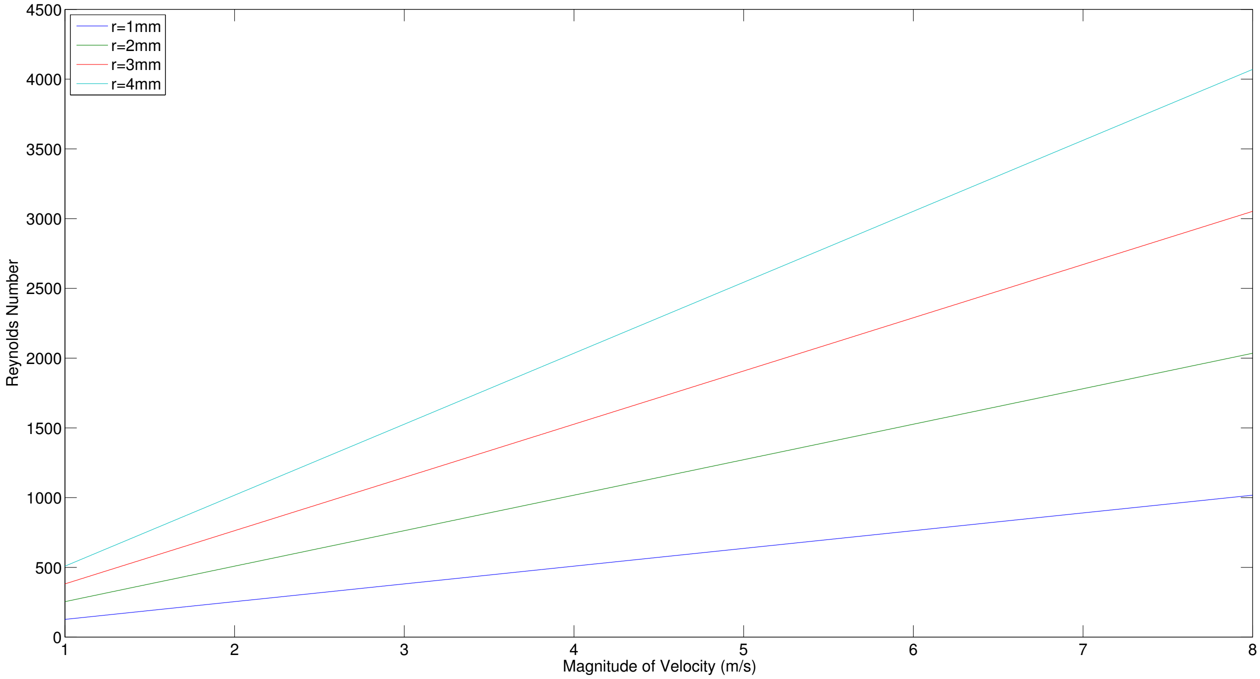

Figure 3.2: Reynolds numbers calculated via Equation 3.4 using four different radii and over $1\,\mathrm{ms}^{-1} \leq \|\mathbf{u}\| \leq 10\,\mathrm{ms}^{-1}$. This plot was made using the density and dynamic viscosity of porcine blood.

3.1.3 Stokes' Flow

When the Reynolds number is small (*i.e.*, $\mathrm{Re} \ll 1$), the resulting flow is referred to as Stokes' flow. Stokes' law characterises the drag force on a rigid sphere immersed in a fluid undergoing Stokes' flow (see [3]). The drag force, $\mathbf{F}_d$, on a sphere in Stokes' flow is written as

$$\mathbf{F}_d = 6\pi r \mu_{\text{air}} \|\mathbf{u}\|. \tag{3.5}$$

We are interested in the drag coefficient associated with the drag force in Equation 3.5. According to Batchelor [3],

> It is common practice to express the forces exerted on moving bodies by the fluid in terms of a dimensionless coefficient obtained by dividing the force by $\frac{1}{2}\rho U^2$ and by the area of the body projected on to a plane normal to $\mathbf{U}$.

In our case, we divide the force (Equation 3.5) by $\frac{1}{2}\rho_{\text{air}}\|\mathbf{u}\|^2 A$ to obtain the drag coefficient, κ, as follows:

$$\begin{aligned}
\kappa &= \frac{\mathbf{F}_d}{\frac{1}{2}\rho_{\text{air}}\|\mathbf{u}\|^2 A} && \text{(3.6a)}\\
&= \frac{6\pi r \mu_{\text{air}}\|\mathbf{u}\|}{\frac{1}{2}\rho_{\text{air}}\|\mathbf{u}\|^2 \pi r^2} && \text{(3.6b)}\\
&= \frac{12\mu_{\text{air}}}{\rho_{\text{air}}\|\mathbf{u}\| r}. && \text{(3.6c)}
\end{aligned}$$

Therefore,

$$\kappa = \frac{24}{\mathrm{Re}}, \tag{3.7}$$

where Re is shown in Equation 3.4. In the next section, we use a correction of Stokes' drag to calculate the drag coefficient for our model.

3.1.4 Drag Coefficient: κ

The drag coefficient has a large influence on the motion of a droplet. The drag coefficient of an object moving through a fluid will vary depending on the speed of the object, the size of the object, and the density and viscosity of the fluid that the object is moving through. These properties are all handled within the Reynolds number (see Equation 3.4). In our model, we use a drag coefficient based on the work of Liu *et. al.* [15], in which the following assertion appears:

> At high relative velocities, the liquid drop deforms as it breaks up, and its drag coefficient should be a function of its Reynolds number and its oscillation amplitude.

We could impose a periodic time dependence on the radius of the droplet to account for the droplet's internal oscillations, *i.e.*, $r = r_0 \cos \omega t$ for some positive parameters r_0 and ω. For simplicity, we neglect these oscillations (discussed in Section 5.2.4). Therefore, the drag coefficient is calculated as [2, 15, 21]

$$\kappa\left(\|\mathbf{u}\|, r\right) = \begin{cases} \frac{24}{\mathrm{Re}}\left(1 + \frac{1}{6}\mathrm{Re}^{\frac{2}{3}}\right), & \text{if } \mathrm{Re} \leq 1000 \\ 0.424, & \text{if } \mathrm{Re} > 1000. \end{cases} \tag{3.8}$$

For Reynolds numbers lower than 1000 (but still larger than 1), a correction to Stokes' drag, $1 + \frac{1}{6}\mathrm{Re}^{\frac{2}{3}}$, was proposed by Putnam in [24]. For a Reynolds numbers higher than 1000 the drag coefficient of a rigid sphere, of radius r, is used. The model presented by Buck *et. al.* [5] also assumes that the droplets remain spherical as they travel through the air [22] and that the oscillations at the beginning of flight can be neglected [25]. A result of this assumption is that the radius of the droplet is assumed to be constant during its entire flight.

As mentioned in Section 3.1.2, we calculate the Reynolds number at every time step. Since we use the Reynolds number in the calculation of the drag coefficient (see Equation 3.8), we also calculate the drag coefficient at every time step. Even though the radius of the droplet is assumed to be constant during the flight of the droplet, the velocity of the droplet is changing during its flight which causes the drag coefficient to also change every time step of the blood droplet's flight. Figure 3.3 plots the drag coefficient against the Reynolds number using Equation 3.8 which is continuous. The drag coefficient decreases as the Reynolds number increases up to Re = 1000 where it plateaus. Figure 3.4 plots the drag coefficient against the norm of the velocity using Equation 3.8. The drag coefficient is a monotone decreasing function of speed. Also, smaller droplets experience a lower drag force but have a larger drag coefficient in accordance Equation 3.8.

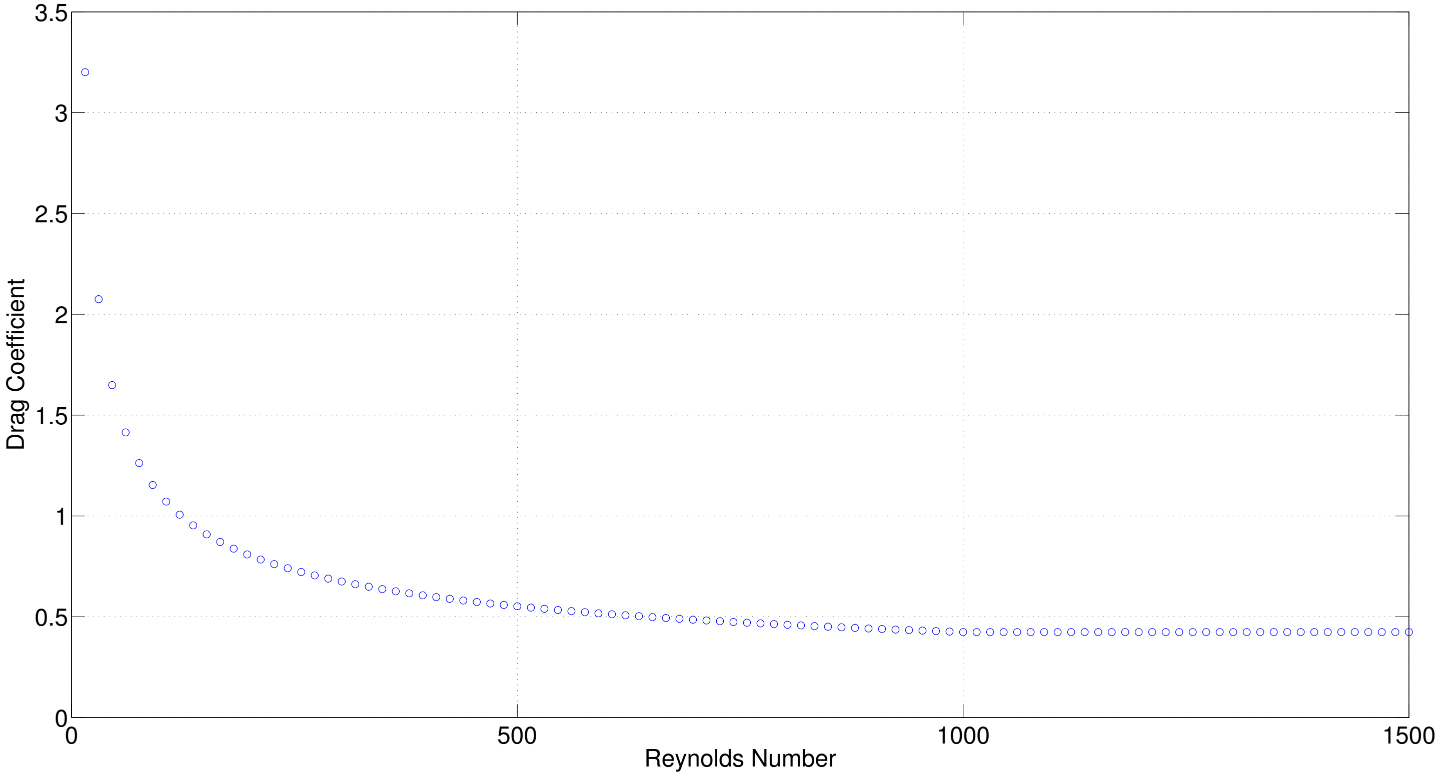

Figure 3.3: A plot of the calculation of the drag coefficient using a range of Reynolds numbers in Equation 3.8.

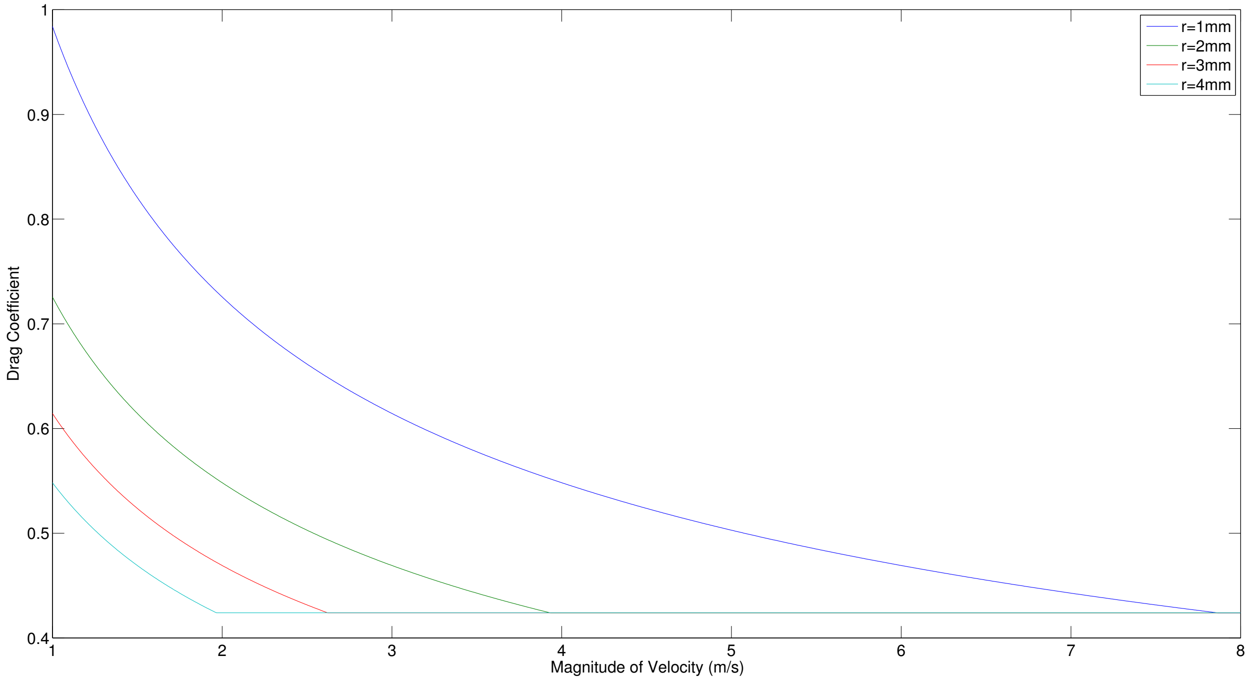

Figure 3.4: Drag coefficients calculated (via Equation 3.8) using four different radii and over the range $1\,\mathrm{ms}^{-1} \leq \|\mathbf{u}\| \leq 10\,\mathrm{ms}^{-1}$. This plot was made using the density and dynamic viscosity of porcine blood.

3.2 Dynamic ODE Model of Droplet Flight

Before describing the model here's a list of the assumptions we are making:

- Blood droplets can be treated as spheres;
- these spheres are rigid, *i.e.*, the radius of the droplet does not oscillate during the flight;
- the decision parameters are bounded above and below, *i.e.*, the radius of the droplet, the direction angles, and the initial speed of the droplet all lie within fixed intervals; and
- the drag force is quadratic in speed and the drag coefficient corresponding to this

drag force is given in Equation 3.8.

The model we present incorporates the force of gravity and effects of drag and is derived from Newton's Second Law of Motion. During a droplet's flight, the force of gravity acts downwards, *i.e.*, towards the centre of the Earth, and the drag force acts in the direction opposing the direction of motion (see Figure 3.5). The direction of the acceleration due to gravity is

$$\mathbf{g} = -g\mathbf{e}_2, \tag{3.9}$$

explicitly, where $\mathbf{e}_2$ is shown in Figure 3.1.

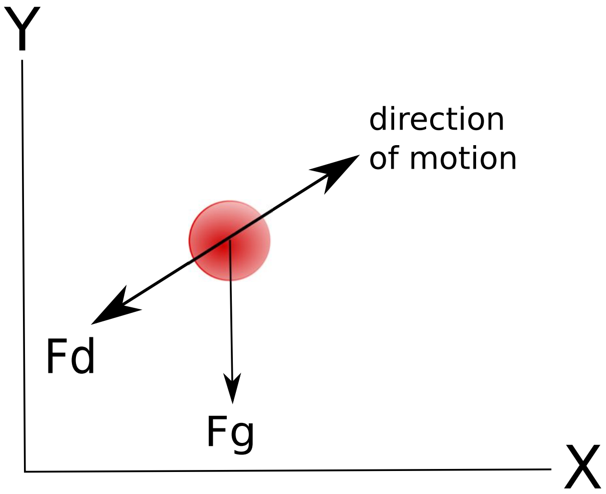

Figure 3.5: The forces acting upon a single droplet as it flies through the air. The drag force (Fd) with oppose the direction of motion and the force of gravity (Fg) acts only in the y direction, pulling the droplet downward.

We start this model with Newton's Second Law of Motion, $\mathbf{F} = m\dot{\mathbf{u}}$, where m is the mass of the droplet and $\dot{\mathbf{u}}$ is the acceleration of the droplet. The velocity of the droplet can also be written in terms of the position of the droplet, $\mathbf{x}$, where $\mathbf{u} = \dot{\mathbf{x}}$, thus $\dot{\mathbf{u}} = \ddot{\mathbf{x}}$. Also, the unit vector of the velocity is written as $\hat{\mathbf{u}}$ and the magnitude of the velocity is written as $\|\mathbf{u}\|$. The net force on a single droplet is

$$\mathbf{F} = \mathbf{F}_d + \mathbf{F}_g, \tag{3.10}$$

where $\mathbf{F}_d$ denotes the drag force acting on the droplet and $\mathbf{F}_g$ denotes the force of gravity. Substituting the drag force (also used by Liu *et. al.* in [15])

$$\mathbf{F}_d = -\frac{1}{2}\kappa\rho_{\text{air}}A\|\mathbf{u}\|^2\hat{\mathbf{u}}, \tag{3.11}$$

and the gravitational force

$$\mathbf{F}_g = -m\mathbf{g} \tag{3.12}$$

into Equation 3.10, we obtain

$$m\dot{\mathbf{u}} = -\frac{1}{2}\kappa\rho_{\text{air}}A\|\mathbf{u}\|^2\hat{\mathbf{u}} - m\mathbf{g}. \tag{3.13}$$

Notice, in Equation 3.13, A denotes the cross-sectional area of a sphere, not the surface area. We divide both sides of Equation 3.13 by m to get an expression for the acceleration, *i.e.*,

$$\dot{\mathbf{u}} = -\frac{\kappa\rho_{\text{air}}A}{2m}\|\mathbf{u}\|^2\hat{\mathbf{u}} - \mathbf{g}. \tag{3.14}$$

As $m = \rho_{\text{drop}}V$, where V is the volume of the blood droplet, Equation 3.14 can be simplified. The radius of the droplet is written as r and density of the droplet, ρ_{drop}, will change depending on the blood used in the laboratory experiment. If the experiment is with porcine blood the density is taken to be 1062 kgm^{-3}, for transfer blood the density was measured to be 1153 kgm^{-3}. It follows that

$$\dot{\mathbf{u}} = -\frac{\kappa\rho_{\text{air}}A}{2\rho_{\text{drop}}V}\|\mathbf{u}\|^2\hat{\mathbf{u}} - \mathbf{g} \tag{3.15a}$$

$$\dot{\mathbf{u}} = -\frac{\kappa\rho_{\text{air}}(\pi r^2)}{2\rho_{\text{drop}}(\frac{4}{3}\pi r^3)}\|\mathbf{u}\|^2\hat{\mathbf{u}} - \mathbf{g} \tag{3.15b}$$

and finally,

$$\dot{\mathbf{u}} = -\frac{3}{8}\frac{\kappa}{r}\frac{\rho_{\text{air}}}{\rho_{\text{drop}}}\|\mathbf{u}\|^2\hat{\mathbf{u}} - \mathbf{g}. \tag{3.16}$$

Expanding Equation 3.17, we get the first order ODE model

$$\dot{x} = u_x \tag{3.17a}$$

$$\dot{y} = u_y \tag{3.17b}$$

$$\dot{z} = u_z \tag{3.17c}$$

$$\dot{u}_x = -\frac{3}{8}\frac{\kappa\left(\|\mathbf{u}\|, r\right)}{r}\frac{\rho_{\text{air}}}{\rho_{\text{drop}}}u_x\left(\sqrt{u_x^2 + u_y^2 + u_z^2}\right) \tag{3.17d}$$

$$\dot{u}_y = -\frac{3}{8}\frac{\kappa\left(\|\mathbf{u}\|, r\right)}{r}\frac{\rho_{\text{air}}}{\rho_{\text{drop}}}u_y\left(\sqrt{u_x^2 + u_y^2 + u_z^2}\right) - g \tag{3.17e}$$

$$\dot{u}_z = -\frac{3}{8}\frac{\kappa\left(\|\mathbf{u}\|, r\right)}{r}\frac{\rho_{\text{air}}}{\rho_{\text{drop}}}u_z\left(\sqrt{u_x^2 + u_y^2 + u_z^2}\right) \tag{3.17f}$$

which is the form used by an Initial Value Problem (IVP) solver.

To solve Equation 3.17, six initial conditions are needed: three initial spatial coordinates and three initial velocity components. For convenience, the initial components of velocity are specified using spherical rather than rectangular coordinates. That is, if u_{x_0}, u_{y_0}, and u_{z_0} denote the rectangular components of the initial velocity $\mathbf{u}_0$, then

$$u_{x_0} = u_0 \cos\theta_0 \cos\phi_0, \tag{3.18a}$$

$$u_{y_0} = u_0 \sin\theta_0, \text{ and} \tag{3.18b}$$

$$u_{z_0} = u_0 \cos\theta_0 \sin\phi_0. \tag{3.18c}$$

In (3.18), ϕ_0 is the initial azimuthal angle, θ_0 is the initial altitude angle, and u_0 is the initial speed of the droplet (see Figure 3.1 coordinate system).

3.3 Fitting the Dynamic ODE Model to the Laboratory Experiment Data

We are fitting our dynamic ODE model described in Section 3.2 to reconstructed trajectories from the laboratory experiments (see Chapter 2) to verify our model. A reconstructed trajectory is obtained by tracking an individual blood droplet in a video of a laboratory experiment. We describe the reconstruction process in Section 3.3.1. We also describe the process of fitting our ODE model to a reconstructed trajectory in Section 3.3.2. We obtain the fitting by solving an optimisation problem where the objective function measures the Euclidean distance between a dynamic ODE-based trajectory and a trajectory reconstructed from a video of a laboratory experiment. This optimisation is done by fine tuning the decision variables, within imposed bounds, in the ODE-based trajectory until it is a reasonable fit to the experimental path reconstruction.

A given path is $W = \{\mathbf{w}_0, \mathbf{w}_1, \mathbf{w}_2, ..., \mathbf{w}_k\}$, where $\mathbf{w}_t = (x_t, y_t, z_t, t)$. The reconstructed trajectories are translated so that the initial spatial coordinates are $(x_0, y_0, z_0) = (0, 0, 0)$ at $t = t_0 = 0$ so that $\mathbf{w}_0 = (0, 0, 0, 0)$. Let $\mathbf{v}(t; r, u_0, \theta_0, \phi_0) = \{\mathbf{v}_0, \mathbf{v}_1, \mathbf{v}_2, ..., \mathbf{v}_k\}$ be the numerical solution of the IVP with initial conditions specified by $(0, 0, 0, u_0, \theta_0, \phi_0)$ and parameter r. Therefore, the objective function, f, is written as

$$f(r, u_0, \theta_0, \phi_0) = \sum_{t=0}^{k} \left\| \mathbf{v}_t - \mathbf{w}_t \right\|^2 . \tag{3.19}$$

3.3.1 Reconstruction of Experimental Blood Droplet Trajectories

We employ the software of Zarrabeitia *et. al.* [30] to extract the paths of individual blood droplets from videos of the laboratory experiments. We refer to this software as the Droplet Tracker (DT). It is an automated method for identifying a unique blood droplet in the videos from a stereo pair of cameras and tracking its trajectory using the video data. Figure 3.6 shows the mock crime scene with trajectories as reconstructed by DT overlaid as recorded from each camera.

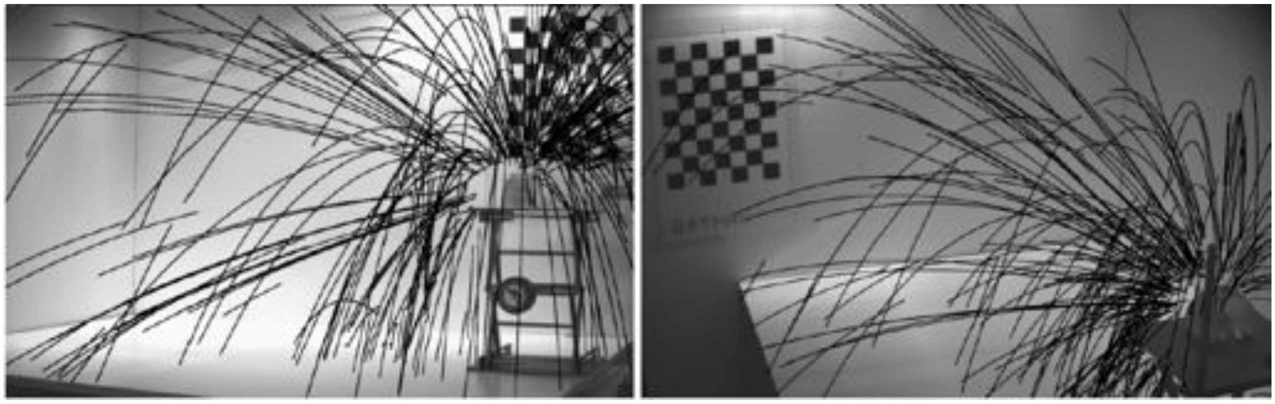

Figure 3.6: Automated tracking of a full experiment using the Droplet Tracker [30].

Given two pixels p_{I} and p_{II} in two synchronised video frames captured by each camera, the software DT generates putative spatial coordinates (x, y, z) of a point in a trajectory. Each of the pixels p_{I} and p_{II} backprojects to a line in three-dimensional space, ℓ_{I} and ℓ_{II}, respectively. The spatial coordinates (x, y, z) computed by the software DT, then, are the coordinates of the midpoint of the shortest line segment connecting ℓ_{I} and ℓ_{II}. The estimated misfit e associated with (x, y, z) is half the length of that same shortest line segment (see [30] for details).

Each numerical trajectory produced by DT is stored as a matrix of form

$$M = \begin{bmatrix} \mathbf{t} & \mathbf{x} & \mathbf{y} & \mathbf{z} & \mathbf{e} \end{bmatrix} = \begin{bmatrix} t_0 & x_0 & y_0 & z_0 & e_0 \\ t_1 & x_1 & y_1 & z_1 & e_1 \\ t_2 & x_2 & y_2 & z_2 & e_2 \\ \vdots & \vdots & \vdots & \vdots & \vdots \\ t_N & x_N & y_N & z_N & e_N \end{bmatrix}. \tag{3.20}$$

In Equation 3.20, the columns $\mathbf{t}$, $\mathbf{x}$, $\mathbf{y}$, $\mathbf{z}$, and $\mathbf{e}$ of M denote time, x-coordinates, y-coordinates, z-coordinates, and estimated misfits associated with each droplet, respectively, and N is the number of frames in which this droplet's motion was successfully captured by both cameras. The $(N+1)$-vector of times $\mathbf{t}$ associated with a path consists of frame indices and is not necessarily contiguous. In practice, individual droplets may not be tracked in every frame for a number of possible reasons:

- droplets in the video leave the field of view;
- droplets in the video return to the field of view;
- droplets collide with one another;
- noise obscures detection of a droplet in some frames;
- droplets break up into smaller droplets; and
- droplets occlude one another in the view of either camera

The software DT records the rows of M in (3.20) with the frame indices in $\mathbf{t}$ translated to start at $t_0 = 0$. DT also provides a rotation matrix in the form

$$R = \begin{bmatrix} \cos\phi & 0 & -\sin\phi \\ 0 & 1 & 0 \\ \sin\phi & 0 & \cos\phi \end{bmatrix}. \tag{3.21}$$

While in this optimisation problem we choose to use the three-dimensional data over the two-dimensional data, DT provides a rotation matrix R (see Equation 3.21) to rotate all the trajectories onto the $\phi = 0$ plane (see Figure 3.7). It is acceptable to perform this optimisation with two-dimensional data because both gravity and drag are isotropic forces meaning regardless of the value for ϕ, gravity will always pull the droplet downward. Similarly, the drag force will always oppose the motion of the droplet regardless of its direction of motion. The initial guess for the parameter ϕ is extracted from R.

(a) This is the original axis setup with two independent paths shown. Each trajectory is expressed in terms of this coordinate system.

(b) Find the principal direction of motion and set the x axis to that direction. Each trajectory has its own coordinate system.

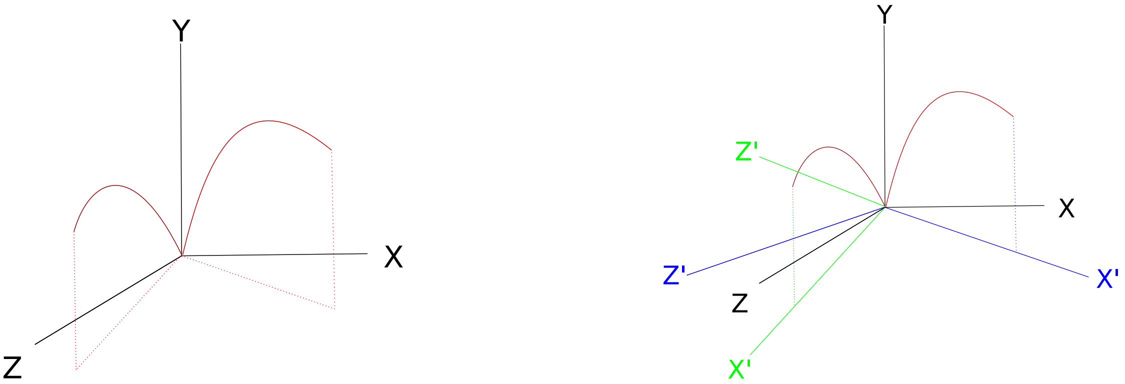

(c) Rotate all new principal directions or new x axes to one plane according to their respective values of ϕ. Note all trajectories still share the same y axis.

(d) Now all the trajectories lie approximately flat on one plane and the measurements in the z direction are deviations from the x plane during the rotation.

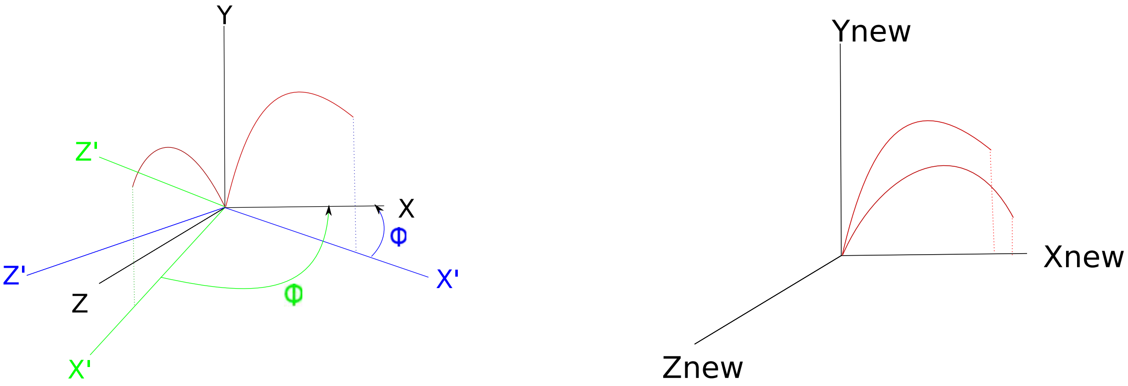

Figure 3.7: Depiction of the coordinate system change when converting three-dimensional to two-dimensional or planar data.

However, there will be some deviation in z plane when performing the rotation and so the initialisation for ϕ will not be exact and will still need to be a decision variable in the fitting.

3.3.2 Using a Practical Optimisation Solver

We use an optimisation tool based on the Nelder-Mead simplex algorithm to optimise the norm between the ODE-based trajectory and the reconstructed path from DT. The

Nelder-Mead simplex algorithm, or the downhill simplex method, is a nonlinear optimisation technique. In our case, the method is approximating a local minimum problem, with four variables. Nelder-Mead is capable of N variables but a reasonable limit for N is five variables. Nelder-Mead also works well with problems that vary smoothly and have one mode or solution. Our model is low dimensional which makes it appropriate to use this algorithm for the optimisation of the objective function. The four decision variables of this optimisation problem are the radius, the initial speed, and the direction angles of the initial velocity vector (θ and ϕ). The optimisation solver will optimise all four variables at once, rather than one at a time and this process is repeated until the optimisation norm is satisfactory.

3.3.3 Initialisation of Decision Parameters for Optimisation

Each reconstructed trajectory from DT is fitted with a curve produced by the integration of Equation 3.17 with optimised parameters which are specific to each individual path. The initial conditions of the model are described in Equation 3.18 where each reconstructed trajectory from DT has been translated to start from the origin of the coordinate system which is the centre of the ballistics gel target. The initial speed of the droplet, u_0, is calculated using the norm of the finite differences over the first two points of the reconstructed path from DT. Thus,

$$u_{x_0} = \frac{x_2 - x_1}{\Delta t} \tag{3.22a}$$

$$u_{y_0} = \frac{y_2 - y_1}{\Delta t} \tag{3.22b}$$

$$u_{z_0} = \frac{z_2 - z_1}{\Delta t} \tag{3.22c}$$

and

$$u_0 = \left(\sqrt{u_{x_0}^2 + u_{y_0}^2 + u_{z_0}^2} \right) \tag{3.23}$$

where Δt is the time difference between the first two frames the droplet has been tracked in by DT and u_{x_0}, u_{y_0}, and u_{z_0} are the spatial components of u_0. The initial guess of r is 2.5 millimetres and the initial guess for ϕ can be extracted from the rotation matrix R as mentioned in Section 3.3.1. The initial guess of the decision variable θ is dependent on the first few points of the reconstructed path form DT. We explain the initial guess of θ in Section 3.3.4.

To prevent the optimisation solver from returning unphysical values for the drag coefficient, radius, exit angles and initial speed, we impose bounds on the decision variables:

- radius of a single droplet: $1\,\text{mm} \leq r \leq 4\,\text{mm}$;
- initial velocity of a droplet: $1\,\text{ms}^{-1} \leq u_0 \leq 10\,\text{ms}^{-1}$; and
- angles of exit from the target: $0 \leq \phi \leq 2\pi$

3.3.4 Initialisation of the parameter θ

Originally, the bounds on θ were set to $0 \leq \theta \leq 2\pi$ in order to allow the fitting of a droplet travelling in any direction. There are instances where an ODE-based path with reasonable values of r and u_0 has a low norm but the actual plots of the ODE-based path and the DT reconstructed path are not visibly the same. The problem is shown in Figure 3.8 where the the calculated parameters are: $r = 0.001$, $u_0 = 2.33$, $\theta = 6.28$, $\phi = 1.19$ and the optimisation norm is 0.29. We can clearly see that the ODE-based path does not fit well with the DT experimental path reconstruction.

To ensure the reconstructed value of θ is reasonable, we adopt the following procedure. If the y coordinates of the first few points of the experimental path reconstruction are all positive, then we restrict θ to the range $0 \leq \theta \leq \pi$. If the y coordinates of the first few

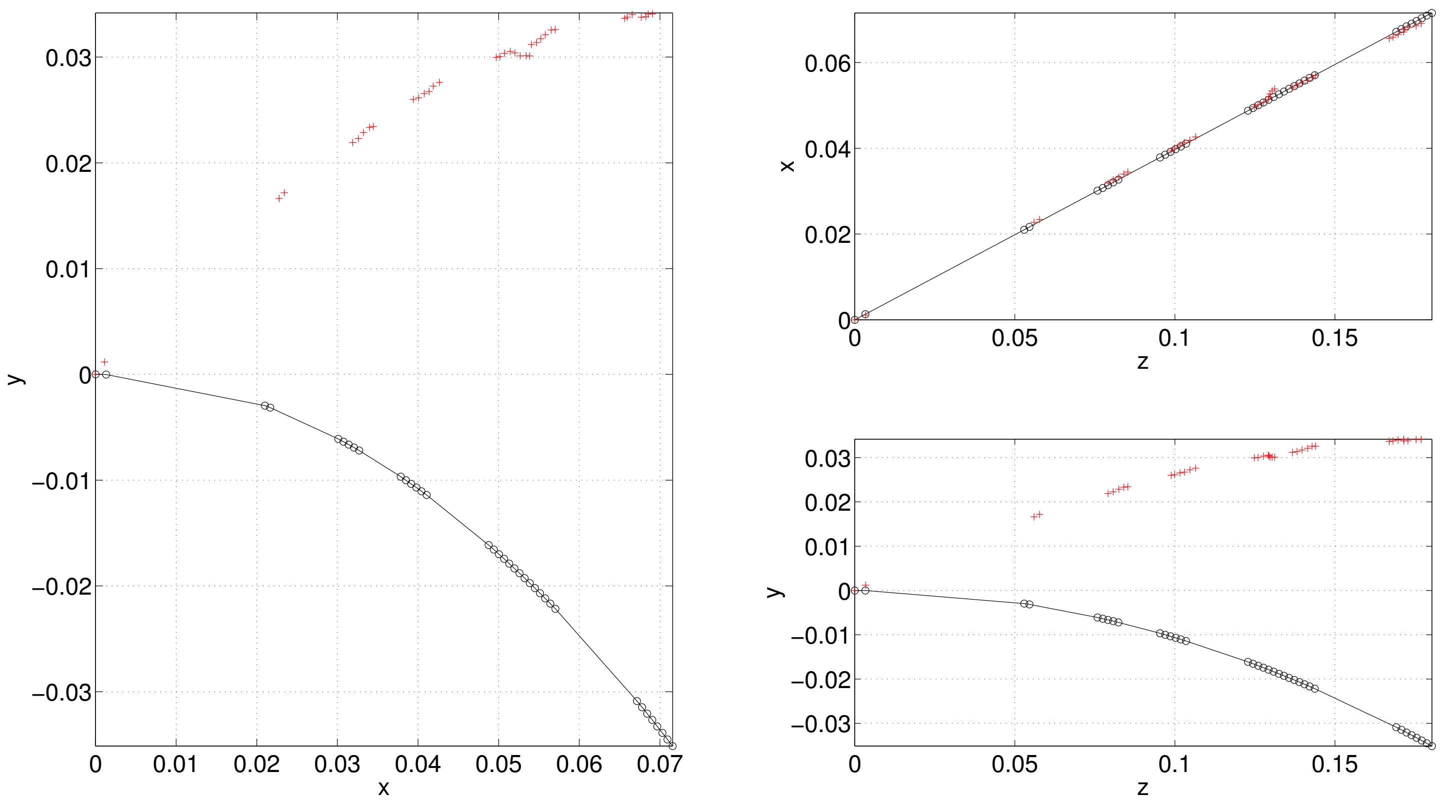

Figure 3.8: The reconstructed path of a single synthetic blood droplet from DT (in red) and the ODE-based path (in black). The optimisation solver fails to solve the fitting problem properly because of the bounds on the variable θ.

points of the experimental path reconstruction are all negative, then we restrict θ to the range $\pi \leq \theta \leq 2\pi$. In Figure 3.9, the problem is resolved and the calculated parameters are: $r = 0.001$, $u_0 = 2.47$, $\theta = 0.34$, $\phi = 1.19$ and a lower optimisation norm of 0.018.

3.3.5 Criteria for Rejection of Reconstructed Trajectories

Given that the data we are attempting to fit with an ODE-based trajectory is generated by the tracking software DT, the reconstructed trajectory produced may not be physically

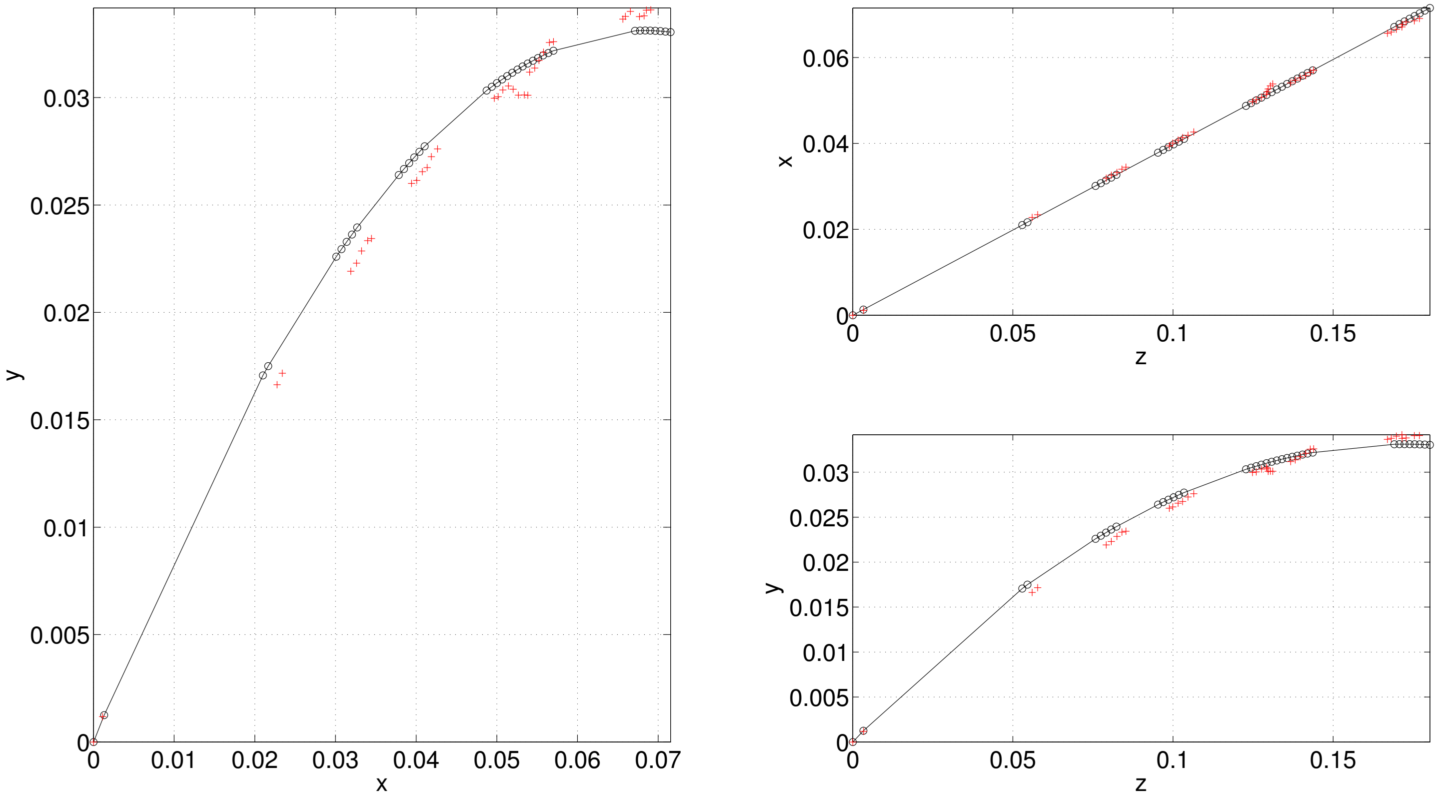

Figure 3.9: The reconstructed path of a single synthetic blood droplet from DT (in red) and the optimisation solver successfully the fits an ODE-based trajectory (in black) to the reconstruction.

reasonable, we need some criteria to decide whether or not to reject a reconstruction. In order for a path reconstruction to be considered for fitting or to remain in the final data set it must pass these criteria:

1. The path reconstruction from DT must have more than 15 frames tracked, *i.e.* the reconstruction must have at least 15 points in the trajectory;
2. The average estimated misfit for a path reconstruction must be less than 0.02 centimetres;
3. The final norm after fitting the ODE-based trajectory to the DT path reconstruc-

tion must be less than 1 centimetre; and

4. During the fitting, the optimisation solver must not get stuck at the boundary of any given parameter.

When the optimisation solver is choosing parameters to perform the fitting, sometimes the solver will choose a value of a parameter that is too close to the boundary. Once the solver is at a boundary and attempts to choose a value off the boundary it will not take a step large enough away from the boundary and thus get caught at the boundary. We call this issue clamping. Refer to [12] for a study on some convergence properties of the Nelder-Mead simplex method.

Chapter 4

Experimental Results

We collect the stereo video data of 80 transfer blood experiments and 2 porcine blood experiments using the procedure from Chapter 2. In Sections 4.1 and 4.2 the ODE-based trajectories are depicted by black lines and the path reconstructions provided by DT are depicted by red data points. For brevity, we refer to the experimental path reconstructions from DT as DT trajectories.

We expect that minimisation of the Euclidean distance, *i.e.*, the objective function (see Section 3.3) will be small enough that the ODE-based trajectory will visually fit the spatial coordinates of the DT trajectory (see Sections 4.1 and 4.2). The process of fitting the ODE-based trajectory to the DT trajectory will yield an optimisation norm which we expect to be less than 1 centimetre. We also expect the estimated misfit (see Section 3.3.1) associated with the tracking of the blood droplets to be less than 0.2 millimetres.

In order to validate our model we use a finite difference method to find the velocity of a given droplet at every time step in its DT trajectory. We also extract the velocities of the droplet from the corresponding ODE-based trajectory. We expect that these methods of calculating the speed of the droplet at each time step should yield similar results and thus validate our model.

4.1 Visual Verification of the Model on Single Trajectories

The DT trajectories that were chosen for visual verification of our model were path reconstructions with the most data points *i.e.*, droplets that DT tracked for the greatest number of frames. There is one droplet from a porcine blood experiment and two droplets from two separate transfer blood experiments.

Figure 4.1 shows a DT trajectory that has 446 plotted spatial coordinates. This porcine blood droplet is moving in the positive x-direction (meaning it is following the direction of the shot riot ball) and its reconstructed trajectory is visibly curved. There is some error in the fitting near the end of the DT trajectory, in the z-direction, however this can be attributed to the tracking of the droplet by DT as the DT trajectory has an unnatural curve, seen in the xz-plot. Overall we can see the ODE-based model fits the DT trajectory very well and the Euclidian norm between these two paths is 2.95 centimetres. The trajectories shown superficially resemble parabolas. However, over longer time scales, the influence of viscous drag forces will make the trajectories deviate further from parabolic curves.

Figure 4.2 shows a similar verification but using a DT trajectory from a transfer blood experiment where the droplet was tracked in 168 frames. This path reconstruction is noisier than the DT trajectory shown in Figure 4.1 but is also a forward moving droplet and its trajectory is visibly curved. We can see again that the ODE-based trajectory is not accurate in fitting the DT trajectory near the end of the path in the z-direction but this can be attributed to the noisy path reconstruction. However, we can see in general the ODE-based trajectory matches the DT trajectory well with an optimisation norm of 4.46 centimetres.

Figure 4.3 shows another DT trajectory selected from a different transfer blood experiment where the droplet is tracked in 266 frames. This transfer blood droplet is a backward

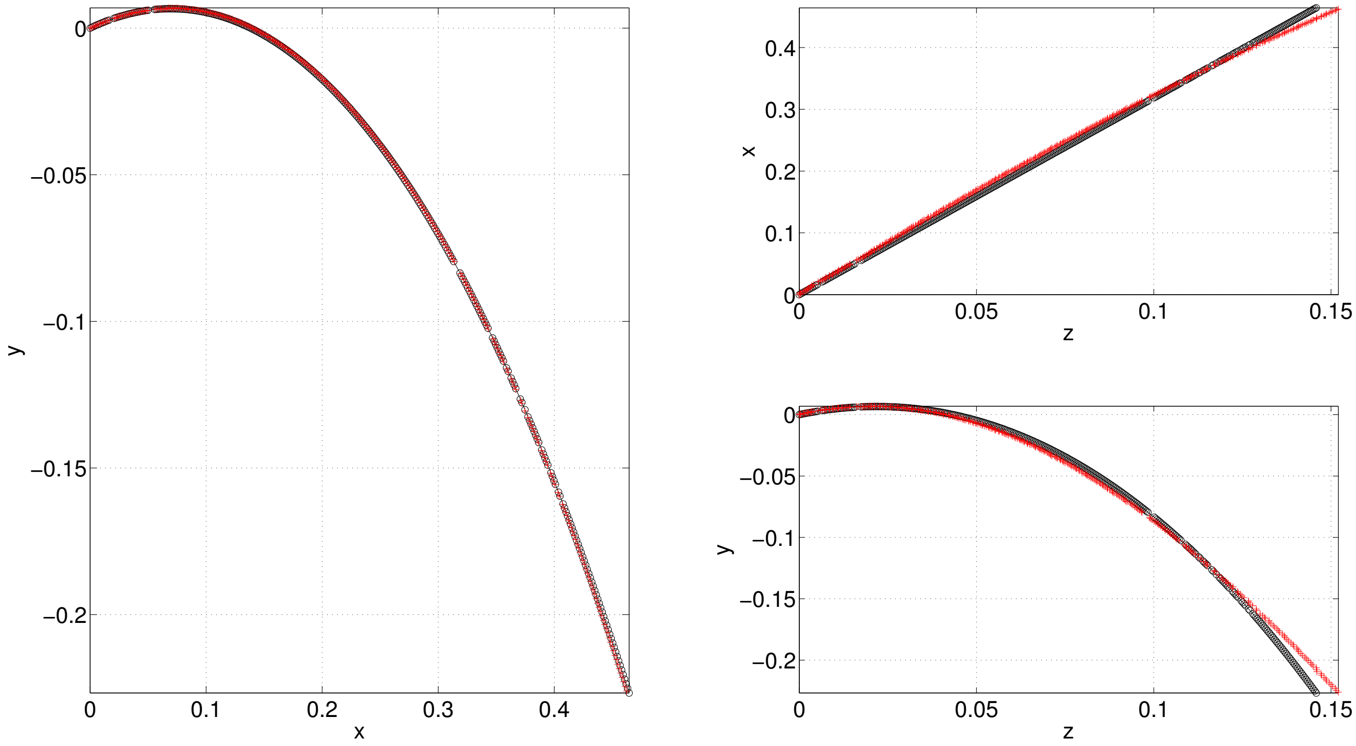

Figure 4.1: The red data points are the spatial coordinates of the porcine blood droplet tracked by DT, producing the experimental path reconstruction. The black line is the ODE-based trajectory with optimised parameters to reduce the Euclidean distance between the DT trajectory and the ODE-based trajectory.

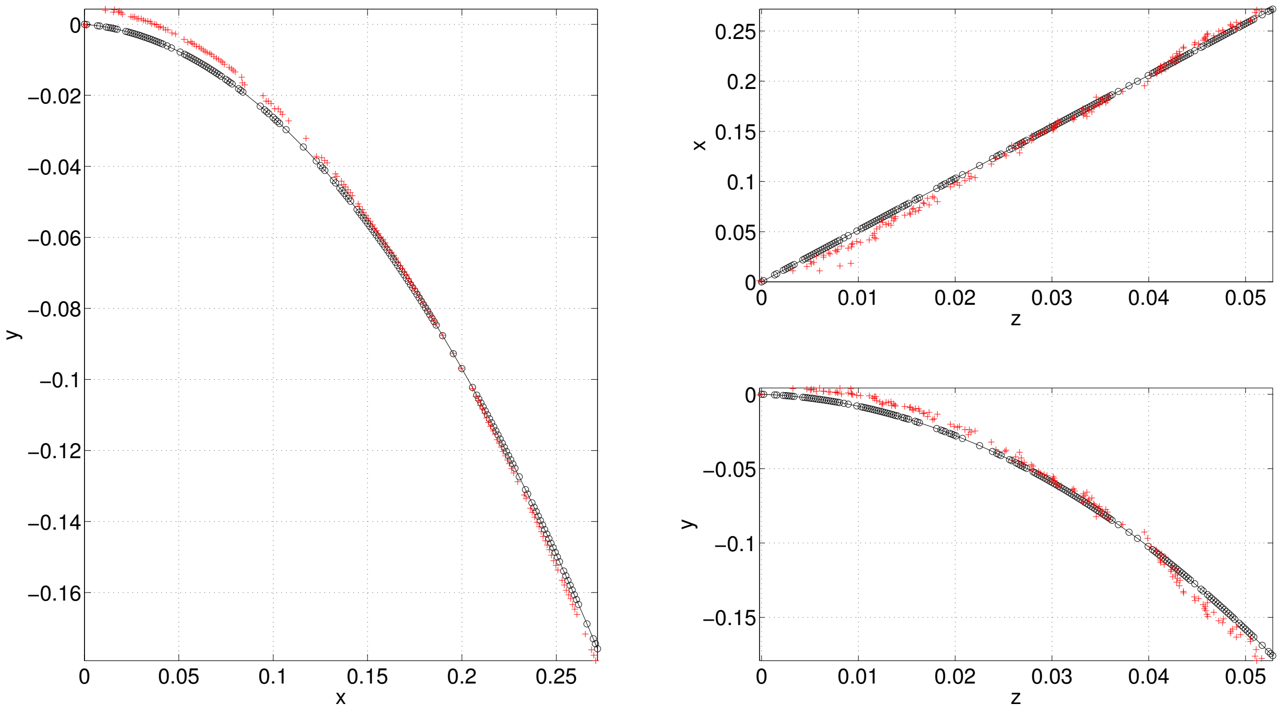

Figure 4.2: The red data points are the spatial coordinates of a transfer blood droplet tracked by DT. The black line is the ODE-based trajectory with optimised parameters to reduce the Euclidean norm between the DT trajectory and the ODE trajectory.

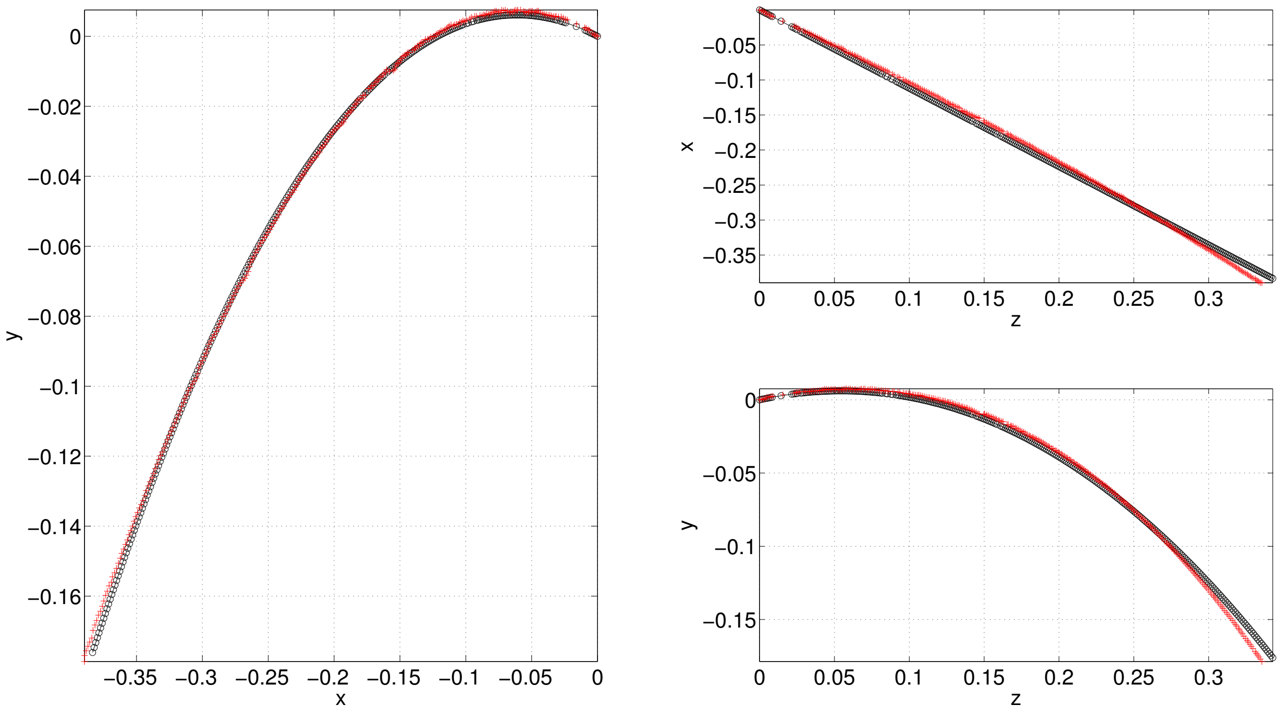

Figure 4.3: The red data points are the spatial coordinates of a transfer blood droplet (from a different transfer blood experiment) tracked by DT. The black line is the ODE-based trajectory with optimised parameters to reduce the Euclidean norm between the DT trajectory and the ODE trajectory.

moving droplet, meaning when the riot ball struck the ballistics gel, the blood droplet is travelling in the opposite direction of the riot ball. In this instance, we can see that the ODE-based trajectory is failing to fit the DT trajectory at the end of the path in the x-direction. However, in both Figures 4.2 and 4.3, the xz-plots of the DT trajectories reveal some motion of the vertical plane. As a result, our model that incorporates forces that are acting strictly within a vertical plane will not yield a good fit in regions where the out-of-plane deviations are largest. This fitting resulted in an optimisation norm of 1.93 centimetres and again we can see again that the ODE-based trajectory matches the DT trajectory very well.

4.2 Visual Verification of the Fitting for Full Experiments

For the individual trajectories in Figures 4.1, 4.2, and 4.3, we can visually confirm that the ODE-based model is fitting the DT trajectories with good accuracy. However, to ensure that the accurate fitting of individual ODE-based trajectories to DT trajectories (see Section 4.1) are not isolated occurrences, we plot all DT trajectories with their corresponding ODE-based trajectories in three different figures. The thick green line in Figures 4.4, 4.5 and 4.6 is the path of the riot ball. We can see in Figure 4.4 that for straight line or curved DT trajectories and forward moving or backward moving DT trajectories, the ODE-based model is fitting the experimental reconstruction very well.

Figure 4.5 is an overhead view, showing the zx-plane, of the porcine blood experiment. There are a few trajectories where we can see the ODE-based model is not fitting the DT trajectory properly (possibly because the reconstruction is noisy or the average estimated misfit is high) but for most of the reconstructed trajectories, the ODE-based trajectories are fitting the DT trajectories very well. Figure 4.6 shows a plot of the DT trajectories and their corresponding ODE-based trajectories from the perspective of being behind the paintball gun. Again, most trajectories are being fitted very well; however, there are two short, noisy trajectories just above the origin where the fitting is failing.

Figures 4.7, 4.8, and 4.9 are the DT trajectories from a transfer blood experiment and their corresponding ODE-based trajectories plotted together. In general, the ODE-based trajectories are fitting the DT trajectories very well however there are a few DT trajectories that are exhibiting out-of-plane motion or simply have a lot of noise. Specifically a single DT trajectory in Figure 4.8 curves sharply to the right. The ODE-based trajectories, expectedly, fail to fit those DT trajectories.

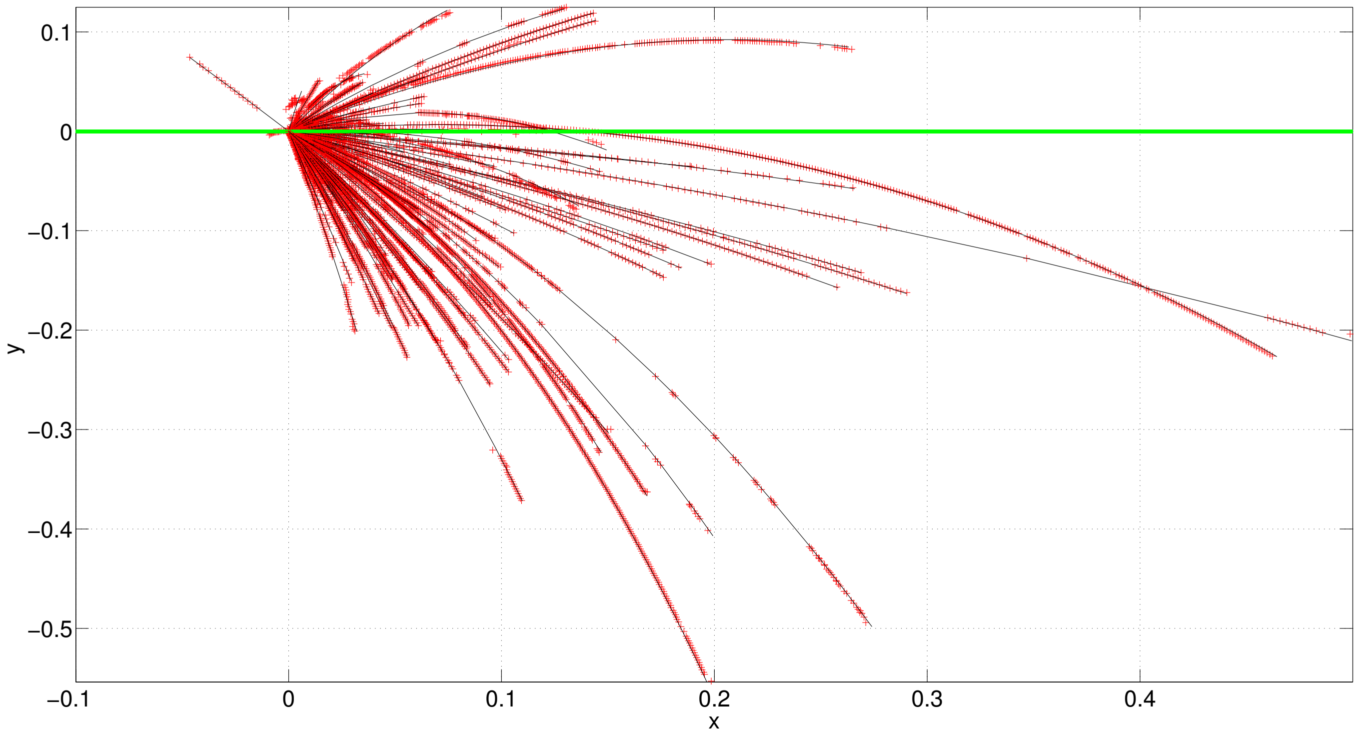

Figure 4.4: An xy view of the DT trajectories (red data points) and each of their ODE-based trajectories (black line). The riot ball is plotted in green, moving in the positive x direction.

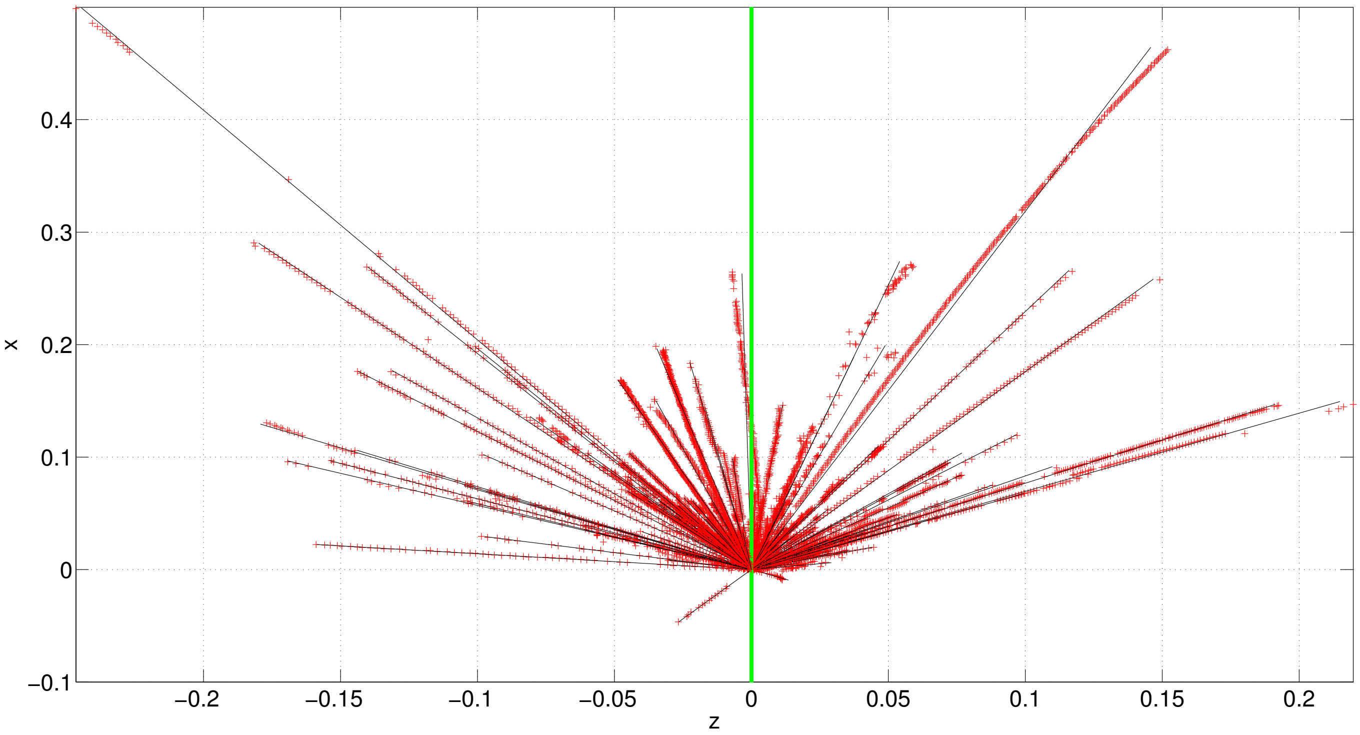

Figure 4.5: A zx view of the DT trajectories (red data points) and each of their ODE-based trajectories (black line). The riot ball is plotted in green, moving in the positive x direction.

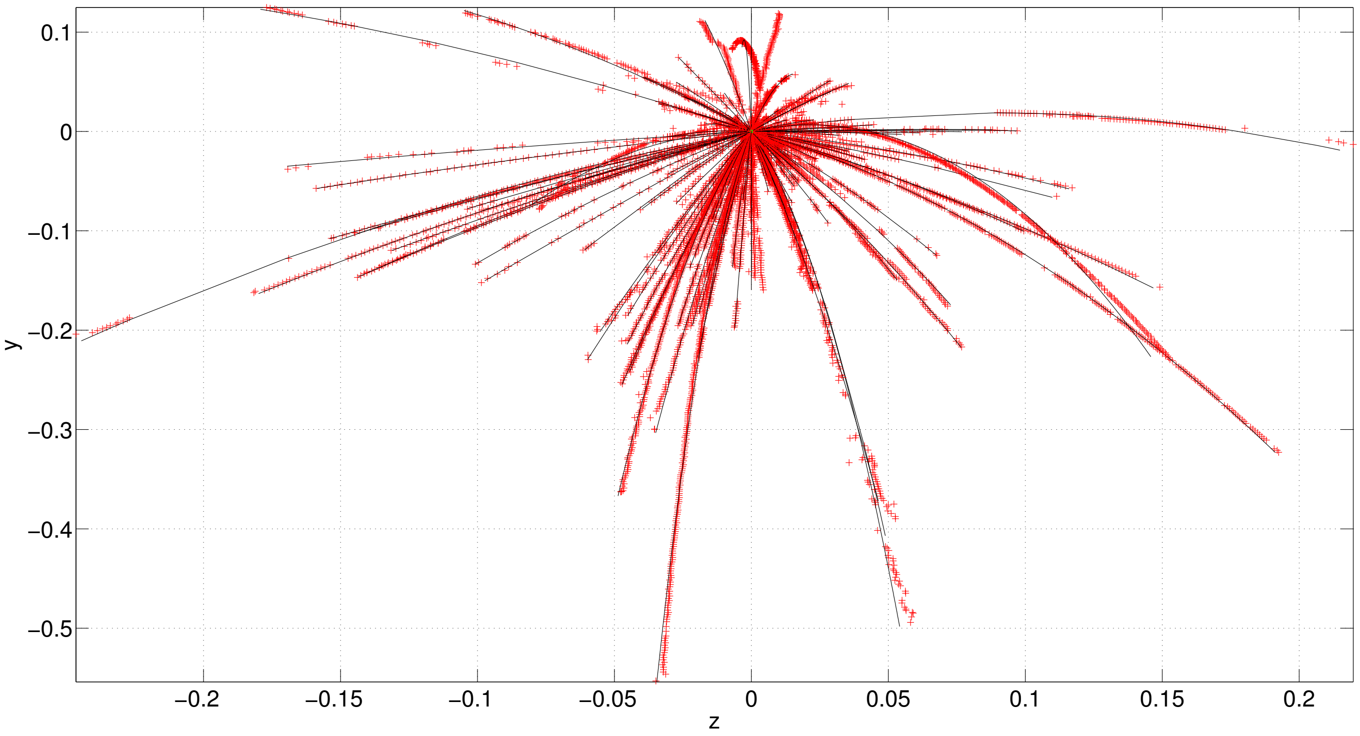

Figure 4.6: A zx view of the DT trajectories (red data points) and each of their ODE-based trajectories (black line).

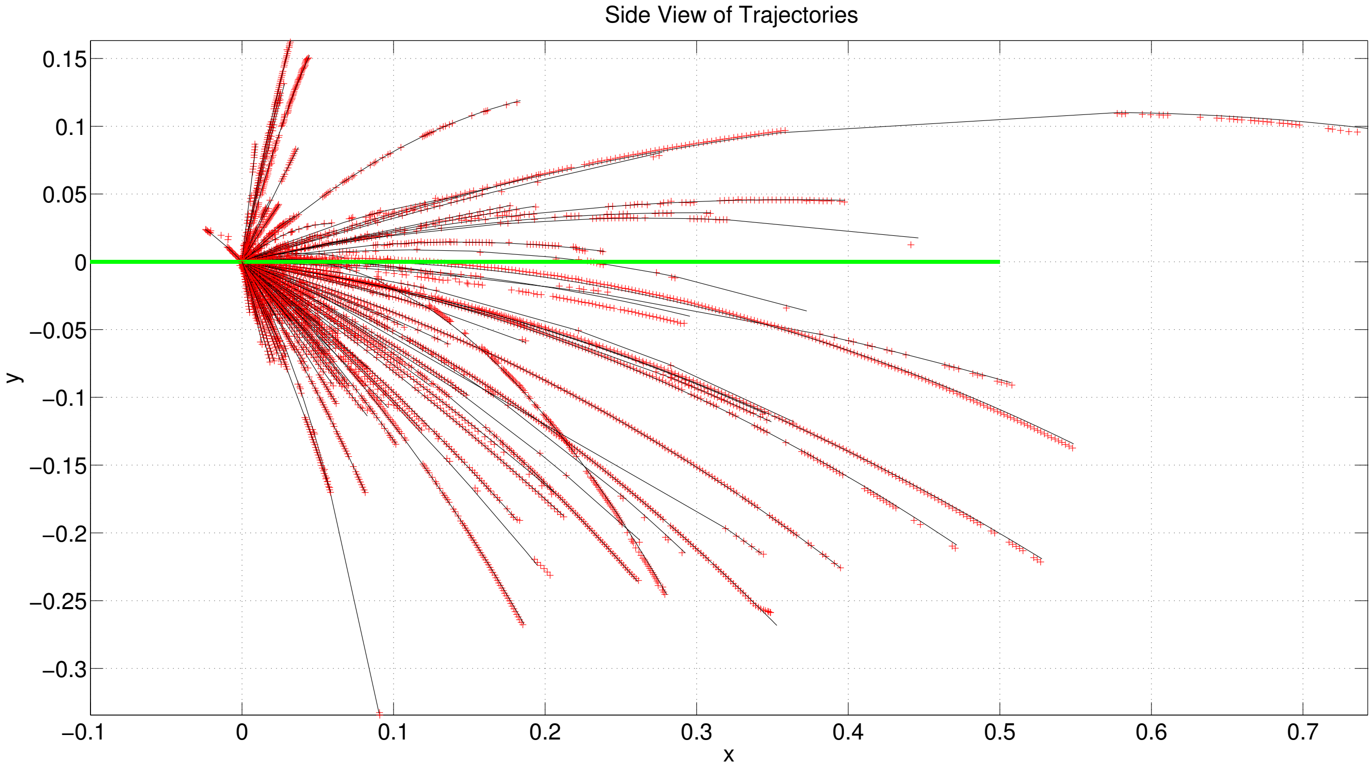

Figure 4.7: An xy view of the DT trajectories (red data points) and each of their ODE-based trajectories (black line). The riot ball is plotted in green, moving in the positive x direction.

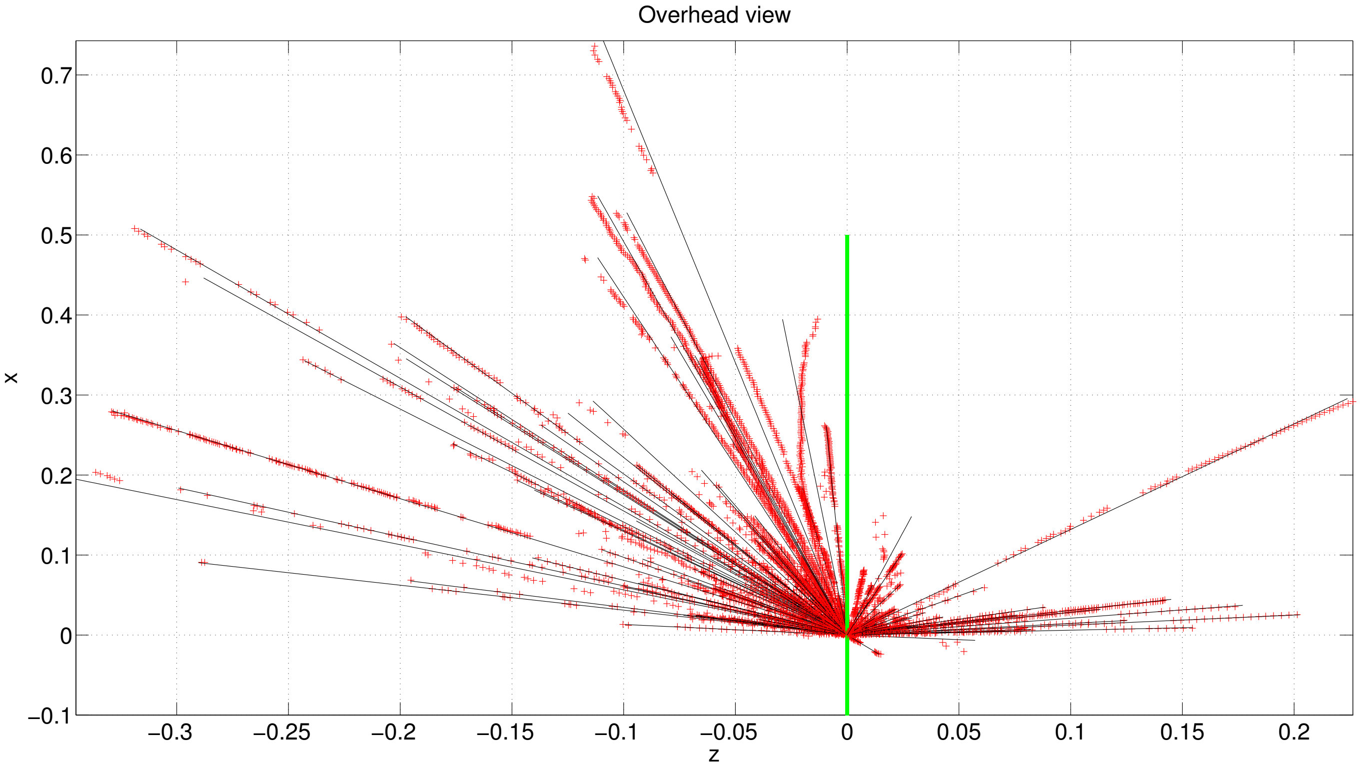

Figure 4.8: A zx view of the DT trajectories (red data points) and each of their ODE-based trajectories (black line). The riot ball is plotted in green, moving in the positive x direction.

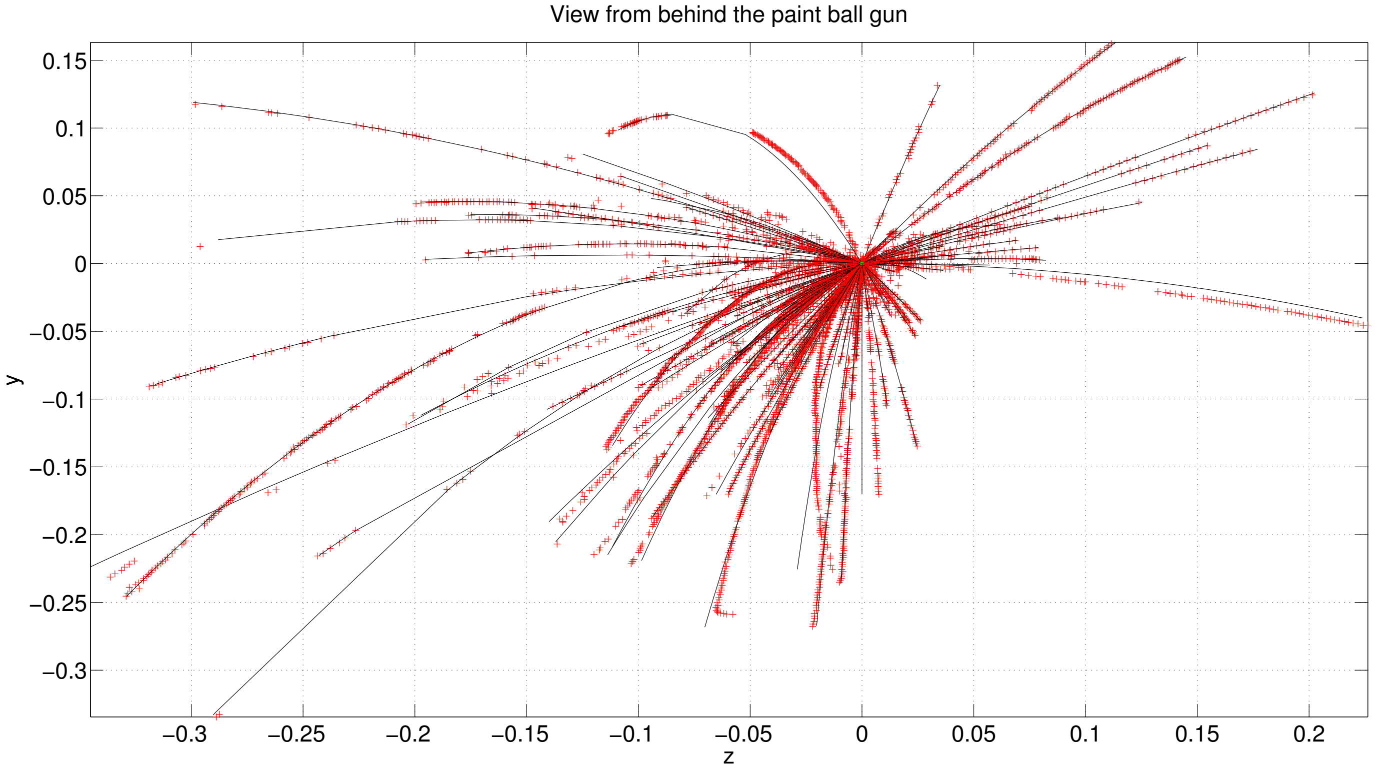

Figure 4.9: A zx view of the DT trajectories (red data points) and each of their ODE-based trajectories (black line).

4.3 Validation of the Model by Comparing Speeds for Individual Trajectories

In the objective function, the calculation of the Reynolds number and the drag coefficient is done for every time step along the DT trajectory. As mentioned in Chapter 3, the Reynolds number depends on the norm of the velocity components and the radius of the droplet. Since we cannot validate that our model is choosing the correct radius because of the low camera resolution (see Section 5.2.4), we validate the norm of the velocity instead. To do this we take the reconstructed experimental paths and at each time step, assuming linear motion between steps, calculate the speed using finite differences. We also extract the norm of the velocity at each time step from our ODE model and we expect that both speed plots will be very similar.

For a porcine blood droplet, Figure 4.10 shows that the speed at each time step of DT trajectory (the blue data points) follows the same characteristics as the speed plot for the ODE-based trajectory (the green line). Since these speed plots are very similar in shape, we can validate that the speeds calculated by the integration of the ODE are correct.

Figures 4.11 and 4.12 are speed validation plots for two different transfer blood droplets in two different experiments. Even with the noisy finite difference calculation seen in Figure 4.12 we can see a general decrease in speed as the droplet reaches the apex of its curved trajectory and then an increase in speed as the droplet falls toward the table. Again, this confirms that the speeds calculated by the ODE model are reasonable. Further, the optimisation norms of the data used in Figures 4.10, 4.11 and 4.12 are 2.95 centimetres, 4.46 centimetres and 1.93 centimetres, respectively.

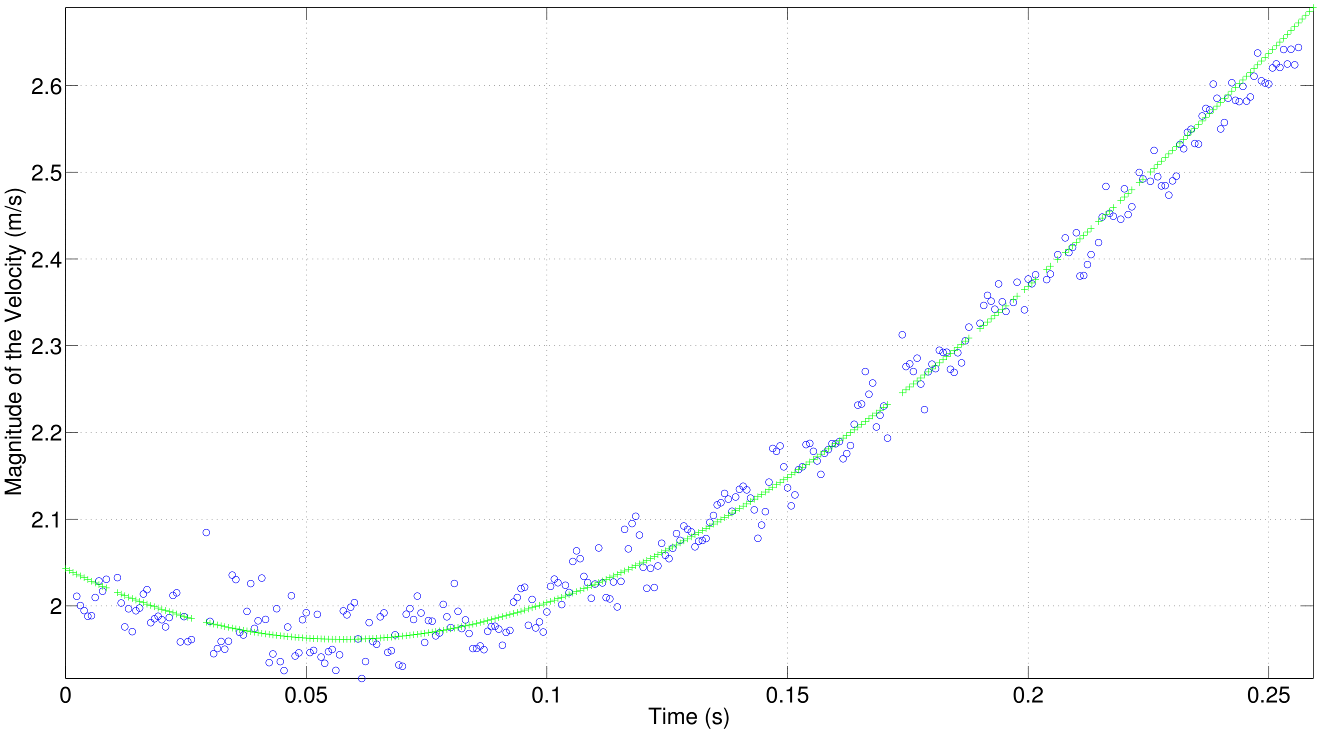

Figure 4.10: The blue data points are the speeds calculated at every time step of the DT reconstruction (using finite differences) and the green line is the speed calculated at every time step from the ODE-based trajectory. This is for one droplet in the porcine blood experiment. The optimisation norm is 2.95 centimetres.

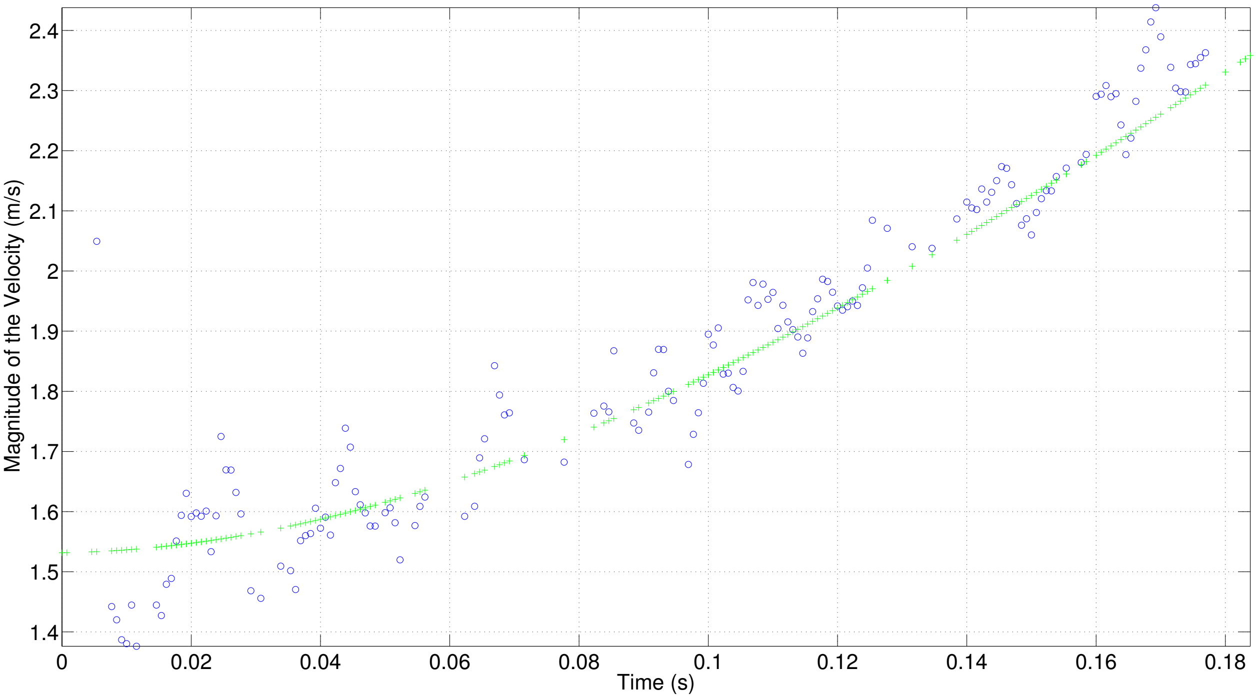

Figure 4.11: The blue data points are the speeds calculated at every time step of the DT reconstruction (using finite differences) and the green line is the speed calculated at every time step from the ODE-based trajectory. This is for one droplet in a transfer blood experiment. The optimisation norm is 4.46 centimetres.

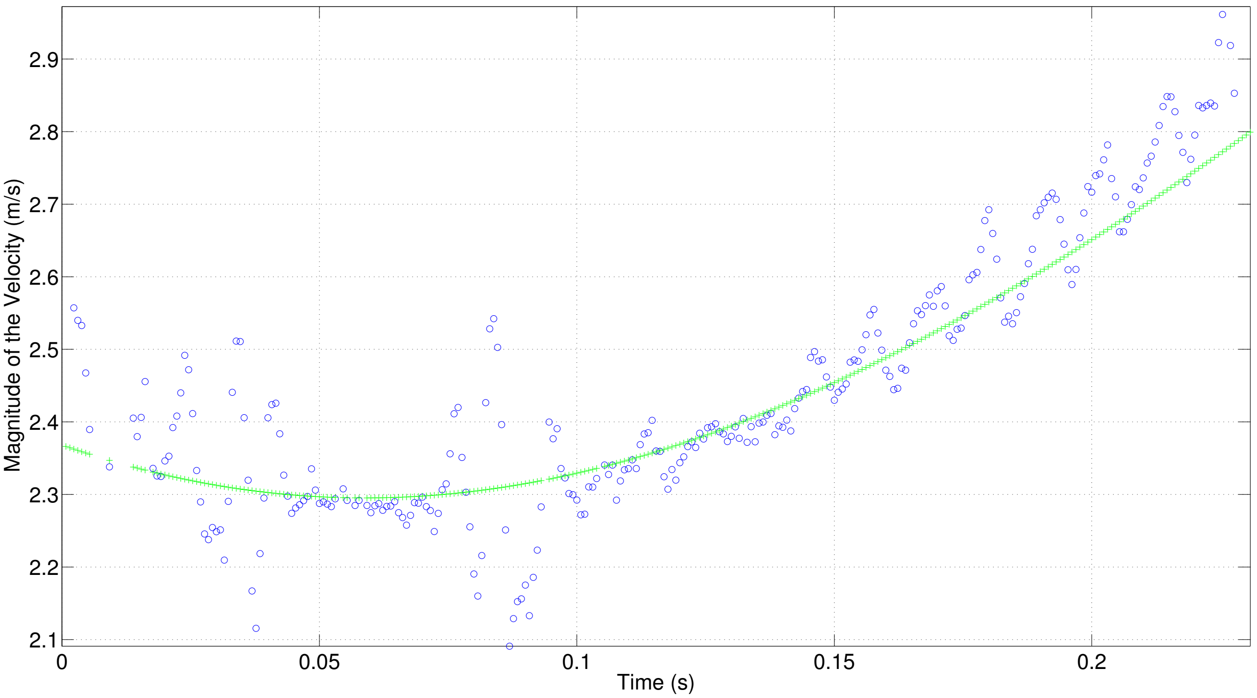

Figure 4.12: The blue data points are the speeds calculated at every time step of the DT reconstruction (using finite differences) and the green line is the speed calculated at every time step from the ODE-based trajectory. This is for one droplet in the second transfer blood experiment. The optimisation norm is 1.93 centimetres.

4.4 Validation of the Model by Comparing Speeds for Full Experiments

To ensure that the paths chosen in Section 4.3 were not remote instances of good speed validation, we plot a histogram of all the speeds calculated by the ODE model and all the speeds calculated using the finite difference method on the DT trajectories. Meaning, for each DT trajectory in an experiment (and its corresponding ODE-based trajectory), the speeds are calculated at each time step (using the appropriate method). All the speeds calculated using the finite difference method are put into one histogram and compared to another histogram with the speeds generated from the ODE model. We expect that these histograms should look similar.

Figure 4.13 shows the speeds calculated via finite differences (blue histogram) and the speeds calculated by the ODE model (red histogram) for a porcine blood experiment. We can see that these histograms follow the same shape and so we can conclude that the speed validations in Section 4.3 are not an isolated cases. The same conclusion can be drawn for Figure 4.14 which plots the histograms for speeds calculated for a transfer blood experiment.

As a result of these speed validations we conclude that the speeds being calculated by the ODE model at each time step are reasonable and correct. Since the Reynolds number and drag coefficient are dependent on this speed calculation, in the ODE model, we can confirm that our model has been validated by a method independent of the procedures outlined in our model.

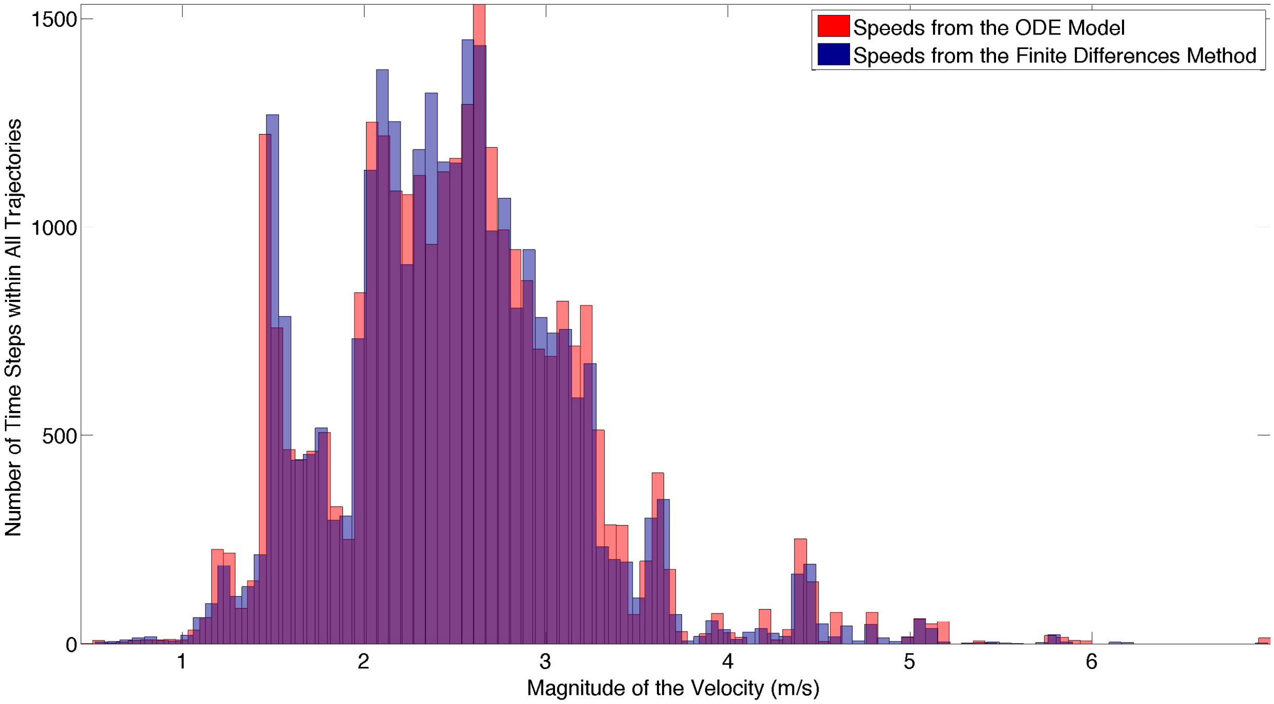

Figure 4.13: The red histogram shows the velocities calculated at each time step by the ODE model and the blue histogram shows all the velocities at each time step of the DT reconstructions (using finite differences). The histograms are generated from a porcine blood experiment. We are using transparency in the histogram colours to show the overlap.

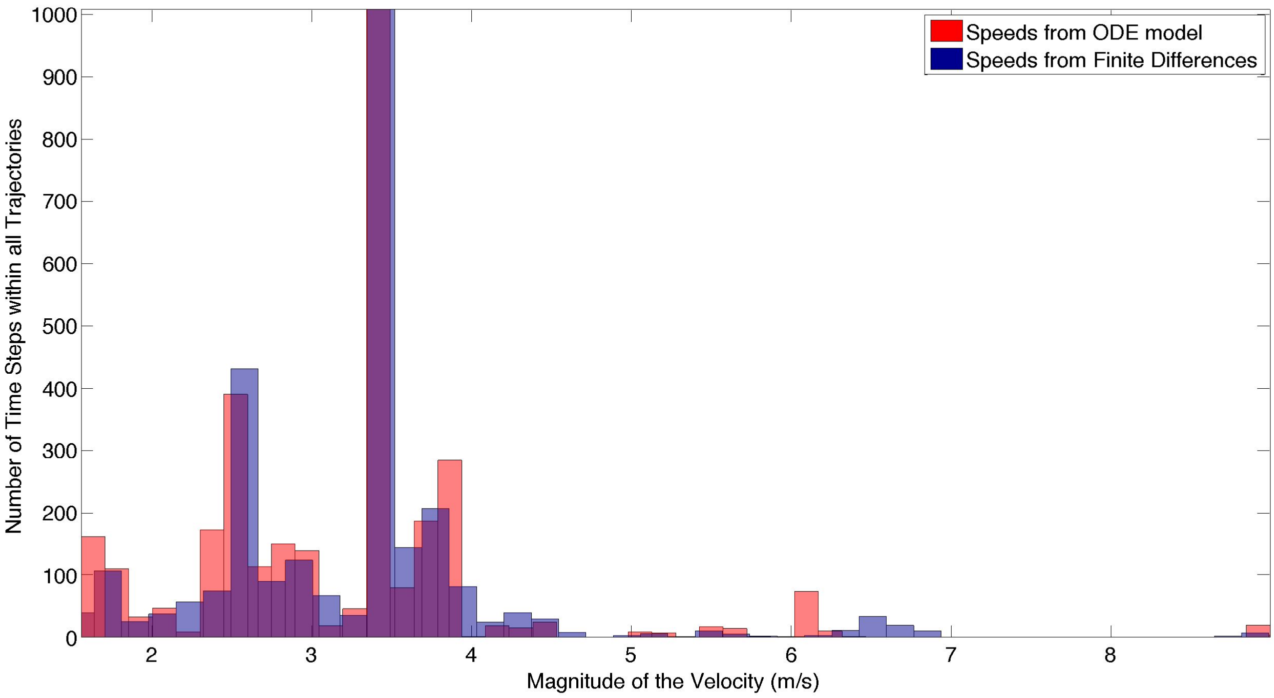

Figure 4.14: The red histogram shows all the velocities calculated by the ODE model and the blue histogram shows all the velocities at each time step of the DT reconstructions (using finite differences). The histograms are generated from a transfer blood experiment. We are using transparency in the histogram colours to show the overlap.

4.5 Analysing the Reynolds numbers and Resulting Drag Coefficients

The specific porcine blood experiment and transfer blood experiment shown in this section were selected because they had the most experimental path reconstructions that passed the criteria for rejection (see Section 3.3.5). The porcine blood experiment has 128 experimental path reconstructions fitted by the ODE model while the transfer blood experiment has 50.

A histogram of the Reynolds numbers calculated by our ODE model for the porcine blood experiment is shown in Figure 4.15. We can see that lower range of Reynolds numbers is approximately $\mathrm{Re} = 250$. This is much higher than what is considered a low Reynolds number, $\mathrm{Re} \ll 1$, which would invoke Stokes' law [3]. Figure 4.16 shows the corresponding drag coefficients calculated for the porcine blood experiment. Only 20% of the calculated drag coefficients are exactly 0.424, *i.e.*, the Reynolds number is greater than 1000. This indicates that the drag coefficient of a droplet cannot be fixed to 0.424 but must be calculated as discussed in Section 3.1.4.

The distribution of Reynolds numbers for a transfer blood experiment is shown in Figure 4.17. The majority of the Reynolds numbers calculated are centred around $\mathrm{Re} = 1000$. Figure 4.18 shows a histogram of the drag coefficients calculated in this transfer blood experiment. Only 60% of the drag coefficients calculated are exactly 0.424 corresponding to a Reynolds number greater than 1000. This is much higher than the porcine blood experiment shown earlier but this difference can be attributed to the amount of droplets tracked in the experiment.

A drag crisis is a phenomenon in fluid mechanics in which the drag coefficient of a body (typically a sphere or a cylinder) experiences a rapid drop as a function of the Reynolds number [29]. Typically, a drag crisis occurs when the Reynolds number characterising the flow is on the order of 10^5. Given that the Reynolds numbers empirically determined

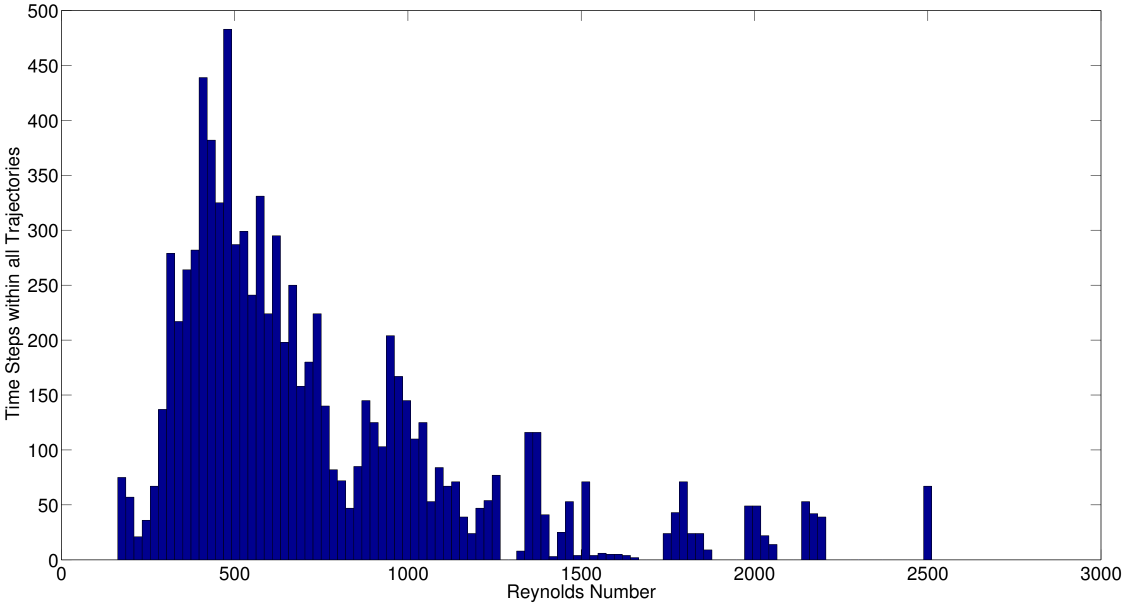

Figure 4.15: A histogram of the Reynolds numbers calculated for a porcine blood experiment.

from our experiments are well below 5000 on average (see Figures 4.15 and 4.17), we do not expect a drag crisis to occur.

Since we will not be observing the drag crisis for this range of Reynolds numbers, characterising the flow of air around the blood droplet, we can be sure that Equation 3.8 is a good approximation of the drag coefficient in the range Re $>$ 1000. Figure 4.19 shows the drag coefficient plotted for a range of Reynolds numbers and a black line corresponding to the drag coefficient for a rigid sphere, $\kappa = 0.424$. While the expression used for Reynolds numbers smaller than 1000 in Equation 3.8 does decrease below $\kappa = 0.424$ for larger Reynolds numbers, the approximation for Re $>$ 1000 is still appropriate as we are assuming the droplets are rigid spheres.

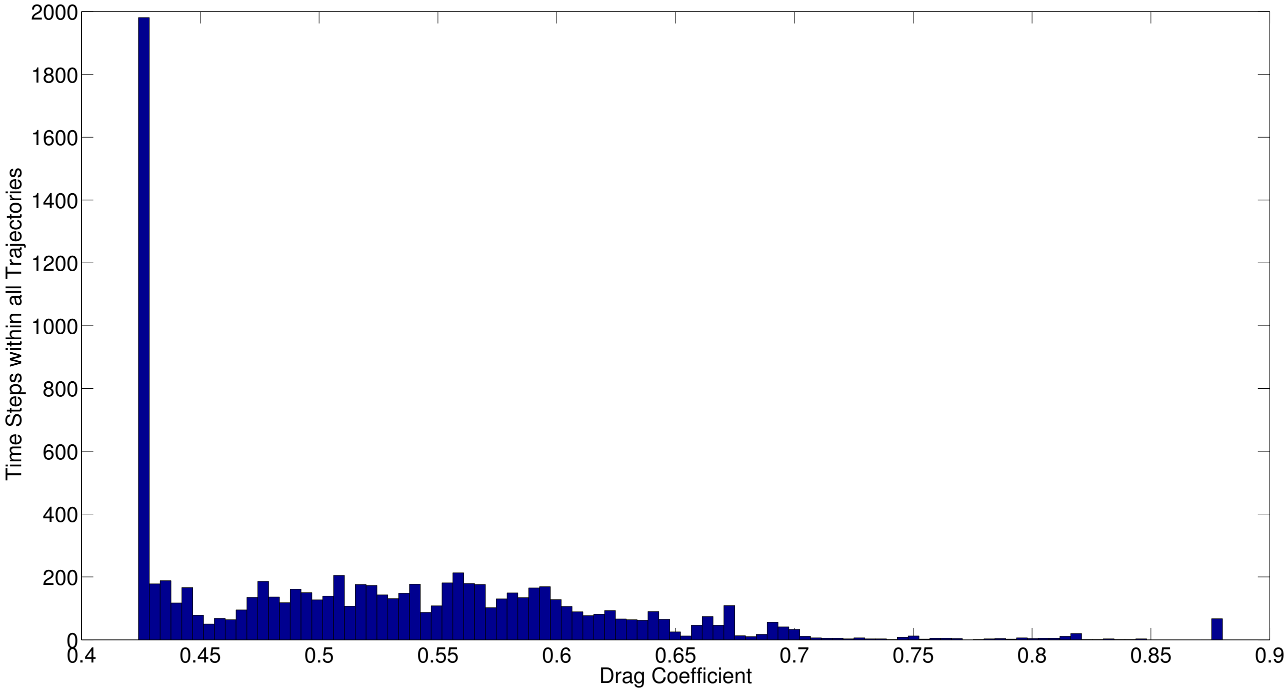

Figure 4.16: A histogram of the Drag Coefficients calculated for a porcine blood experiment.

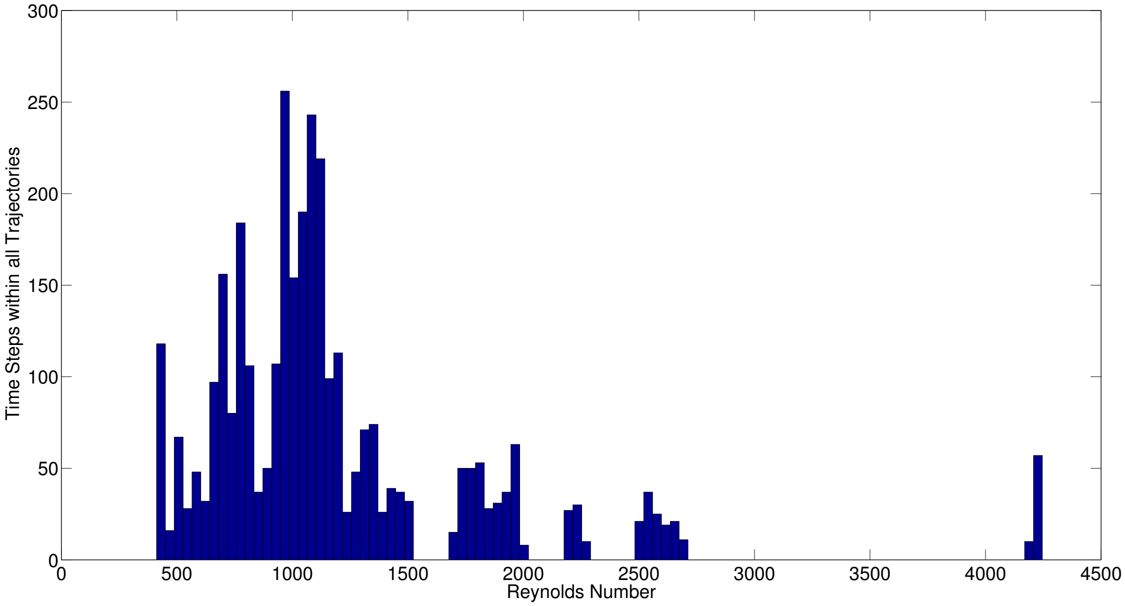

Figure 4.17: A histogram of the Reynolds numbers calculated for a transfer blood experiment.

4.6 Analysing the Optimisation Norms and Average Estimated Misfits

Figure 4.20 shows a histogram of the optimisation norms associated with the paths analysed in a porcine blood experiment. This histogram is heavily skewed left which reflects well on our model. Figure 4.21 shows the average estimated misfit associated with each path and this histogram is also skewed left which reflects well on the program DT [30] used to track the droplets. There are a few outliers toward an average estimated misfit of 0.02 centimetres but we do not expect any instances beyond 0.02 centimetres because the error criteria discards paths with an average estimated misfit over 0.02 centimetres (see Section 3.3.5). The same conclusions can be drawn concerning the histograms of the optimisation norm (Figure 4.22) and average estimated misfit (Figure 4.23) for a transfer blood experiment.

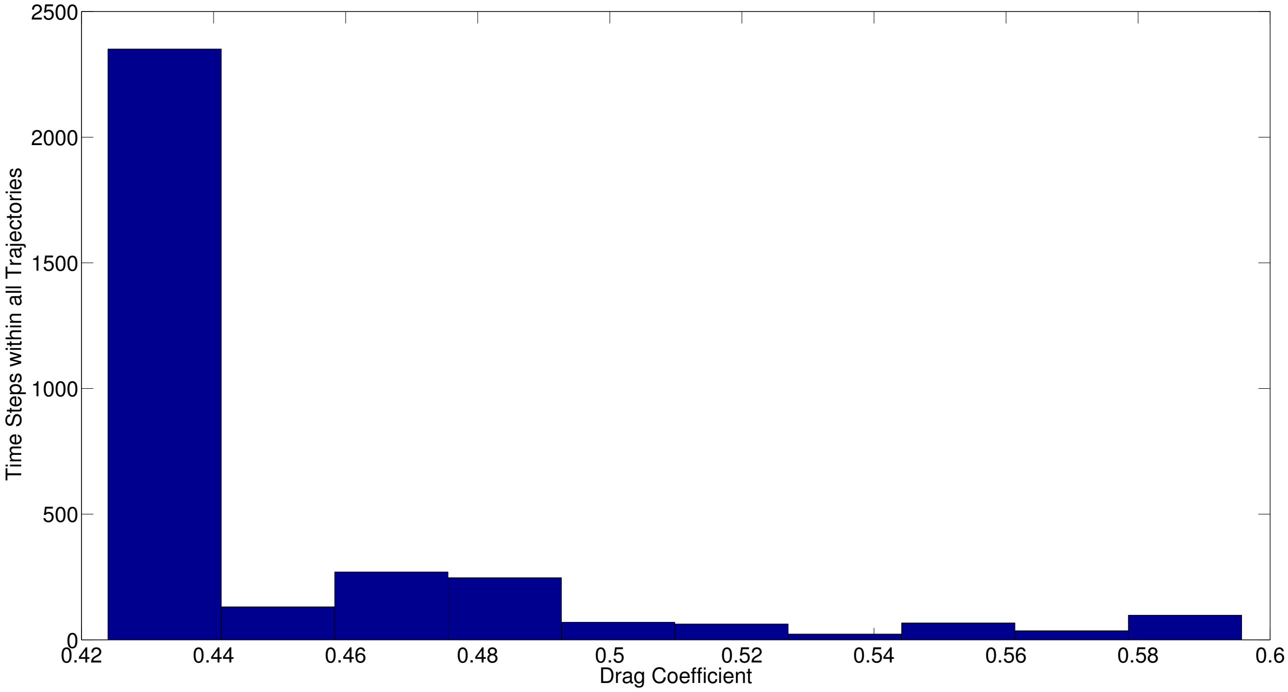

Figure 4.18: A histogram of the drag coefficients calculated for a transfer blood experiment.

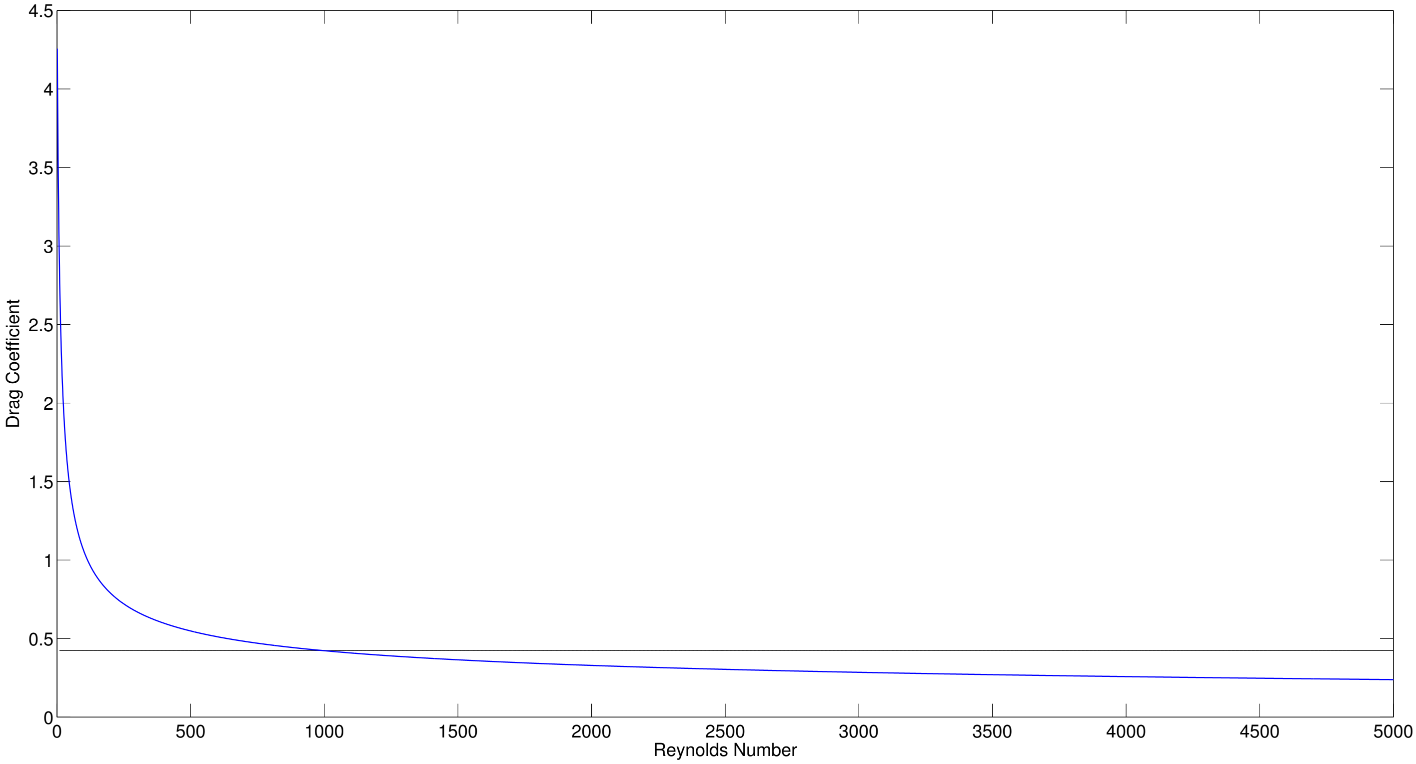

Figure 4.19: A plot of the calculation of the drag coefficient using a range of Reynolds numbers from $10 \leq \mathrm{Re} \leq 5000$ in Equation 3.8 (in blue) and a line plotted at $\kappa = 0.424$ (in black).

4.7 Discussion

From the results presented in this chapter, we can conclude that our ODE-based model successfully incorporates the forces of gravity and drag. Our model can also reliably retrieve parameters for unique reconstructed trajectories from a bloodletting event. These parameters are the initial speed, azimuthal angle, altitude angle, radius, Reynolds number and finally the drag coefficient for any given droplet tracked by DT. Further, we see that the optimisation solver did not choose one specific value for the drag coefficient and thus we can conclude that the drag coefficient cannot be fixed to a specific value but must be calculated as a function of the droplet's radius and velocity.

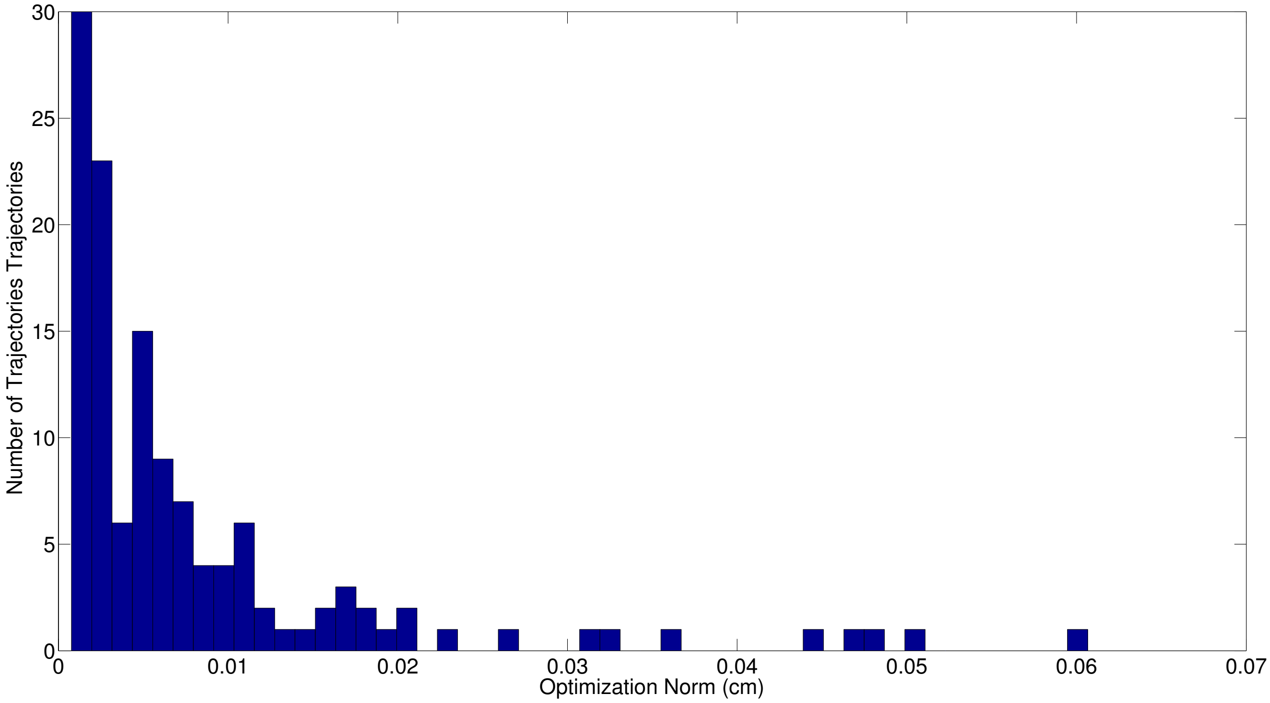

Figure 4.20: The optimisation norms for each trajectory analysed by the model in a porcine blood experiment.

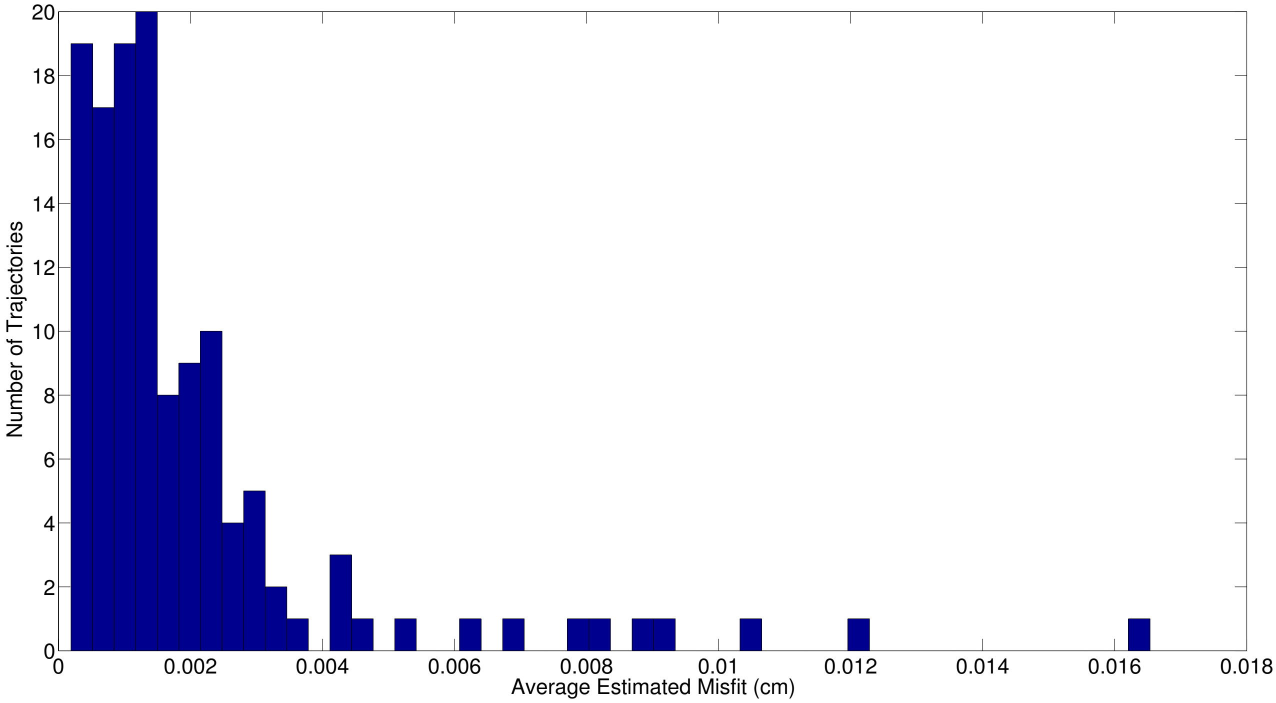

Figure 4.21: The average estimated misfit (from DT) for each trajectory analysed by the model in a porcine blood experiment.

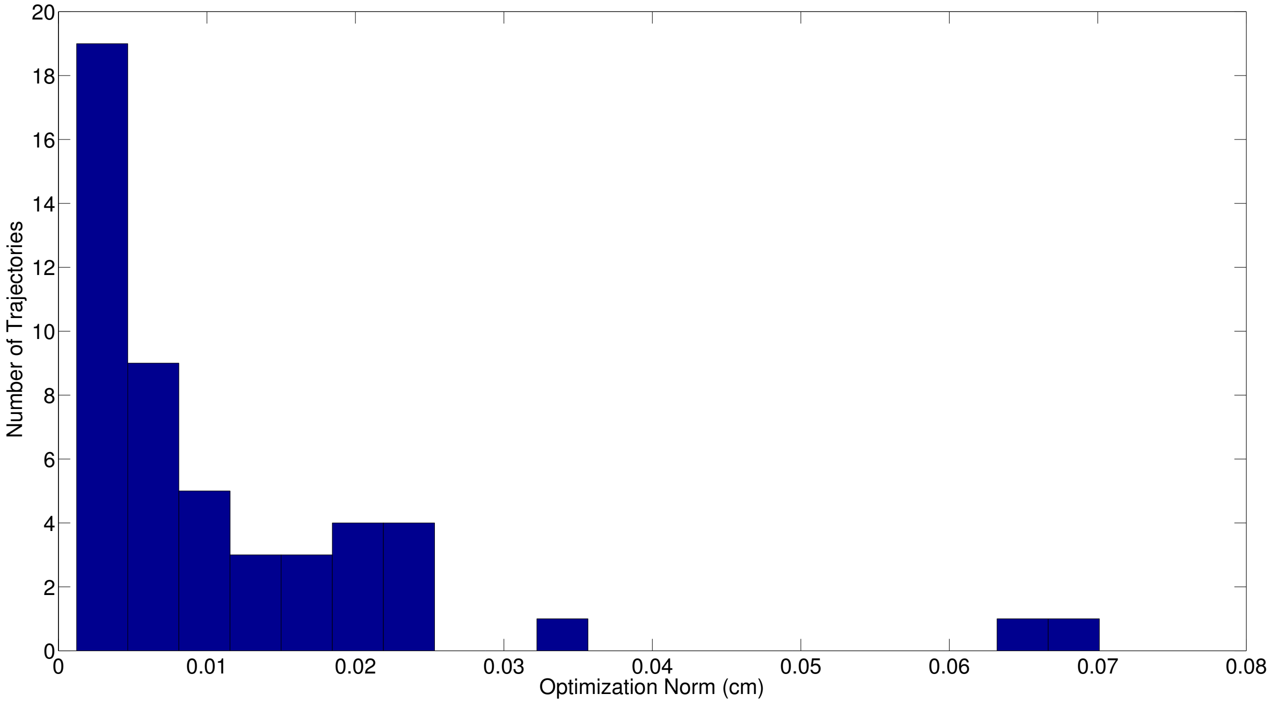

Figure 4.22: The optimisation norms for each trajectory analysed by the model in a transfer blood experiment.

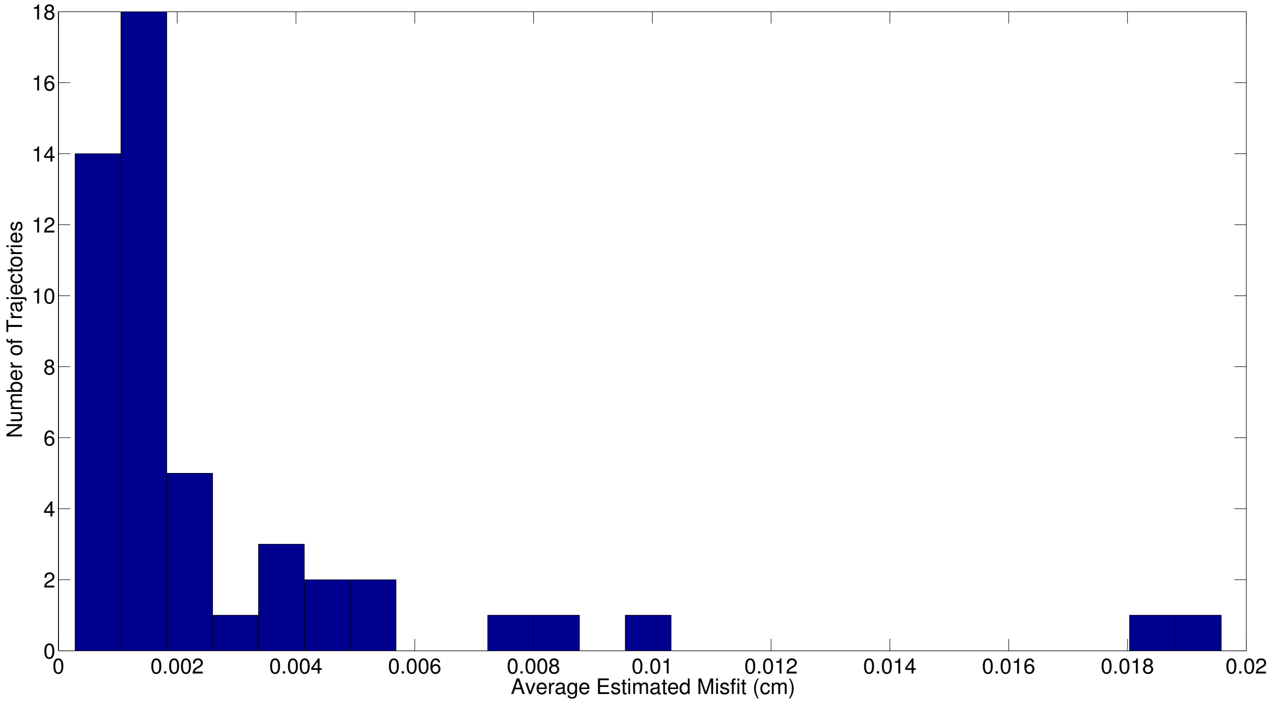

Figure 4.23: The average estimated misfit (from DT) for each trajectory analysed by the model in a transfer blood experiment.

We can also confirm that the force of drag (see Equation 3.11) used for the droplets is appropriate because the Reynolds number is high enough to dismiss using Stoke's drag. We also confirm that the drag crisis is unlikely to occur in the range of Reynolds numbers observed. The speeds used to calculate the drag coefficient and Reynolds number of a droplet has been validated by an independent calculation of the speeds from the experimental path reconstruction (see Sections 4.3 and 4.4). Since this model includes the forces of gravity and drag in three-dimensions it can be used to create paths based on the Equation 3.17. The outline of using this ODE model backwards in time as a BPA tool is outlined in Chapter 5.

Chapter 5

Conclusions and Future Research

5.1 Conclusions

We show that a three-dimensional, physics based, ODE model can successfully fit experimental path reconstructions from a bloodletting event. An advantage to our model is the incorporation of the forces of gravity and drag acting upon the droplet. This results in our model not being restricted by straight line geometric reconstructions. From our laboratory experiments, outlined in Chapter 2, we collect stereo video data of simulated bloodletting events. The blood droplets emerging from the ballistics gel are tracked using software from [30] and the trajectories of the blood droplets are reconstructed. The Euclidean distance between the experimental path reconstructions and the ODE-based trajectories is minimised. These ODE-based trajectories match the path reconstructions reasonably well as seen in Sections 4.1 and 4.2. The optimisation norm of this problem is low, along with the average estimated misfit from tracking the droplets (see Section 4.6). Our model is based on the integration of Equation 3.17 and thus can be integrated backward in time to be used as a tool in Bloodstain Pattern Analysis.

5.2 Future Research

The Bloodstain Pattern Analysis (BPA) problem is at the very heart an inverse problem. A bloodletting event produces a bloodstain and in BPA, an investigator is presented with the bloodstain, the solution to the problem. The investigator's task is to reconstruct the bloodletting event which is solving the inverse problem. From a given bloodstain pattern, ballistic properties like a blood droplet's angle of impact and the droplet's impact velocity can be inferred and used to find the location of the bloodletting event. These become the initial conditions and the model must move backwards in time, using physical principles, to arrive at the initial velocity of the blood droplets and their starting position. The model presented in this thesis could, in theory, be used as a forward model in an inverse problem to find the source of bloodstains. Since the ODE-based trajectories are based on the integration of a model, we can integrate the same ODE backwards using different initial conditions. The inputs to the inverse model would include the radius of the droplet, the impact velocity of the droplet, the impact angles and the drag coefficient.

An immediate advantage of this inverse model is the accommodation of droplets that hit the surface moving in the downward direction or droplets far from the bloodletting source. This inverse model would still not account for oscillations of the droplet during its flight but it would account for the forces of gravity and drag. The inverse problem is expected to be ill-posed in the sense that the problem will be underdetermined. Further, errors in extracting information about the radius and impact angles from the bloodstain will be amplified when the inverse model attempts to find the origin of the blood droplet.

5.2.1 Initial Conditions of the Inverse Problem

A few properties can be found from the stain of a single droplet. The conventional and simplest properties to measure from the single stain are the width (minor axis, w) and length (major axis, l). Consider Figure 5.1, a simple image of a bloodstain pattern created by Maloney [18].

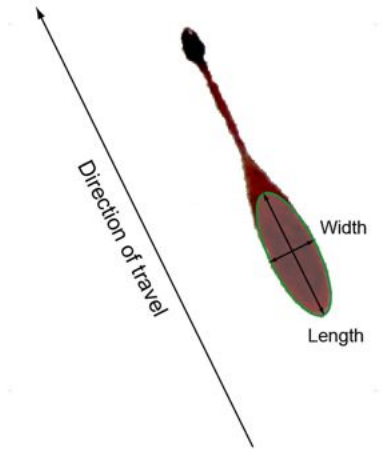

Figure 5.1: Classical measuring of bloodstain patterns where the direction of travel is characterised by following the tail of the blood droplet once it has impacted a surface. See [16].

The width and the length of the bloodstain are relevant because we can find the angle of impact with the surface with a simple trigonometric formula,

$$\sin\alpha = \frac{w}{l}, \tag{5.1}$$

which is also known as the Balthazard formula [4]. With this simple calculation and by measuring the glancing angle, γ we can find what is called the string angle using

$$\tan\beta = \frac{\tan\alpha}{\sin\gamma}. \tag{5.2}$$

All these angles are depicted in Figure 5.2.

There is still a vital piece of information missing here which can not be solved for using simple trigonometric formulae and that is the impact speed of the droplet u_0. All the angles of impact can be extracted but none of the velocity components (as shown in Figure 5.2) can be determined using just these measurements. Fortunately, there have been studies done on circular bloodstains and a formula has been derived to find the

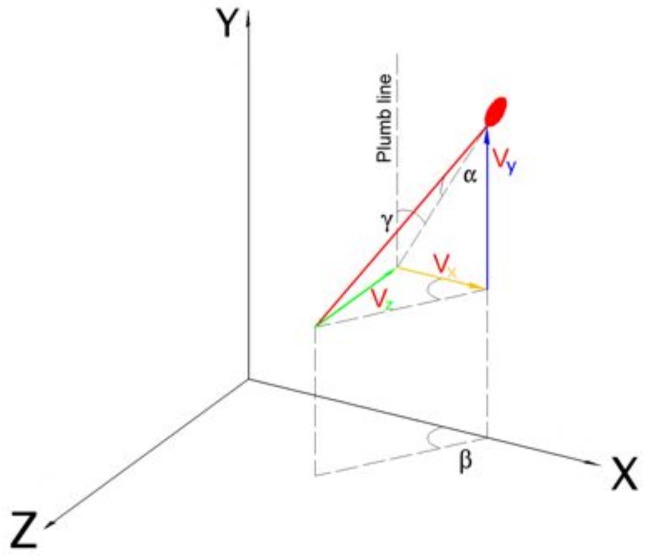

Figure 5.2: The impact angle, stringing angle and glancing angle with respect to a blood droplet which is landing on the xy-plane. The components of velocity are also shown and this figure was edited to match the coordinate system used in our model. See [16].

impact speed using the spines of the circular droplet [10] and on angled stains [14]. If the speed cannot be measured from the stain, then a reasonable range of speed could be used in the inverse problem which would produce a selection of paths from one stain. In the context of a small number of individual elliptical bloodstains patterns, a region of intersection can be found. Further, the validity of Equation 5.1 depends on assumptions about the droplet and its flight. Rowe [27] states these assumptions:

> The drop of blood is spherical at the time of impact and has travelled in a straight line to the point of impact.

When measuring the width and length of a bloodstain, there will be uncertainties which carry over into the calculation of the impact angle, α. These uncertainties are explored in [27] and need to be considered when using our model in the inverse problem. There has also been work done in solving the inverse problem using probabilistic methods [7].

This method includes the forces of gravity and drag in the model; however, the estimate for the drag coefficient is Stokes' drag (instead of a correction to Stokes' drag, as used in our model). Further, the method has only been tested on planar data and more tests are needed to validate the entire algorithm.

5.2.2 Surfaces

Within the field of bloodstain pattern analysis, there is a large area of research dedicated to blood droplet impacts on different surfaces. As mentioned in Chapter 2, we attempted a few experiments using surfaces other than white laminated plywood walls. The experiments using carpets were discarded because the bloodstain had seeped into the carpet before the photographs could be taken. However, from our experiments using cardboard surfaces (see Figure 5.3), we discover that blood droplets (both porcine and transfer blood) adhere better to cardboard than to laminated plywood.

The digital photographs captured in our experiments can be used to validate computed solutions of the inverse problem. Other research directions include the development of methods for extraction of bloodstains from photographs and automating the collection of individual features from bloodstains (e.g., lengths, widths, and glancing angles of bloodstains caused by individual droplets). Shen *et. al.*, in [28], has proposed an image analysis technique that can automate the gathering and analysis of bloodstain pattern data. However, the experimental validation of that specific algorithm used paint rather than blood thus further trials could be necessary. Carter [6], has also proposed an automated method for calculating the glancing angle using the digital photographs of a bloodstain.

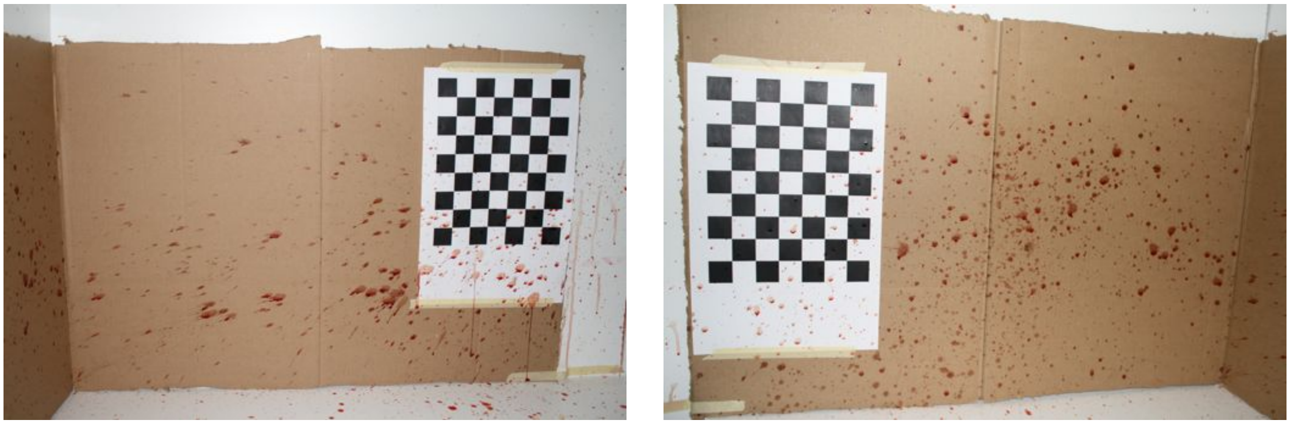

(a) Porcine bloodstain pattern photograph taken in a position in front of Camera A.

(b) Porcine bloodstain pattern photograph taken in a position in front of Camera B.

Figure 5.3: A digital photograph of the resulting bloodstain pattern formed on a cardboard surface from the porcine blood experiment.

5.2.3 Collisions

The initial velocity of blood droplets are dictated by the initial impact on the ballistics gel. There is relationship between the impact velocity of the riot ball on the gel, to the droplet's initial velocity. The backbone of this problem is in the equations for an inelastic collision in physics where

$$m_b\mathbf{v}_b = m_b^{'}\mathbf{v}_b^{'} + \sum_i^N m_i\mathbf{v}_i. \tag{5.3}$$

In Equation 5.3, m_b and $\mathbf{v}_b$ are, respectively, the mass and the velocity of the bullet prior to the impact. Immediately after the impact, the mass and velocity of the bullet are m_b' and $\mathbf{v}_b'$ respectively. The term $m_i\mathbf{v}_i$ within the sum in Equation 5.3 constitute the momentum transferred to the ith droplet (assuming the target breaks into N individual droplets). This would be useful to investigate for the purpose of studying how droplets break up or how many droplets to expect at a crime scene given a certain impact or associating the impact velocity of the droplets on the surface to the impact velocity from the weapon. The above is a very simplistic approach to investigating the initial velocities of droplets but could be worth looking into.

5.2.4 Models of Oscillations in Moving Droplet Shape

As mentioned in Section 1.1, the droplet undergoes radial distortions because, realistically, the droplet is not a rigid sphere; rather, it is a fluid. Raymond explains these oscillations clearly [25]:

> The forces that damp droplet oscillations are due to viscosity acting on the internal flow in the droplet while the forces that 'drive' the oscillations, once a droplet has been distorted, are due to surface tension. The surface tension tries to minimise the surface area of the droplet.

According to Liu *et al.* in [15] "the drag coefficient of a distorting drop should lie between the lower limit of a rigid sphere and the upper limit of a disk". From this we can understand that the droplet's maximum radial deviation will resemble a disk shape. In [15], Liu *et. al.* present a second-order ODE model for the oscillation of the surface of a droplet in flight, namely,

$$\ddot{y} = \frac{C_F \rho_{\mathrm{air}} W^2}{C_b \rho_{\mathrm{d}} a^2} - \frac{C_k \sigma_{\mathrm{d}}}{\rho_{\mathrm{d}} a^3} y - \frac{C_d \mu_{\mathrm{d}}}{\rho_{\mathrm{d}} a^2} \dot{y}, \tag{5.4}$$

In Equation 5.4, the independent variable y is the radial distortion, σ_d is the surface tension of the droplet, a is a characteristic radius, W is the relative velocity, and C_b, C_F, C_d, and C_k are constants obtained in [20]. Liu [15] proposed that solving Equation 5.4 for the radial distortion, y, could be used in the linear variation of the drag coefficient,

$$\kappa = \kappa_{sphere} \left(1 + 2.632y\right), \tag{5.5}$$

where κ would be the drag coefficient at each time step. Equation 5.5 still needs to be validated by experiment which could be done by having droplets of known volume dropped into an air stream and the motion of the droplet in the air stream should be recorded by high-speed cameras with high enough resolution to observe the radial distortions of the droplet.

Bibliography

[1] D. J. Acheson. *Elementary Fluid Dynamics.* Oxford Applied Mathematics and Computing Science Series. Oxford University Press, New York, 1990.

[2] S. K. Aggarwal and F. Peng. A review of droplet dynamics and vaporization modeling for engineering calculations. *Journal of Engineering for Gas Turbines and Power*, 117:1384–1394, 1995.

[3] G. K. Batchelor. *An Introduction to Fluid Dynamics.* Cambridge University Press, 2000.

[4] T. Bevel and R. M. Gardner. *Bloodstain Pattern Analysis: With an Introduction to Crime Scene Reconstruction.* CRC Press, New York, second edition, 2001.

[5] U. Buck, B. Kneubuehl, S. Näther, N. Albertini, L. Schmidt, and M. Thali. 3D bloodstain pattern analysis: Ballistic reconstruction of the trajectories of blood drops and determination of the centres of origin of the bloodstains. *Forensic Science International*, 206:22–28, 2010.

[6] A. L. Carter. The Directional Analysis of bloodstain patterns: Theory and experimental validation. *Canadian Society of Forensic Science*, 34(4):173–189, 2001.

[7] B. Cecchetto and W. Heidrich. Probabilistic inverse dynamics for blood pattern reconstruction. *Vision, Modeling, and Visualization*, 2011.

[8] K. G. de Bruin, R. D. Stoel, and J. C. M. Limborgh. Improving the point of origin determination in bloodstain pattern analysis. *Journal of Forensic Science*, 56(6):1476–1482, November 2011.

[9] L. Hulse-Smith and M. Illes. A blind trial evaluation of a crime scene methodology for deducing impact velocity and droplet size from circular bloodstains. *Journal of Forensic Sciences*, 52(1):65–69, 2007.

[10] L. Hulse-Smith, N. Z. Mehdizadeh, and S. Chandra. Deducing drop size and impact velocity from circular bloodstains. *Journal of Forensic Science*, 50:1, 2005.

[11] M. B. Illes, A. L. Carter, P. L. Laturnus, and A. B. Yamashita. Use of the BACKTRACK computer program for bloodstain pattern analysis of stains from downward-moving drops. *Canadian Society of Forensic Science*, 38(4):213–218, 2005.

[12] M. H. Wright J. C. Lagarias, J. A. Reeds and P. E. Wright. Convergence properties of the Nelder-Mead simplex method in low dimensions. *SIAM Journal of Numerical Analysis*, 9(1):112–147, 1998.

[13] S. H. James and J. J. Nordby. *Forensic Science: An Introduction to Scientific and Investigative Techniques.* Taylor & Francis Group, 2005.

[14] C. Knock and M. Davison. Predicting the position of the source of bloodstains for angled impacts. *Journal of Forensic Science*, 52(5):1044–1049, 2007.

[15] A. B. Liu, D. Mather, and R. D. Reitz. Modeling the effects of drop drag and breakup on fuel sprays. SAE Technical Paper Series, University of Wisconsin, Masidon Engine Research Center, 1993.

[16] A. Maloney and K. Maloney. Hemospat bloodstain pattern analysis software, 2009.

[17] A. Maloney, C. Nicloux, K. Maloney, and F. Heron. One-sided impact spatter and area-of-origin calculations. *Journal of Forensic Identification*, 61(2):123–135, 2011.

[18] K. Maloney, J. Killeen, and A. Maloney. The use of HemoSpat to include bloodstains located on nonorthogonal surfaces in area-of-origin calculations. *Journal of Forensic Identification*, 59(5):513–524, 2009.

[19] Mega Speed. *High-Speed B/W & Color CMOS Camera Model MS50K & MS55K*, 2.9 edition, 2010. Instruction Manual.

[20] P. J. O'Rourke and A. A. Amsden. The tab method for numerical calculation of spray droplet breakup. SAE Technical Paper Series, 1987.

[21] F. Peng and S. K. Aggarwal. Droplet motion under the influence of flow, nonuniformity and relative acceleration. 1993. Presented at the 206th ACS National Meeting.

[22] P. A. Pizzola, S. Roth, and P. R. De Forest. Blood droplet dynamics – I. *Journal of Forensic Sciences*, 31:36–49, 1986.

[23] P. A. Pizzola, S. Roth, and P. R. De Forest. Blood droplet dynamics – II. *Journal of Forensic Sciences*, 31:50–64, 1986.

[24] A. Putnam. Integrable form of droplet drag coefficient. *American Rocket Society Journal*, 31:1467–68, 1961.

[25] M. A. Raymond, E. R. Smith, and J. Liesegang. Oscillating blood droplets—implications for crime scene reconstruction. *Science & Justice*, 36:161–171, 1996.

[26] M. A. Raymond, E. R Smith, and J. Liesegang. The physical properties of blood—forensic considerations. *Science & Justice*, 36:153–160, 1996.

[27] W. F. Rowe. Errors in the determination of the point of origin of bloodstains. *Forensic Science International*, 161:47–51, 2006.

[28] A. R. Shen, G. J. Brostow, and R. Cipolla. Toward automatic blood spatter analysis in crime scenes. In *The Institution of Engineering and Technology Conference*

on Crime and Security, pages 378–383. University of Cambridge, Department of Engineering, 2006.

[29] S. P. Singh and S. Mittal. Flow past a cylinder: Shear layer instability and drag crisis. *International Journal for Numerical Methods in Fluids*, 47:75–98, 2005.

[30] L. Zarrabeitia, D. A. Aruliah, and F. Z. Qureshi. Extraction of blood droplet flight trajectories from videos for forensic analysis. Algarve, Portugal., 2012. International Conference on Pattern Recognition Applications and Methods.